The excitonic fine structure of colloidal nanocrystals

Submitted by

Thi Hanh Bui

Dissertation
with the aim of achieving a doctoral degree
at the Faculty of Mathematics, Informatics and Natural Sciences
Department of Chemistry
University of Hamburg

February, 2020

Supervisor: Prof. Dr. Gabriel Bester
Co-supervisor: Prof. Dr. Alf Mews
Disputation date: 25/09/2020

Contents

List of publications v

List of Figures vii

List of Tables xi

Acronyms xiii

Zusammenfassung xvii

Abstract xx

Introduction 1

1 Basics of Ab-initio electronic structure calculations **3**

1.1 Many-body problem and Born-Oppenheimer approximation 3

1.2 Exchange and correlation 5

1.3 Density functional theory 5

1.3.1 Hohenberg-Kohn theorems 5

1.3.2 Kohn-Sham equations 7

1.3.3 Local density approximation 8

1.4 Periodic supercells and plane-wave pseudopotential method 10

2 Atomic effective pseudopotential for semiconductors **15**

2.1 Atomic effective pseudopotential for periodic systems 16

2.1.1 Analytic connection between AEPs and effective Kohn-Sham potentials for bulk systems 16

2.1.2 AEPs construction 18

2.2 Atomic effective pseudopotential for nanocrystals 21

- 2.2.1 Analytic connection between AEPs and effective Kohn-Sham potentials for passivant. 21
- 2.2.2 AEPs for InP and CdSe passivants 24
- 2.2.3 Assessment of the quality of the AEP for different surfaces . . . 26
- 2.2.4 Results for Si, InP and CdSe nanowires 27
- 2.2.5 Results for InP and CdSe QDs 30
- 2.3 Generation of artificially relaxed QDs 31

3 Empirical correction 37
- 3.1 The functional form of the correction 37
- 3.2 Result for InP 38
- 3.3 Result for CdSe 40
- 3.4 Result for HgTe 42

4 Configuration interaction method 47
- 4.1 N-particle wave-function 47
- 4.2 CI calculation procedure 49

5 Excitonic fine structure of colloidal nanocrystals 55
- 5.1 Excitonic fine structure of CdSe nanocrystals 56
  - 5.1.1 Comparison to Experiment and to EMA results 57
  - 5.1.2 Comparison between the FS of WZ and ZB NCs. 61
  - 5.1.3 Exciton lifetime of CdSe NCs 68
    - 5.1.3.1 Experiment measurement 68
    - 5.1.3.2 Theoretical calculation 71
    - 5.1.3.3 Results 71
  - 5.1.4 Conclusion 73
- 5.2 Excitonic fine structure of InP nanocrystals 74
  - 5.2.1 CI convergence 74
  - 5.2.2 Excitonic fine structure of spherical InP NCs 75
  - 5.2.3 Conclusion 77
- 5.3 Excitonic fine structure of HgTe nanocrystals 77
  - 5.3.1 Electronic properties of HgTe nanocrystals 77
  - 5.3.2 Optical properties of HgTe nanocrystals 79
  - 5.3.3 Conclusion 85

Summary and Outlook **87**

Bibliography **89**

Acknowledgements **101**

Declaration **103**

List of publications

1. A. Karpulevich, H. Bui, D. Antonov, P. Han, and G. Bester, "Nonspherical atomic effective pseudopotentials for surface passivation," Phys. Rev. B 94, 205417 (2016).

2. A. Karpulevich, H. Bui, Z.Wang, S. Hapke, C. P. Ramírez, H. Weller, and G. Bester, "Dielectric response function for colloidal semiconductor quantum dots," J. Chem. Phys. 151, 224103 (2019).

3. H. Bui, A. Karpulevi, and G. Bester, "Excitonic fine structure of zincblende and wurtzite colloidal CdSe nanocrystals and comparison to effective mass results", Phys. Rev. B 101, 115414 (2020).

List of Figures

1.1 Supercell geometry for a point-defect (vacancy) in a bulk solid (a) and for a quantum dot (b). 12

2.1 Band structure of Zinc-blende InP bulk and Wurtzite CdSe bulk 20
2.2 Real and pseudo hydrogen passivants of (a) Si, (b) CdSe, and (c) InP . 23
2.3 Slab A (a) and slab B (b) used to construct the AEPs for passivant H_1 and H_2 23
2.4 Hydrogen AEP in real and reciprocal space 24
2.5 AEPs for InP passivants as functions of $|G|$ 25
2.6 AEPs for CdSe passivants as functions of $|G|$ 26
2.7 Comparison between AEPs and DFT results for (111), (110), and (100) surfaces. 27
2.8 The geometry of the InP nanowire with a diameter of 1.6 nm and the corresponding local potential 28
2.9 Eigenvalues of the $D = 1.6$ nm InP quantum wire (QW) with and without weight 29
2.10 Eigenvalues of Si, InP, and CdSe nanowires in the proximity of the band gap 30
2.11 DFT and AEP results for 2.4 nm diameter InP QD 31
2.12 Flow diagram of nanocrystals (NCs) generation procedure 32
2.13 Forces acting on the atoms of 1.6 diameter InP QD and 2.4 diameter InP QD 32
2.14 QD before and after refinement by replacing clusters of passivants of In atoms by P atoms 33
2.15 Comparison between the relaxed and non-relaxed 1.6 nm diameter InP QD 34

3.1 Contour plot the differences between calculated values and the experimental values of band-gap and the effective mass of electron 38
3.2 Band structure of InP before and after corrections. 39
3.3 Pseudopotential of In and P before and after correction. 40
3.4 Band structure of ZB CdSe before and after corrections 41
3.5 Band structure of WZ CdSe before and after corrections 42
3.6 Pseudopotential of Cd and Se before and after correction. 43
3.7 Band structure of HgTe before and after corrections 43
3.8 Pseudopotential of Hg and Te before and after correction. 44

4.1 Size-dependence of $\epsilon_{\infty}^{\text{bulk}}(R)$ and $\epsilon_{0}^{\text{bulk}}(R)$ of InP quantum dots 51
4.2 Size-dependence of $\epsilon_{\infty}^{\text{bulk}}(R)$ and $\epsilon_{0}^{\text{bulk}}(R)$ of CdSe quantum dots 52
4.3 Size-dependence of $\epsilon_{\infty}^{\text{bulk}}(R)$ and $\epsilon_{0}^{\text{bulk}}(R)$ of HgTe quantum dots 52
4.4 Diagram summarises the input and output of the calculation procedure 53

5.1 Schematic representation of the FS of “spherical” WZ and ZB NCs . . . 56
5.2 Dark-bright splittings of “spherical” ZB and WZ CdSe NCs in comparison with SEPM and experiments 57
5.3 Exciton FS versus radius of “spherical” WZ NCs. Comparison between atomistic results and EMA, experiments 58
5.4 Oscillator strength of spherical WZ CdSe NCs and slightly elongated WZ CdSe NCs 60
5.5 Oscillator strength calculated for spherical and slightly prolate WZ CdSe NCs in comparison with experimental measurement 60
5.6 Schematic representation of the FS in “spherical” and oblate ZB NCs . 61
5.7 Oblate NC with an aspect ratio of 0.5 and prolate NC with an aspect ratio of 1.5 62
5.8 Projection of the h_0 state onto the bulk wave functions 63
5.9 The single-particle energy of the h_0 and h_1 states (both are aligned at the h_0 energy) for two WZ NCs 64
5.10 FS of ellipsoidal ZB and WZ CdSe NCs with the same horizontal diameter $\mathrm{D_h}$ of 2.8 nm but different vertical lengths 64
5.11 FS of ellipsoidal ZB and WZ CdSe NCs with the same horizontal diameter $\mathrm{D_h}$ of 3.6 nm but different vertical lengths 65

5.12 Figure corresponding to Fig. 5.10 and Fig. 5.11 but calculated using EMA for a horizontal diameter Dh of 2.8 nm. 66
5.13 Oscillator strength of ellipsoidal ZB and WZ CdSe NCs with the same horizontal diameter of 2.8 nm but different vertical lengths 67
5.14 Oscillator strength of ellipsoidal ZB and WZ CdSe NCs with the same horizontal diameter of 3.6 nm but different vertical lengths 68
5.15 Three-level system used to interpret the data 69
5.16 Time-integrated PL spectrum of InP/ZnS nano particle, with 2.9 nm core and 2-nm thick shell 69
5.17 The radiative lifetime of the bright exciton of the WZ CdSe QDs in comparison with experimental results 72
5.18 The convergence of the DB splitting and the first bright exciton energy with the single-particle basis set 75
5.19 The diagonal Coulomb integral and the DB splitting of InP quantum dots. 76
5.20 The first bright exciton energy of spherical InP quantum dots, experiment values are taken from refs. [11, 79, 80], respectively. 76
5.21 A spherical HgTe NC with a diameter of 3.8 nm and eigenvalues of this quantum dot 78
5.22 Projection of HOMO and LUMO wavefunctions of HgTe NCs onto the wavefunctions of the bulk system 79
5.23 Molecular orbital diagram of HgTe 79
5.24 Energy levels of HgTe and CdSe NCs with different sizes. 80
5.25 The convergence of the DB splitting and the first bright exciton energy with the single-particle basis set 80
5.26 The diagonal Coulomb integral and the DB splitting of HgTe NCs. . . . 81
5.27 The single particle (SP) and the optical (CI) gap of HgTe NCs for various sizes. 81
5.28 Exciton energy measured by various groups in comparison with our calculations 82
5.29 Comparison between our model and TB 83
5.30 Absorption spectra of (a) HgTe and (b) CdSe NCs with different diameters. 83
5.31 Dependence of the absorption spectra of the $D = 5.8$ nm HgTe NCs on the basis set. 84

5.32 Analyzing the origin of 5 resolved peaks in the absorption spectra of the $D = 5.8$ HgTe NCs. 84
5.33 Band-edge exciton and trion (-) peaks of (a) HgTe and (b) CdSe NCs at different diameters. 85
5.34 The difference in energy between the band-edge exciton and trion (-) peaks of HgTe and CdSe 85

List of Tables

2.1 Structural parameters and band gaps of different nanowires 28
2.2 Structural parameters and band gaps of different InP and CdSe QDs. . 30
2.3 Comparison between non-relaxed and relaxed InP QDs 33

3.1 m_e^*, band-gap, ΓL and ΓX gaps of InP bulk in experiment and theory with and without β corrections 39
3.2 m_e^*, band-gap, ΓL and ΓX gaps of CdSe bulk in experiment and theory with and without β corrections 40
3.3 Effective masses, band-gap, crystal field (CF) splitting Δ_CF and spin-orbit splitting Δ_SO of WZ CdSe bulk in experiment and theory with and without β corrections. 42
3.4 Effective masses, band-gap and spin-orbit splitting Δ_SO of HgTe bulk in experiment and theory with and without β corrections. 44

4.1 Parameters in the Thomas-Fermi and Haken models of InP, CdSe, and HgTe 51

Acronyms

AEP atomic effective pseudopotential.

CF crystal field.

CI configuration interaction.

DFT density-functional theory.

EMA effective mass approximation.

EPM empirical pseudopotential method.

FS fine structure.

HOMO highest occupied molecular orbital.

LDA local density approximation.

LSDA local spin density approximation.

LUMO lowest unoccupied molecular orbital.

NCs nanocrystals.

QD quantum dot.

QDs quantum dots.

QW quantum wire.

SEP semi-empirical pseudopotential.

SEPM semi-empirical pseudopotential method.

SO spin-orbit.

SP single-particle.

VBM valence band maximum.

Zusammenfassung

Halbleiter sind Materialien, deren elektrische Leitfähigkeit kleiner als die von Leitern, aber größer als die von Isolatoren ist. Sie sind weit verbreitet als optische Sensoren, Stromquellen, Lichtsender und auch Festkörperlaser aufgrund ihrer Zuverlässigkeit, Kompaktheit und geringen Kosten. In den letzten Jahren haben kolloidale Halbleiter-Quantenpunkte (QDs) die Möglichkeit eröffnet, Halbleiter mithilfe von lösungsbasierten Verfahren mit niedriger Temperatur und großer Fläche in leistungsstarke und flexible Bauelemente zu integrieren. Kolloidale QDs sind eine Untergruppe der Halbleiter-Nanokristalle (NKs) und sind stark im Fokus in der Nanotechnologie. Die Größe der kolloidalen QDs beträgt normalerweise nicht mehr als 10 nm. In diesem Bereich spielen die Quanten- und die dielektrischen Begrenzungseffekte eine wesentliche Rolle, die dazu führen, dass sich die elektrischen und optischen Eigenschaften von denen des bulk-Materials unterscheiden. Ihre hochgradig einstellbaren elektronischen und optischen Eigenschaften basieren auf Größe, Form, Zusammensetzung und ihre mit molekularen Liganden unterschiedlicher Chemie funktionalisierten Oberflächen. Dies führt zu einer Vielzahl von Forschungs- und kommerziellen Anwendungen wie biologischen Bildgebung (Bioimaging), Solarzellen, LEDs, Diodenlaser und Transistoren. Die optischen Eigenschaften des Nanokristalls werden durch die sogenannte Feinstruktur (FS) bestimmt. Die Berechnung der FS ist sehr schwierig, da die Kristallstruktur, die Spin-Orbit-Wechselwirkung und die Elektron-Loch-Austauschintegrale bererücksichtigt werden müssen. Atomistische Ansätze basierend auf semi-empirischen Pseudopotentialen [8, 9, 20, 38, 111] oder Tight-Binding [30, 32, 66, 69, 101] sind wahrscheinlich die genauesten, aber auch rechnerisch die teuersten. Bevor diese Methoden zur Verfügung standen, hatte ein dringender Bedarf an theoretischen Vorhersagen zu Modellen geführt, die auf der effektiven Massenannäherung [34] (EMA) basierten und lieferten einen guten Vergleich mit bestehenden Experimenten. Die Einfachheit der EMA-Modelle und der Erfolg bei der Vorhersage gemessener Eigenschaften führten zu der großen Beliebtheit des Ansatzes. Obwohl es immer möglich ist, experimentelle Ergeb-

nisse mit nur wenigen Parametern an effektive Massenmodelle anzupassen, bleibt häufig die Frage offen, ob die zugrunde liegende Physik gut erfasst wird. In dieser Arbeit werden die neu entwickelte Methode der atomar effektiven Pseudopotentiale (AEPs) und die Theorie der abgeschirmten Konfigurationswechselwirkung (CI) kombiniert, um die elektronischen und optischen Eigenschaften von NCs zu untersuchen.

Diese Arbeit ist in fünf Kapitel unterteilt. Kapitel 1 gibt einen allgemeinen Überblick über die Dichte Funktional Theorie (DFT) - eine der am häufigsten verwendeten theoretischen Methoden, die ein Verständnis der elektronischen Eigenschaften von kondensierter Materie bis hin zu Molekülen und Atomen ermöglicht. Wir präsentieren den Ursprung und die elegante Formulierung, die die Verwendung von DFT ermöglichen. DFT beinhaltet im Gegensatz zur Hartree-Fock-Methode Elektronenkorrelation und ist kostengünstig. DFT hat jedoch auch einige Nachteile. In DFT sind sehr viele verschiedene Basisästze und Funktionale verfügbar. Es kann nicht systematisch verbessert werden. Es kann nicht mit Systemen aus tausenden bis hunderttausenden Atomen umgehen. Kapitel 2 befasst sich mit der Beschreibung der atomar effektiven Pseudopotentialmethode (AEP). Die neu entwickelte Methode AEP [21, 61] basiert auf DFT und ermöglicht es uns, mit Systemen aus tausenden bis hunderttausenden Atomen umzugehen. Das atomar effektive Pseudopotential leitet sich aus einer analytischen Verbindung zwischen einem AEP und dem abgeschirmten selbstkonsistenten effektiven Potential von DFT ab. Die Qualität von AEPs wird in verschiedenen Materialien und Strukturen getestet. In Kapitel 3 wird eine empirische Korrektur der nichtlokalen Teile des Pseudopotentials eingeführt. Da die AEPs direkt aus der DFT unter Verwendung von der lokalen Dichtenäherung LDA für die Austauschkorrelationsfunktion erhalten werden, wird der typische Fehler aus der LDA, wie unterschätzte Bandlücken und effektive Massen, an die AEPs weitergegeben. Die einfache Korrektur ermöglicht uns genaue Quasiteilchen-Bandlücken und effektive Massen zu berechnen. Kapitel 4 enthält eine allgemeine Einführung in die Konfigurationswechselwirkungsmethode (CI) und das Verfahren zur Untersuchung der elektronischen und optischen Eigenschaften kolloidaler Nanokristalle. Kapitel 5 widmet sich den Ergebnissen zur exzitonischen Feinstruktur von kolloidalen CdSe-, InP- und HgTe-Nanokristallen. Aufgrund der hohen Lumineszenz und der guten Quantenausbeute ist CdSe eines der beliebtesten Materialien im Quantenpunktbereich. Die hochwertigen CdSe-basierten Quantenpunkte sind vielversprechende Kandidaten als fluoreszierende Tags für Einzelelektronentransistoren in der biologischen Bildgebung, Leuchtdioden, Lasermaterialien und Solarzellenanwendungen [25, 59, 64, 89]. InP-NCs haben vergleichbare optische Eigenschaften wie CdSe-NCs. InP-NCs wurden jedoch erst seit kurzem intensiv untersucht dank neuer Syntheseprotokolle auf der Basis eines billigen und einfach zu verwendenden Phosphorvorläufers, der zu hochwertigen InP-NCs führt [11, 100, 105]. In einem anderen Anwendungsbereich haben sich HgTe-NCs als vielversprechendes Material für die Infrarot-Bildgebungstechnologie herausgestellt. [70], Unsere theoretische Studie zu den optischen Eigenschaften von HgTe-NCs liefert wertvolle Einblicke in dieses neue Material.

Abstract

Semiconductors are materials whose electrical conductivity is smaller than that of conductors but larger than that of insulators. They are widely used as optical sensors, power devices, light emitters and also including the solid-state lasers because of their reliability, compactness, and low cost. In recent years, colloidal semiconductors quantum dots (QDs) open up opportunities to integrate semiconductors into high-performance and flexible devices by using low-temperature, large-area and solution-based methods. Colloidal QDs are a subset of semiconductor NCs and are the central topic of nanotechnology. The size of colloidal QDs is normally no more than 10 nm. In this regime the quantum and the dielectric confinement effects play essential roles leading to the difference in electric and optical properties from those of bulk materials. Their highly tunable electronic and optical properties based on size, shape, composition and their, with molecular ligands of diverse chemistry, functionalized surfaces lead to a variety of research and commercial applications such as bioimaging, solar cells, LEDs, diode lasers, and transistors. The optical properties of the nanocrystal are governed by the so-called fine structure (FS). The calculation of the FS is very challenging, as it requires a proper treatment of the crystal structure, the spin-orbit (SO) interaction, and the electron-hole exchange integrals. Atomistic approaches based on semi-empirical pseudopotential (SEP) [8, 9, 20, 38, 111] or tight-binding [30, 32, 66, 69, 101] are probably the most accurate, but also computationally the most expensive. Before these methods became available, an urgent need for theoretical predictions had led to models based on the effective mass approximation (EMA) [34], which yield a good comparison with existing experiments. The simplicity of the EMA models and the success in predicting measured properties led to the large popularity of the approach. However, while it is always possible to fit experimental results to effective mass models with only a few parameters, the question often remains if the underlying physics is well captured. In this work, the newly developed atomic effective pseudopotential (AEP) method and the screened configuration interaction (CI) theory are combined to investigate the electronic and optical properties of NCs.

This thesis is divided into five chapters. Chapter 1 gives a general overview of density-functional theory (DFT)-one of the most used theoretical methods which allow an understanding of the electronic properties from condensed matter to molecules and atoms. We present the origin and the elegant formulation which enable the use of DFT. Though DFT has quite a few advantages such as including electron correlation unlike the Hartree-Fock method, being cost-efficient, etc. Some disadvantages make DFT less powerful for example: there are many functionals available in DFT, it can not be systematically improved, it can not deal with systems consisting of thousands to hundreds of thousands atoms. Chapter 2 focuses on the description of the AEP method. The AEP method [21, 61] is based on DFT, and allows us to cope with systems of thousands to hundred thousand atoms. The AEP is derived from an analytic connection to the screened self-consistent effective potential of DFT. The quality of AEPs is tested in various materials and structures. In chapter 3, an empirical correction of the non-local parts of the pseudopotential is introduced. As the AEPs are directly obtained from DFT using the local density approximation (LDA) for exchange-correlation functional, the typical error from LDA, such as underestimated band gaps and effective masses, are inherited by the AEPs. The simple correction enables us to get accurate quasi-particle band gaps and effective masses. Chapter 4 provides a general introduction to the CI method and the procedure used to study the electronic and optical properties of colloidal NCs. Chapter 5 is devoted to the results on the excitonic fine structure of CdSe, InP and HgTe colloidal nanocrystals. Because of high luminescence and good quantum yield, CdSe is one of the most popular materials in the QD area. The high-quality CdSe-based QDs are promising candidates for fluorescent tags in biological imaging, single-electron transistors, light-emitting diodes, laser materials and solar cell applications. InP NCs have comparable optical properties with CdSe NCs. However, InP NCs have been intensively investigated since just recently thanks to new synthesis protocols based on a cheap and easy-to-use phosphorus precursor that leads to high-quality InP NCs [11, 100, 105]. In another field of application, HgTe NCs has emerged as a promising material for infrared imaging technology [70]. Our theoretical study on the optical properties of HgTe NCs provides valuable insight into this new material.

Introduction

Colloidal quantum dot (QD) (free-standing QDs) have opened the door to new and exciting spectroscopic studies of quantum structures due to their exciting features such as quantum-dot shape-dependent transitions, size-dependent (red) shifts between absorption and emission, emission from high excited levels, surface-mediated transitions, exchange splitting, strain-induced splitting, and Coulomb-blockade transitions. It is essential to understand the way the single-particle (SP) levels of the dot reflect the quantum size, quantum shape, interfacial strain, and surface effects and the nature of the many-particle interactions such as electron-hole exchange, electron-hole Coulomb effects, and electron-electron Coulomb interaction.

There have been several theoretical tools developed for analyzing the electronic structure of QDs. The first approach is the EMA and its extension called **k.p**, where **k** is the wave vector and **p** is the momentum. In the empirical pseudopotential method (EPM) and the semi-empirical pseudopotential method (SEPM) the dangling bonds at the surface of the QDs are passivated by ligandlike potentials, which are designed to remove the surface states from the band-gap and minimize the coupling with the band-edge states [38, 39, 41, 117]. AEP is the most recent method which is free of adjustable parameters, and the surface of the QDs is terminated by hydrogen or pseudo hydrogen, which allows for an accurate description of the surface effect. In this thesis, the results of the AEP method are presents in comparison with experiments and other theoretical methods.

Chapter 1

Basics of Ab-initio electronic structure calculations

1.1 Many-body problem and Born-Oppenheimer approximation

To understand the physical properties of materials, physicists have developed many different methods. Ab-initio methods, which require only a specification of the atomic numbers, have been used to calculate and predict efficiently many properties of solids, such as the total energy, the equilibrium lattice constants, elastic constants, vibrational frequencies. In combination with other theories, ab-initio methods can be applied to investigate the optical properties of materials. In quantum mechanics, a physical system can be described by the time-independent, non-relativistic Schrödinger equation

$$\hat{H}\Psi = E\Psi, \tag{1.1}$$

where Ψ and E are the wave function and total energy of the system, respectively. $\hat{H}$ is a differential operator whose expectation value is the total energy, in SI units:

$$\begin{aligned} \hat{H} = & -\frac{\hbar^2}{2}\sum_{\mathrm{A}}\frac{\nabla^2_{\mathbf{R}_A}}{M_A} - \frac{\hbar^2}{2}\sum_{i}\frac{\nabla^2_{\mathbf{r}_i}}{m_{\mathrm{e}}} \\ & - \frac{1}{4\pi\epsilon_0}\sum_{A,j}\frac{e^2 Z_A}{\mid \mathbf{R}_A - \mathbf{r}_j \mid} + \frac{1}{8\pi\epsilon_0}\sum_{\substack{i,j \\ i\neq j}}\frac{e^2}{\mid \mathbf{r}_i - \mathbf{r}_j \mid} + \frac{1}{8\pi\epsilon_0}\sum_{\substack{A,B \\ A\neq B}}\frac{e^2 Z_A Z_B}{\mid \mathbf{R}_A - \mathbf{R}_B \mid}. \end{aligned} \tag{1.2}$$

In this expression M_A denotes the mass of the Ath nucleus at the position $\mathbf{R}_A$ and m_i is the mass of the ith electron at the position $\mathbf{r}_i$. The first two terms are the kinetic energies of nuclei and electrons, other terms describe the Coulomb interactions between electrons and nuclei, between the electrons and between the nuclei, respectively. ϵ_0 is the permittivity of vacuum. The Schrödinger equation of the Hamiltonian (1.2) is almost unsolvable neither analytically nor numerically. It is necessary to introduce approximations in order to make this problem more tractable. The first approximation invoked is the Born-Oppenheimer approximation, which was proposed in 1927 by Max Born and J. Robert Oppenheimer [12]. The idea of this approximation is that since the mass of an electron is much smaller than that of a proton ($m_\mathrm{p}/m_\mathrm{e} \geq 1836$), electrons respond almost instantaneously to ionic motion. Thus nuclei can be treated adiabatically, leading to a separation of nuclear and electronic components of the many-body wave function

$$\Psi(\mathbf{r}_i, \mathbf{R}_A) = \psi(\mathbf{r}_i, \{\mathbf{R}_A\})\phi(\mathbf{R}_A), \tag{1.3}$$

where $\psi(\mathbf{r}_i, \{\mathbf{R}_A\})$ is the electronic wave function in a frozen ion configuration $\{\mathbf{R}_A\}$ and $\phi(\mathbf{R}_A)$ is the ionic wave function. $\phi(\mathbf{R}_A)$ is the solution of the equation

$$H_\mathrm{nuclei}\phi(\mathbf{R}_A) = E_\mathrm{nuclei}\phi(\mathbf{R}_A), \tag{1.4}$$

with H_nuclei is the Hamiltonian describing the nuclear motion under the influence of the Coulomb potential and the time-averaged adiabatic electronic potential. $\psi(\mathbf{r}_i, \{\mathbf{R}_A\})$ satisfies the Schrödinger equation for electrons

$$\begin{aligned}\Bigg(&- \frac{\hbar^2}{2}\sum_i \frac{\nabla^2_{\mathbf{r}_i}}{m_\mathrm{e}} - \frac{1}{4\pi\epsilon_0}\sum_{A,j}\frac{e^2 Z_A}{\mid \mathbf{R}_A - \mathbf{r}_j \mid} + \frac{1}{8\pi\epsilon_0}\sum_{\substack{i,j\\ i\neq j}}\frac{e^2}{\mid \mathbf{r}_i - \mathbf{r}_j \mid} \\ &+ \frac{1}{8\pi\epsilon_0}\sum_{\substack{A,B\\ A\neq B}}\frac{e^2 Z_A Z_B}{\mid \mathbf{R}_A - \mathbf{R}_B \mid}\Bigg)\psi(\mathbf{r}_i, \{\mathbf{R}_A\}) = E_\mathrm{el}\psi(\mathbf{r}_i, \{\mathbf{R}_A\}).\end{aligned} \tag{1.5}$$

Even though the Born-Oppenheimer approximation makes the many-body problem much simpler, it is still a challenge to solve the Schrödinger equation (1.5), and it is now the task of numerical electronic structure theory.

1.2 Exchange and correlation

The toughest part of any electronic structure calculation is the need of taking into account the electron-electron interaction which is described by exchange and correlation energies. The exchange interaction is a quantum mechanical effect and is present in any identical particle system. As electrons are Fermions, the wave function of a many-electron system must change its sign under the exchange of any two electrons, leading to an increase of the distance between two electrons with the same spin. This spatial separation reduces the total Coulomb energy of the system and this reduction is defined as the exchange energy of the electronic system. The first atomic calculation including the exchange interaction between electrons is the well-known Hartree-Fock method. [52], [37].

The correlation energy describes how much one electron is affected by all other electrons. Mathematically the correlation energy of an electronic system is the difference between its exact total energy and its total energy calculated using the Hartree-Fock approximation. In most cases, it is extremely hard to compute the correlation energy of a system and an approximation is undoubtedly needed for a correlation energy calculation.

1.3 Density functional theory

DFT is one of the most used methods nowadays to calculate the electronic properties of atoms, molecules, and condensed systems. The foundations of DFT are the Hohenberg-Kohn and Kohn-Sham theorems [53] with the elegant formulation of Kohn and Sham [65] in which both exchange and correlation effects are taken into account. Unlike traditional electronic structure methods, in DFT, instead of the many-body wave function, the one-body density is used as the only one fundamental variable. Since the density $\rho(\mathbf{r})$ is a function of only three spatial coordinates (rather than the 3N coordinates of the wave-function), density functional theory is computationally feasible even for large systems.

1.3.1 Hohenberg-Kohn theorems

DFT was established by two Hohenberg-Kohn theorems. The first theorem, which is disarmingly simple to prove using reductio ad absurdum, states that the external potential $V_{\text{ext}}(\mathbf{r})$ of an electronic system corresponds to a ground state electron density $\rho_0(\mathbf{r})$ (to within a constant). The external potential $V_{\text{ext}}(\mathbf{r})$ is generally defined by $\{N_A, \mathbf{R}_A\}$, therefore, the ground state density $\rho_0(\mathbf{r})$ contains information about $\{N, N_A, \mathbf{R}_A\}$, here N_A is the number of atoms and N is the number of electrons. We have the following chain

$$\rho_0(\mathbf{r}) \Rightarrow \{N, N_A, \mathbf{R}_A\} \Rightarrow \hat{H} \Rightarrow \Psi_0 \Rightarrow E_0 \text{ and other properties.}$$

The ground state energy is the sum of the ground state kinetic energy T, the potential energy due to the interaction between electrons E_{ee} and the potential energy due to the interaction between electron and the external potential E_{ext}.

$$E_0[\rho_0(\mathbf{r})] = T[\rho_0(\mathbf{r})] + E_{\text{ee}}[\rho_0(\mathbf{r})] + E_{\text{ext}}[\rho_0(\mathbf{r})], \tag{1.6}$$

where $E_{\text{ext}}[\rho_0] = \int \rho_0(\mathbf{r}) V_{\text{ext}} d\mathbf{r}$ depends on the actual system while the first two term are universal in the sense that they do not depend on $\{N_A, \mathbf{R}_A\}$. It is convenient to introduce the Hohenberg-Kohn functional

$$F_{\text{HK}}[\rho_0(\mathbf{r})] = T[\rho_0(\mathbf{r})] + E_{\text{ee}}[\rho_0(\mathbf{r})], \tag{1.7}$$

which describes the universal part of the ground state energy and is the same for every electronic system. The Schrödinger equation of the many-electron problem could have been solved exactly if the functional $F_{\text{HK}}[\rho(\mathbf{r})]$ was known exactly. But unfortunately the form of both $T[\rho(\mathbf{r})]$ and $E_{\text{ee}}[\rho(\mathbf{r})]$ are not explicitly defined. The $E_{\text{ee}}[\rho(\mathbf{r})]$ is specially difficult to define as it includes the classical Coulomb energy (Hartree energy) $E_{\text{H}}[\rho(\mathbf{r})]$, the exchange and correlation interactions which are non-classical effects $E_{\text{ncl}}[\rho(\mathbf{r})]$

$$E_{\text{ee}}[\rho(\mathbf{r})] = E_{\text{H}}[\rho(\mathbf{r})] + E_{\text{ncl}}[\rho(\mathbf{r})]. \tag{1.8}$$

Determining the explicit expressions for $T[\rho(\mathbf{r})]$ and $E_{\text{ee}}[\rho(\mathbf{r})]$ is the major chalenge in DFT.

So far it has been established that the ground state density determines uniquely the external potential thus the Hamiltonian and all properties of interest of an electronic system. The question is, how do we know exactly if a certain density is the ground state density. The second Hohenberg-Kohn theorem gives an answer to that question. It states that the Hohenberg-Kohn functional $F_{\text{HK}}[\rho(\mathbf{r})]$ is minimised at the true ground state density ρ_0. It is nothing but the variational principle which can be expressed as

$$E[\rho_0(\mathbf{r})] \leq E[\rho(\mathbf{r})] = T[\rho(\mathbf{r})] + E_{\mathrm{H}}[\rho(\mathbf{r})] + E_{\mathrm{ncl}}[\rho(\mathbf{r})] + E_{\mathrm{ext}}[\rho(\mathbf{r})]. \tag{1.9}$$

It is noteworthy that this strategy can not be straightforwardly transferred to the electronically excited problem.

1.3.2 Kohn-Sham equations

Practically it is not straightforward to solve the many-body problem within the Hohenberg-Kohn formalism because this approach gives no information about how to construct the universal functional $F_{\mathrm{HK}}[\rho_0(\mathbf{r})]$. Among three components of $F_{\mathrm{HK}}[\rho_0(\mathbf{r})]$, except for the electrostatic term $E_{\mathrm{H}}[\rho(\mathbf{r})]$, which can be expressed explicitly, the other two, $T[\rho_0(\mathbf{r})]$ and $E_{\mathrm{ncl}}[\rho(\mathbf{r})]$, are completely unknown and usually calculated approximately. There were some methods sugessted before DFT, the two most well-known are the Hartree approach, in which $E_{\mathrm{ncl}}[\rho(\mathbf{r})]$ is completely neglected, and the Thomas-Fermi approach in which $T[\rho(\mathbf{r})]$ is represented in terms of a density functional [35, 106]. These approaches, however, are too rude and usually produce inaccurate results.

About one year after the two Hohenberg and Kohn theorems were stated, in 1965, Kohn and Sham suggested a method to approximate the unknown universal functional by introducing an auxiliary system of non-interacting electrons which has the same ground state density as the interacting one. The very clever idea of Kohn and Sham is to compute the true kinetic energy by separating it into two parts, the main part is equal to the kinetic energy of the non-interacting reference system $T_{\mathrm{S}}[\rho(\mathbf{r})]$ and the smaller remainder $T_{\mathrm{C}}[\rho(\mathbf{r})]$ has to be dealt approximately. The universal functional $F_{\mathrm{HK}}[\rho(\mathbf{r})]$ thus can be presented as

$$F_{\mathrm{HK}}[\rho(\mathbf{r})] = T_{\mathrm{S}}[\rho(\mathbf{r})] + E_H[\rho(\mathbf{r})] + E_{\mathrm{XC}}[\rho(\mathbf{r})], \tag{1.10}$$

where $E_{\mathrm{XC}}[\rho(\mathbf{r})]$, the so-called exchange-correlation energy, is defined by equation (1.10) itself.

$$E_{\mathrm{XC}}[\rho(\mathbf{r})] = (T[\rho(\mathbf{r})] - T_{\mathrm{S}}[\rho(\mathbf{r})]) + E_{\mathrm{ncl}}[\rho(\mathbf{r})] = T_{\mathrm{C}}[\rho(\mathbf{r})] + E_{\mathrm{ncl}}[\rho(\mathbf{r})]. \tag{1.11}$$

$E_{\mathrm{XC}}[\rho(\mathbf{r})]$ contains not only the non-classical effects but also a part of the kinetic energy. Up to this point, $E_{\mathrm{XC}}[\rho(\mathbf{r})]$ is the only energy contribution we do not know how to handle exactly. The total energy of the electronic system can be written as (in atomic unit)

$$\begin{aligned}E[\rho(\mathbf{r})] &= T_{\mathrm{S}}[\rho(\mathbf{r})] + E_H[\rho(\mathbf{r})] + E_{\mathrm{XC}}[\rho(\mathbf{r})] + E_{\mathrm{ext}}[\rho(\mathbf{r})] \\ &= T_{\mathrm{S}}[\rho(\mathbf{r})] + \frac{1}{2}\int\int \frac{\rho(\mathbf{r}_1)\rho(\mathbf{r}_2)}{r_{12}} d\mathbf{r}_1 d\mathbf{r}_2 + E_{\mathrm{XC}}[\rho(\mathbf{r})] + \int V_{\mathrm{ext}}\rho(\mathbf{r})d\mathbf{r} \\ &= -\frac{1}{2}\sum_i^N \langle\psi_i|\nabla^2|\psi_i\rangle + \frac{1}{2}\sum_i^N\sum_j^N \int\int \mid \psi_i(\mathbf{r}_1)\mid^2 \frac{1}{r_{12}} \mid \psi_j(\mathbf{r}_2)\mid^2 d\mathbf{r}_1 d\mathbf{r}_2 \\ &+ E_{\mathrm{XC}}[\rho(\mathbf{r})] - \sum_i^N \int \sum_A^{N_A} \frac{Z_A}{r_{iA}} \mid \psi_i(\mathbf{r}_1)\mid^2 d\mathbf{r}_1. \end{aligned} \tag{1.12}$$

Minimizing the energy functional $E[\rho(\mathbf{r})]$ defined by equation (1.12), with the constraint that $\langle\psi_i|\psi_j\rangle = \delta_{ij}$, is equivalent to solving the set of self-consistent equations

$$\left[-\frac{1}{2}\nabla^2 + \left(\int \frac{\rho(\mathbf{r}_2)}{r_{12}} d\mathbf{r}_2 + V_{\mathrm{XC}}(\mathbf{r}_1) - \sum_A^{N_A} \frac{Z_A}{r_{iA}}\right)\right]\psi_i = \left[-\frac{1}{2}\nabla^2 + V_{\mathrm{KS}}(\mathbf{r}_1)\right]\psi_i = \epsilon_i\psi_i. \tag{1.13}$$

Equations (1.13) is the well-known Kohn Sham equations, V_{XC} is the potential due to the exchange-correlation energy E_{XC} and simply defined as the functional derivative of E_{XC} with respect to $\rho(\mathbf{r})$

$$V_{\mathrm{XC}} = \frac{\delta E_{\mathrm{XC}}}{\delta\rho(\mathbf{r})}. \tag{1.14}$$

If E_{XC} were known then the Kohn Sham equation could be solved exactly and self-consistently. Unfortunately, there is no way to determine E_{XC} explicitly and it becomes the primary goal of DFT to find better and better approximations to calculate E_{XC}.

1.3.3 Local density approximation

So far DFT allows an exact description of the major part the electronic energy of a system. All remaining unknown parts are collectively presented by the exchange-correlation term $E_{\mathrm{XC}}[\rho(\mathbf{r})]$. To solve the Schrodinger equation using the Kohn-Sham formalism we need to know the form of $E_{\mathrm{XC}}[\rho(\mathbf{r})]$ so the quality of DFT will be judged by the accuracy of the chosen approximation to $E_{\mathrm{XC}}[\rho(\mathbf{r})]$. The simplest approximation of describing the exchange-correlation functional of an electronic system is the LDA which was already included in the original paper by Kohn-Sham [65] and have been widely used for solid systems. In LDA the exchange-correlation energy of an electronic system is constructed by assuming that the exchange-correlation energy per electron at a position $\mathbf{r}$ in the electronic system, $\varepsilon_{\mathrm{XC}}[\rho(\mathbf{r})]$, equal to the exchange-correlation energy per electron in a homogeneous electron gas, $\varepsilon_{\mathrm{XC}}^{\mathrm{hom}}[\rho(\mathbf{r})]$, that has the same density as the electronic system at $\mathbf{r}$. Therefore, $E_{\mathrm{XC}}[\rho(\mathbf{r})]$ can be written in a very simple form as following

$$E_{\mathrm{XC}}^{\mathrm{LDA}}[\rho(\mathbf{r})] = \int \rho(\mathbf{r})\varepsilon_{\mathrm{XC}}[\rho(\mathbf{r})]d\mathbf{r}. \tag{1.15}$$

The potential due to the exchange-correlation energy (1.14) now becomes

$$V_{\mathrm{XC}} = \frac{\delta E_{\mathrm{XC}}}{\delta\rho(\mathbf{r})} = \frac{\partial\left[\rho(\mathbf{r})\varepsilon_{\mathrm{XC}}[\rho(\mathbf{r})]\right]}{\partial\rho(\mathbf{r})}. \tag{1.16}$$

The exchange-correlation energy per electron $\varepsilon_{\mathrm{XC}}[\rho(\mathbf{r})]$ includes the exchange and the correlation contributions

$$\varepsilon_{\mathrm{XC}}[\rho(\mathbf{r})] = \varepsilon_{\mathrm{X}}[\rho(\mathbf{r})] + \varepsilon_{\mathrm{C}}[\rho(\mathbf{r})], \tag{1.17}$$

where the exchange energy per electron of the homogeneous electron gas, $\varepsilon_{\mathrm{X}}^{\mathrm{hom}}[\rho(\mathbf{r})] = \varepsilon_{\mathrm{X}}[\rho(\mathbf{r})]$, is described by the Slater approximation based on the Hartree-Fock method and is usually called Slater exchange

$$\varepsilon_{\mathrm{X}}[\rho(\mathbf{r})] = -\frac{3}{4}\sqrt[3]{\frac{3\rho(\mathbf{r})}{\pi}}. \tag{1.18}$$

There is no similar way to express the correlation contributions explicitly. However, the functional form of the correlation energy has been parametrized from the highly accurate numerical quantum Monte-Carlo simulations of the homogeneous electron gas which had done by Ceperly and Alder in 1980. One of the most well-known representations of $\varepsilon_{\mathrm{C}}[\rho(\mathbf{r})]$ was developed by Perdew and Zunger in 1981 [93]. Later, in 1992, Perdew and Wang provided a simple analytic representation of $\varepsilon_{\mathrm{C}}[\rho(\mathbf{r})]$ which is widely used [92]. For solid systems which are weakly correlated, LDA and its extension, the local spin density approximation (LSDA) to deal with the spin-polarized systems, work surprisingly well and provide an accurate description of structural and vibrational properties such as lattice constants, bulk moduli and phonon vibrational frequencies. For the cohesive energy of solids, the dissociation energy of molecules and the ionisation energy of atoms, LDA becomes less accurate; thus, further development of LDA were required for those calculations. LDA assumes that the exchange-correlation energy functional is local and depend only on $\rho(\mathbf{r})$. It is, in principle, ignores the effect of inhomogeneities of the electron density. In the generalised gradient approximation (GGA) where $\varepsilon_{\mathrm{XC}}[\rho(\mathbf{r})]$ depends not only on $\rho(\mathbf{r})$ but also on the gradient of $\rho(\mathbf{r})$, $\nabla\rho(\mathbf{r})$, the non-homogeneity of the true electron density is taken into account. GGA, therefore, made a high impact in computational chemistry where cohesive and dissociation energies play important roles. Another extension of LDA is the hybrid approximation proposed by A. Becke in 1993 [7] in which a portion of exact exchange from Hartree-Fock theory is incorporated with the rest of the exchange-correlation energy from other sources (ab initio or empirical). The hybrid functional is mostly used in chemistry.

1.4 Periodic supercells and plane-wave pseudopotential method

The many-body problem has been mapped into an effective single-particle problem. By expanding the electronic wave function into a basis set, the integro-differential Kohn-Sham equation is transformed into an algebraic one. However, it is still challenging to solve the Kohn-Sham equation since the electronic wave functions extends over the entire solid and the basis set required is in principle infinite. Some widely used basis set are, for example, Gaussian functions, atomic orbitals, plane-waves, etc. In our work, we use the plane-wave basis set, and it will be discussed in this section.

Bloch's theorem states that in a perfectly periodic system the electronic wave function can be written as

$$\psi_i(\mathbf{r}) = e^{i\mathbf{k}\mathbf{r}} f_i(\mathbf{r}), \tag{1.19}$$

here $f_i(\mathbf{r})$ is a periodic function with the same periodicity as the system and can be expanded in terms of a discrete plane-wave basis set whose wave vector are reciprocal space vector of crystal

$$f_i(\mathbf{r}) = \sum_{\mathbf{G}} c_{i,\mathbf{G}} e^{i\mathbf{G}\mathbf{r}}. \tag{1.20}$$

Therefore each electronic wave function can be written as a sum of plane-waves

$$\psi_i(\mathbf{r}) = \sum_{\mathbf{G}} c_{i,\mathbf{k}+\mathbf{G}} e^{i(\mathbf{k}+\mathbf{G})\mathbf{r}}. \tag{1.21}$$

In principle, an infinite number of plane-wave is needed to expand an electronic wave function. However, since the coefficient $c_{i,\mathbf{k}+\mathbf{G}}$ of the plane-waves which have small kinetic energy $(\hbar^2/2m)|\mathbf{k}+\mathbf{G}|^2$ are much more important than that of plane-waves which have a large kinetic energy, in practice, the plane-wave basis set is truncated at a certain value of kinetic energy E_{cut} and only plane-waves with the kinetic energy smaller than E_{cut} will be included in the basis. This truncation leads to an error in the total energy. Nevertheless, the error can be reduced by increasing the value of E_{cut}. One can study the convergence of the total energy with respect to E_{cut} and decide about the accuracy of the calculations.

Using Bloch's theorem, instead of calculating an infinite number of the electronic wave function, one needs to calculate a finite electronic wave function at an infinite number of k point. However, as the electronic wave functions at k points that are very close together are almost identical, it is possible to represent the electronic wave functions in a region of k space by electronic wave functions at a finite number of k point. The error introduced by this k point sampling, like the case of E_{cut}, can be controlled by studying the convergence of the total energy with respect to the number of k point. In insulator or semiconductor, highly accurate calculations can be done with a small number of k point, but it requires a denser k point for metallic because of the requirement of defining the Fermi surface precisely.

Using plane-waves basis set the Kohn-Kham equation (1.13) reads

$$\sum_{\mathbf{G}'} \langle \mathbf{k}+\mathbf{G}'|H_{\text{KS}}|\mathbf{k}+\mathbf{G}\rangle \, c_{i,\mathbf{k}+\mathbf{G}} = \epsilon_i \sum_{\mathbf{G}'} \langle \mathbf{k}+\mathbf{G}'|\mathbf{k}+\mathbf{G}\rangle = \epsilon_i c_{i,\mathbf{k}+\mathbf{G}}. \tag{1.22}$$

The matrix element of the Kohn-Sham Hamiltonian H_{KS} includes two parts. The kinetic energy part is diagonal

$$\langle \mathbf{k}+\mathbf{G}'| -\frac{\hbar^2}{2m}\nabla^2|\mathbf{k}+\mathbf{G}\rangle = \frac{\hbar^2}{2m}|\mathbf{k}+\mathbf{G}|^2\delta_{\mathbf{G}\mathbf{G}'}, \tag{1.23}$$

and the Kohn-Sham potential part is presented in terms of its Fourier transform

$$\langle \mathbf{k}+\mathbf{G}'|V_{\text{KS}}(r)|\mathbf{k}+\mathbf{G}\rangle = V_{\text{KS}}(\mathbf{G}-\mathbf{G}'). \tag{1.24}$$

The Kohn-Kham equation at a given k vector in matrix form is

$$\sum_{\mathbf{G}'} \left[\frac{\hbar^2}{2m}|\mathbf{k}+\mathbf{G}|^2\delta_{\mathbf{G}\mathbf{G}'} + V_{\text{KS}}(\mathbf{G}-\mathbf{G}')\right] c_{i,\mathbf{k}+\mathbf{G}'} = \epsilon_i c_{i,\mathbf{k}+\mathbf{G}}, \tag{1.25}$$

with the matrix elements $H_{\mathbf{k}+\mathbf{G},\mathbf{k}+\mathbf{G}'}$ are given by

$$H_{\mathbf{k}+\mathbf{G},\mathbf{k}+\mathbf{G}'} = \frac{\hbar^2}{2m}|\mathbf{k}+\mathbf{G}|^2\delta_{\mathbf{G}\mathbf{G}'} + V_{\mathrm{KS}}(\mathbf{G}-\mathbf{G}'). \tag{1.26}$$

Solving Kohn-Sham equation at this point corresponds to diagonalising the Kohn-Sham Hamiltonian matrix which has the size defined by the energy cut off E_{cut}.

The plane-wave method is in general developed for a periodic system. The systems which have a defect or is lack of periodicity such as quantum dots, quantum wires, slabs, in principle need to be extented in a continuous plane-wave basis set and the plane-wave method becomes unsolvable. This formidable task can be tackled by using a periodic supercell so that the nonperiodic system is located inside the supercell and artificially repeated in space to form a periodic system which is suitably studied by plane-wave method and the energy per unit cell of a crystal containing an array of supercells is calculated. The supercell for a point-defect system is illustrated in figure 1.1a, the bulk region surrounding the point-defect need to be enough to ensure that there is no interaction between defects from different supercells. Nanostructures or molecules can also be studied in this fashion by making supercell with enough vacuum surrounding systems. An example of a supercell for a quantum dot is schematically presented in figured 1.1b.

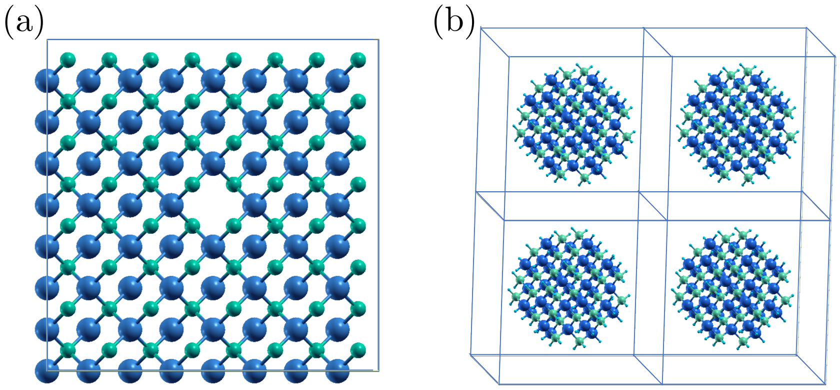

Figure 1.1: Supercell geometry for a point-defect (vacancy) in a bulk solid (a) and for a quantum dot (b).

As most of the physical properties of a system depend on valence electrons only, we can treat core and valence electron separately. The core electrons are those in the filled orbitals, strongly localised and can be treated together with the nuclei as the so-called ion cores. The valence electrons are in incompletely filled shells and more mobile.

Because of the strong ionic potential induced by the ion cores via Coulomb interaction, the electronic wave function of valence electron oscillates rapidly in the core region leading to the need for a vast number of plane-wave basis set to expand the electronic wave functions and hence make plane-wave method impractical. To tackle this problem we need to use the so-called pseudopotential approximation. In this approximation the strong ionic potential is replaced by a much smoother and weaker pseudopotential which acts on the pseudo wave function instead of the real wave function of valence electrons. The pseudopotential is constructed ideally so that the scattering properties are preserved and in such a way that the pseudo wave functions are nodeless. Beyond a certain radius cutoff r_{C} the pseudopotential and the real potential are identical.

The two most widely used forms of pseudopotential are norm-conserving pseudopotential and ultrasoft pseudopotential. The norm-conserving pseudopotential was first time introduced by D. Hamann, M. Schlüter, and C. Chiang. [50] and satisfy four criteria:
(i) Real and pseudo valence eigenvalues agree for the reference configuration.
(ii) Real and pseudo atomic wave functions agree beyond a chosen "core radius" r_{C}.
(iii) The integrals from 0 to r of the real and pseudo charge densities agree for $r > r_{\mathrm{C}}$ for each valence state (norm conservation).
(iv)) The logarithmic derivatives of the real and pseudo wave function and their first energy derivatives agree for $r > r_{\mathrm{C}}$.
These criteria guarantee the high transferability and the preserved scattering properties of pseudopotential. The most common form of pseudopotential is

$$V_{SL} = \sum_{lm} |Y_{lm}\rangle V_{\mathrm{NL}}(r) \langle Y_{lm}|. \tag{1.27}$$

In this form, the pseudopotential is radially non-local but angularly local therefore it is called semi-local pseudopotential. In the plane-wave basis representation, the calculation of matrix elements of this pseudopotential is computationally very demanding. To deal with this difficulty, Kleinman and Bylander proposed a separate form for the non-local part of pseudopotential

$$V_{\mathrm{NL}} = \sum_{l} V_l^{\mathrm{NL}} = \sum_{lm} \frac{|V_l^{\mathrm{SL}} \phi_{lm}^{\mathrm{PS}}\rangle \langle \phi_{lm}^{\mathrm{PS}} V_l^{\mathrm{SL}}|}{\langle \phi_{lm}^{\mathrm{PS}} | V_l^{\mathrm{SL}} | \phi_{lm}^{\mathrm{PS}}\rangle}, \tag{1.28}$$

where V_l^{SL} is the local radial part of pseudopotential and ϕ_{lm}^{PS} are pseudo wave functions calculated on each atom. This derivation allows fewer calculations for the matrix element of the non-local part of pseudopotential.

The ultrasoft pseudopotential was suggested by Vanderbilt [109] with the relaxing norm-conserving constraint in order to generate a smoother but still highly transferable pseudopotential. The ultrasoft pseudopotential is commonly used for elements, which have quite "hard" norm-conserving pseudopotential and require a sizeable plane-wave basis set for good representation, such as N, O, F and the first row of transition metals.

The general way of generating a pseudopotential for an atom is as follow: (i) The all-electron calculations are performed for the ground and some electronically excited states using a given form of exchange-correlation functional to obtain eigenvalues and eigenfunctions of valence electrons. (ii) The pseudopotential is then defined parametrically in such a way that the pseudo atom calculation using the same form of exchange-correlation as of the all-electron calculation gives the eigenvalues that are the same with eigenvalues of all-electron calculations and eigenfunctions that match eigenfunction in the all-electron calculation in the region where $r > r_{\mathrm{C}}$.

DFT with the use of plane-wave basis set has been developed and implemented in many codes over past decades. In this thesis, all DFT calculations are done with the code ABINIT, and the norm-conserving pseudopotentials are employed to study the electronic structure of Si, InP, and CdSe.

Chapter 2

Atomic effective pseudopotential for semiconductors

AEPs were derived by J. R. Cárdenas and G. Bester in 2012 [21] from an analytic connection between an AEP and the screened self-consistent effective potential of DFT. The main motivation of deriving AEPs is to save computational cost compared to ab initio calculations. It can be done because AEPs allows one to bypass the self-consistent procedure and in contrast to DFT, where the number of calculated eigenstates scales with the number of atoms, AEP allows consideration of a selected part of the eigenvalue spectrum. Therefore, using AEP, one can address structures with thousands to hundreds of thousands of atoms as given and most of nanostructures.

The idea to replace the strong Coulomb potential of the nucleus together with the bound electrons by an effective, weaker pseudopotential were introduced before. The first generation is the empirical pseudopotential method (EPM) [17, 18, 24, 26, 27, 94], in this method the empirical pseudopotentials were constructed to reproduce experimentally determined energy levels of the bulk crystals. The band structure and optical properties of the bulk system can be studied accurately with EPM. For nanostructures, an extension via interpolation to neighbouring points in G space was performed to improve the transferability of EPM [4, 23]. The second generation is the semiempirical pseudopotential method developed by Wang, Fu, and Zunger [40, 110]. In this approach, the semiempirical pseudopotentials were generated from DFT calculations with LDA for the bulk systems with several values of lattice parameter and a few different structures (wurtzite, zincblende). The local parts of the DFT potentials were transformed into G space and represented by a set of Gaussian functions. By construction, the semiempirical pseudopotential is not defined at small G vectors that are shorter than $2\pi/a_0$, where a_0 is the lattice parameter of the bulk system. However, this range becomes significantly essential in a nanostructure where the shortest relevant G vector is $2\pi/L$, where L is the size of the nanostructure. In practice, the Gaussian function was interpolated from the shortest known G vector to the $G = 0$ point and the pseudopotential at $G = 0$ point is adjusted to reproduce the experimentally determined quantities. SEPM with very low energy cut off was widely used to study the electronic and the optical properties of NCs [19, 20, 38, 44, 56, 57].

In this chapter, we introduce a new generation of the pseudopotential method, the AEP, in which the AEPs are derived via an analytic connection to the effective pseudopotential of DFT without any fitting procedure. The generated AEPs are highly transferable and efficiently used to study the electronic properties of bulk and nanostructures [21], [61].

2.1 Atomic effective pseudopotential for periodic systems

2.1.1 Analytic connection between AEPs and effective Kohn-Sham potentials for bulk systems

The bulk AEP construction requires two simple DFT calculations of slightly deformed elongated cells [21]. As already mentioned in the previous chapter, the cornerstone of DFT is the Kohn-Sham equation

$$\Big(-\frac{\hbar^2}{2m}\Delta + V_{\mathrm{KS}}(\mathbf{r})\Big)\psi_i(\mathbf{r}) = \epsilon_i \psi_i(\mathbf{r}),$$

where the effective Kohn-Sham potential $V_{\mathrm{KS}}(\mathbf{r})$ describes the interaction of an electron with its environment.

$$V_{\mathrm{KS}}(\mathbf{r}) = V_{\mathrm{ext}}(\mathbf{r}) + V_{\mathrm{Hartree}}[\rho(\mathbf{r})] + V_{\mathrm{XC}}[\rho(\mathbf{r})] \tag{2.1}$$

with

$$\rho(\mathbf{r}) = \sum_i^{occ} |\psi_i(\mathbf{r})|^2$$

is the electron density of all occupied states. Using the pseudopotential approximation, the external potential $V_{\text{ext}}(\mathbf{r})$ is replaced by a weaker one named as the pseudopotential $V(\mathbf{r})$. In the representation of angular momentum projectors, the local and non-local part of the pseudopotential can be written as

$$V_{\text{loc}}(\mathbf{r}) = \sum_{\alpha n} v^{\alpha}_{\text{loc}}(|\mathbf{r} - \boldsymbol{\tau}^{\alpha n}|), \tag{2.2}$$

$$V_{\text{nloc}}(\mathbf{r}) = \sum_{\alpha n}\sum_{lm} \delta v^{\alpha l}(|\mathbf{r} - \boldsymbol{\tau}^{\alpha n}|)\hat{P}^{\alpha n, lm}, \tag{2.3}$$

where α implies atom type and runs from 1 to N_{species}, n is the atom index, and runs from 1 to the number of atoms N_α for atom type α. $\boldsymbol{\tau}^{\alpha n}$ presents the atomic position and $\hat{P}^{\alpha n, lm}$ is the projection operator. In the Kleinman and Bylander form, the pseudopotential is rewritten as

$$V_{\text{KS}} = V_{\text{loc}}(\mathbf{r}) + V_{\text{Hartree}}[\rho] + V_{\text{XC}}[\rho] + \sum_{lm} |\chi^{lm}_{\text{KB}}\rangle E^{lm}_{\text{KB}} \langle \chi^{lm}_{\text{KB}}|, \tag{2.4}$$

where the last term is the nonlocal part of the potential, E^{lm}_{KB} are the Kleinman-Bylander eigenvalues and χ^{lm}_{KB} are the normalized Kleinman-Bylander projectors. During the self-consistent cycle of the Kohn-Sham equations the density is updated until the ground state density ρ^{scf} is found. The AEPs are constructed from the local part of the self-consistent effective Kohn-Sham potential

$$V_{\text{loc,KS}}(\mathbf{r}) = V_{\text{loc}}(\mathbf{r}) + v_{\text{Hartree}}[\rho^{scf}] + v_{\text{XC}}[\rho^{scf}]. \tag{2.5}$$

The potential v^{α}_{loc} defined in Eq. (2.2) is the norm-conserving pseudopotential constructed using the approach of Troullier and Martins [107]. The effective potential in reciprocal space is the Fourier transform of the effective potential in real space

$$V_{\text{loc,KS}}(\mathbf{G}) = \frac{1}{\Omega_{\text{c}}} \int_{\Omega_{\text{c}}} V_{\text{loc,KS}}(\mathbf{r}) e^{-i\mathbf{G}.\mathbf{r}} d^3 r, \tag{2.6}$$

where Ω_{c} is the volume of the unit cell. The effective potential in real space can be represented as a sum of atom-centered potentials

$$V_{\text{loc,KS}}(\mathbf{r}) = \sum_{\alpha}^{N_{\text{species}}} \sum_{n}^{N_\alpha} v_\alpha(\mathbf{r} - \boldsymbol{\tau}^{\alpha n}), \tag{2.7}$$

and transformed into reciprocal space as

$$V_{\text{loc,KS}}(\mathbf{G}) = \frac{1}{\Omega_{\text{c}}} \sum_{\alpha}^{N_{\text{species}}} \sum_{n}^{N_{\alpha}} v_{\alpha}(\mathbf{G}) e^{-i\mathbf{G}.\boldsymbol{\tau}^{\alpha n}} \tag{2.8}$$

where

$$v_{\alpha}(\mathbf{G}) = \int_{\infty} v_{\alpha}(\mathbf{r}) e^{-i\mathbf{G}.\mathbf{r}} d^3r \tag{2.9}$$

are the AEPs for different types of atoms.

2.1.2 AEPs construction

The AEPs of a binary system, including v_{a} for anion and v_{c} for cation, can be constructed indirectly through v_{+} and v_{-}

$$v_{+} = v_{\text{a}} + v_{\text{c}}, \tag{2.10}$$

$$v_{-} = v_{\text{a}} - v_{\text{c}}. \tag{2.11}$$

The effective local potential of a binary system is presented as the sum of anion and cation components

$$V^{(1)}_{\text{loc,KS}}(\mathbf{r}) = \sum_{i=1}^{N_{\text{a}}} v_{\text{a}}(\mathbf{r} - \boldsymbol{\tau}^{i}) + \sum_{j=1}^{N_{\text{c}}} v_{\text{c}}(\mathbf{r} - \boldsymbol{\tau}^{j}). \tag{2.12}$$

In the inverted structure, where atomic positions are fixed but anion and cation are interchanged, the effective local potential is

$$V^{(2)}_{\text{loc,KS}}(\mathbf{r}) = \sum_{i=1}^{N_{\text{c}}} v_{\text{c}}(\mathbf{r} - \boldsymbol{\tau}^{i}) + \sum_{j=1}^{N_{\text{a}}} v_{\text{a}}(\mathbf{r} - \boldsymbol{\tau}^{j}). \tag{2.13}$$

Two equations (2.12) and (2.13) simply lead to

$$\sum_{n=1}^{N_{\text{atoms}}} v_{+}(\mathbf{r} - \boldsymbol{\tau}^{n}) = V^{(1)}_{\text{loc,KS}}(\mathbf{r}) + V^{(2)}_{\text{loc,KS}}(\mathbf{r}) = V^{(1+2)}_{\text{loc,KS}}(\mathbf{r}), \tag{2.14}$$

and

$$\sum_{n=1}^{N_{\text{atoms}}} (-1)^{n+1} v_{-}(\mathbf{r} - \boldsymbol{\tau}^{n}) = V^{(1)}_{\text{loc,KS}}(\mathbf{r}) - V^{(2)}_{\text{loc,KS}}(\mathbf{r}) = V^{(1-2)}_{\text{loc,KS}}(\mathbf{r}). \tag{2.15}$$

The Fourier transforms of Eqs. (2.14) and (2.15) are as following

$$V_{\text{loc,KS}}^{(1+2)}(\mathbf{G}) = \frac{1}{\Omega}\int_{\Omega} V_{\text{loc,KS}}^{(1+2)}(\mathbf{r})e^{i\mathbf{G}.\mathbf{r}}d^3r = \frac{1}{\Omega}\sum_{n=1}^{N_{\text{atoms}}} e^{i\mathbf{G}.\boldsymbol{\tau}^n} v_+(\mathbf{G}), \tag{2.16}$$

$$V_{\text{loc,KS}}^{(1-2)}(\mathbf{G}) = \frac{1}{\Omega}\int_{\Omega} V_{\text{loc,KS}}^{(1-2)}(\mathbf{r})e^{i\mathbf{G}.\mathbf{r}}d^3r = \frac{1}{\Omega}\sum_{n=1}^{N_{\text{atoms}}} (-1)^{n+1}e^{i\mathbf{G}.\boldsymbol{\tau}^n} v_-(\mathbf{G}). \tag{2.17}$$

Though $v_+(\mathbf{G})$ and $v_-(\mathbf{G})$ are complex, within spherical approximation only real parts of $v_+(\mathbf{G})$ and $v_-(\mathbf{G})$ are of interest. The real components of $v_+(\mathbf{G})$ and $v_-(\mathbf{G})$ can be extracted from 2.16 and 2.17

$$V_{\pm}^{(\text{SA})}(|\mathbf{G}|) = Re[v_{\pm}(\mathbf{G})] = \Omega\Big[\frac{Re[V_{\text{loc,KS}}^{(1\pm2)}(\mathbf{G})]}{\beta_{\pm}} + \frac{Im[V_{\text{loc,KS}}^{(1\pm2)}(\mathbf{G})]}{\alpha_{\pm}}\Big] \times \Big(\frac{\beta_{\pm}\alpha_{\pm}}{\beta_{\pm}^2 + \alpha_{\pm}^2}\Big) \tag{2.18}$$

where

$$\begin{aligned}
\beta_+ &= \textstyle\sum_{i=1}^{N_{\text{atoms}}} sin(\mathbf{G}.\boldsymbol{\tau}^n),\\
\alpha_+ &= \textstyle\sum_{i=1}^{N_{\text{atoms}}} cos(\mathbf{G}.\boldsymbol{\tau}^n),\\
\beta_- &= \textstyle\sum_{i=1}^{N_{\text{atoms}}} (-1)^{n+1} sin(\mathbf{G}.\boldsymbol{\tau}^n),\\
\alpha_- &= \textstyle\sum_{i=1}^{N_{\text{atoms}}} (-1)^{n+1} cos(\mathbf{G}.\boldsymbol{\tau}^n).
\end{aligned}$$

The two effective local potentials $V_{\text{loc,KS}}^{(1)}(\mathbf{G})$ and $V_{\text{loc,KS}}^{(2)}(\mathbf{G})$ are generated from two [100] elongated 24 atoms supercells. One supercell can be obtained by inverting the atom positions of the other. A deformation of 5% is applied along slab direction to break the symmetry of the crystal and allow the extraction of long-range interaction. $V_{\text{loc,KS}}^{(1)}(\mathbf{G})$ and $V_{\text{loc,KS}}^{(2)}(\mathbf{G})$ generated from supercell calculation agree with that generated from the bulk unit-cell calculation for larger G vectors, at the point of the smallest G vector, G_{c}, of bulk unit-cell calculation the value of potential from slabs calculations and bulk unit-cell calculation have a small difference. To make AEPs more general and system independent a Gaussian correction was applied in order to have the same effective local potential at G_{c} in supercells and bulk unit-cell calculations. Supercells were chosen to be in [100] direction to allow for the extraction of $V_{-}^{(\text{SA})}(\mathbf{G})$ which disappears from the equation determining the effective local potential of the system in [110] direction. In DFT calculation, the average effective crystal potential $V(G = 0)$ of a periodic system is undefined and usually fixed to an arbitrary value. Therefore, the whole eigenvalue spectrum can be shifted corresponding to the value of $V(G = 0)$.

In heterostructure where the band offsets play a very important role, the band alignment need to be determined correctly. For that purpose, AEPs are linked together.

The construction of linked AEPs is base on two DFT calculations of two quantum wells (QWs) which comprise two types of material whose AEPs are needed to be linked. The lattice parameter is defined as the average of the lattice constants of the two materials. AEPs of the first material are generated simply by the procedure used for binary systems, AEPs of the second material are defined according to the AEPs of the first material. The linked and the binary AEPs are identical beyond G_c. The values of $V(G)$ at $G = 0$ and small G are adjusted to reproduce DFT calculation of deformation potential of the valence band. AEPs have been used in many types of materials with different structure (zincblende, wurtzite or rocksalt) [21]. The results show a high transferability of the AEPs and a very good agreement between AEPs and DFT calculations.

As a demonstration, figure 2.1 show the band structures of Zinc-blende InP and Wurtzite CdSe bulk systems obtained by DFT and AEP. It is shown that the band structures calculated using DFT and AEP are almost identical, presenting a very high quality of AEPs.

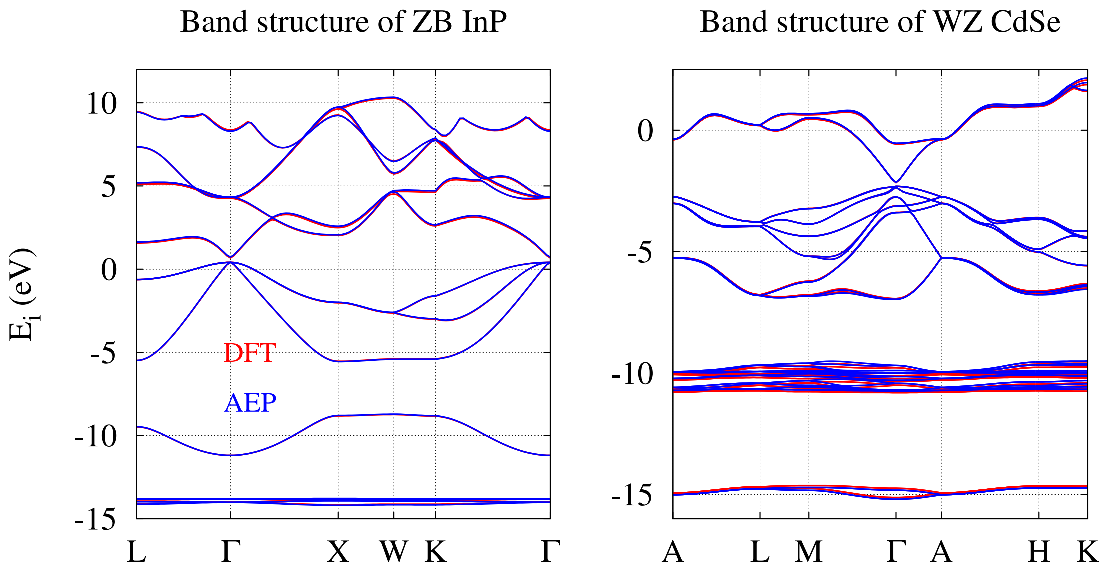

Figure 2.1: Band structure of Zinc-blende InP bulk and Wurtzite CdSe bulk. Red curves are DFT and blue curves are AEP result.

2.2 Atomic effective pseudopotential for nanocrystals

2.2.1 Analytic connection between AEPs and effective Kohn-Sham potentials for passivant.

In the previous section, the construction of AEPs for the bulk systems have been introduced. Within the framework of the AEP methods, we present a procedure to extract the AEPs for surface passivants. In contrast with bulk's AEPs generation, the imaginary components of the passivant's AEPs should be retained in order to model surface dipoles which generate a band offset to vacuum. As the influence of surface on the electronic and optical properties of nanostructures is significantly important, an accurate quantitative treatment of surface effect is desirable. Our AEPs for passivant, which can be simply derived from DFT calculation without empirical parameters, have been shown to work as well as DFT but require a much less computational cost. Once AEPs for passivant of a material are created, they can be used in all other types of structure made from that material, this demonstrates a high level of transferability of AEPs. For the construction of AEPs of passivants we consider a nanostructure of a binary cation-anion system with two types of passivant denoted by H_1 which is attached to the cation and H_2 which is attached to the anion. The potential in equation (2.8) becomes

$$\begin{aligned}\Omega_{\mathrm{c}}V_{\mathrm{loc,KS}}(\mathbf{G}) =&\left(\sum_{n}^{N_{\mathrm{cat}}} e^{-i\mathbf{G}.\boldsymbol{\tau}^{cat,n}}\right)v_{\mathrm{cat}}(\mathbf{G}) + \left(\sum_{n}^{N_{\mathrm{ani}}} e^{-i\mathbf{G}.\boldsymbol{\tau}^{ani,n}}\right)v_{\mathrm{ani}}(\mathbf{G}) \\ &+ \left(\sum_{n}^{N_{\mathrm{H}_1}} e^{-i\mathbf{G}.\boldsymbol{\tau}^{H_1,n}}\right)v_{\mathrm{H}_1}(\mathbf{G}) + \left(\sum_{n}^{N_{\mathrm{H}_2}} e^{-i\mathbf{G}.\boldsymbol{\tau}^{H_2,n}}\right)v_{\mathrm{H}_2}(\mathbf{G}) \\ =&S_{\mathrm{cat}}v_{\mathrm{cat}}(\mathbf{G}) + S_{\mathrm{ani}}v_{\mathrm{ani}}(\mathbf{G}) + S_{\mathrm{H}_1}v_{\mathrm{H}_1}(\mathbf{G}) + S_{\mathrm{H}_2}v_{\mathrm{H}_2}(\mathbf{G})\end{aligned} \tag{2.19}$$

where $S_{\mathrm{cat,ani,H_1,H_2}}$ are the structure factors of the cations, the anions, the passivants H_1, and the passivants H_2 respectively. AEPs for passivants can be directly calculated from equation (2.19)

$$S_{\mathrm{H}_1}v_{\mathrm{H}_1}(\mathbf{G}) + S_{\mathrm{H}_2}v_{\mathrm{H}_2}(\mathbf{G}) = \Omega_{\mathrm{c}}V_{\mathrm{loc,KS}}(\mathbf{G}) - (S_{\mathrm{cat}}v_{\mathrm{cat}}(\mathbf{G}) + S_{\mathrm{ani}}v_{\mathrm{ani}}(\mathbf{G})). \tag{2.20}$$

In this equation, everything except for $S_{\mathrm{H}_1}v_{\mathrm{H}_1}(\mathbf{G})$ and $S_{\mathrm{H}_2}v_{\mathrm{H}_2}(\mathbf{G})$ is known. To extract $S_{\mathrm{H}_1}v_{\mathrm{H}_1}(\mathbf{G})$ and $S_{\mathrm{H}_2}v_{\mathrm{H}_2}(\mathbf{G})$ we need to introduce the second equation of the second system and denote them with A and B

$$S^{\mathrm{A}}_{\mathrm{H}_1} v_{\mathrm{H}_1}(\mathbf{G}) + S^{\mathrm{A}}_{\mathrm{H}_2} v_{\mathrm{H}_2}(\mathbf{G}) = \Omega_{\mathrm{c}} V^{\mathrm{A}}_{\mathrm{loc,KS}}(\mathbf{G}) - (S^{\mathrm{A}}_{\mathrm{cat}} v_{\mathrm{cat}}(\mathbf{G}) + S^{\mathrm{A}}_{\mathrm{ani}} v_{\mathrm{ani}}(\mathbf{G})), \tag{2.21}$$

$$S^{\mathrm{B}}_{\mathrm{H}_1} v_{\mathrm{H}_1}(\mathbf{G}) + S^{\mathrm{B}}_{\mathrm{H}_2} v_{\mathrm{H}_2}(\mathbf{G}) = \Omega_{\mathrm{c}} V^{\mathrm{B}}_{\mathrm{loc,KS}}(\mathbf{G}) - (S^{\mathrm{B}}_{\mathrm{cat}} v_{\mathrm{cat}}(\mathbf{G}) + S^{\mathrm{B}}_{\mathrm{ani}} v_{\mathrm{ani}}(\mathbf{G})). \tag{2.22}$$

By adding and subtracting two equations (2.21) and (2.22) we obtain a system of equations

$$\mathbf{A}x = \mathbf{B} \tag{2.23}$$

with

$$\mathbf{A} = \begin{pmatrix} S^{\mathrm{A}}_{\mathrm{H}_1} + S^{\mathrm{B}}_{\mathrm{H}_1} & S^{\mathrm{A}}_{\mathrm{H}_2} + S^{\mathrm{B}}_{\mathrm{H}_2} \\ S^{\mathrm{A}}_{\mathrm{H}_1} - S^{\mathrm{B}}_{\mathrm{H}_1} & S^{\mathrm{A}}_{\mathrm{H}_2} + S^{\mathrm{B}}_{\mathrm{H}_2} \end{pmatrix} \tag{2.24}$$

$$x = \begin{pmatrix} v_{\mathrm{H}_1}(\mathbf{G}) \\ v_{\mathrm{H}_2}(\mathbf{G}) \end{pmatrix}, \tag{2.25}$$

$$\mathbf{B} = \begin{pmatrix} \Omega_{\mathrm{c}} \left(V^{\mathrm{A}}_{\mathrm{loc,KS}}(\mathbf{G}) + V^{\mathrm{B}}_{\mathrm{loc,KS}}(\mathbf{G}) \right) - \left(S^{\mathrm{A}}_{\mathrm{cat}} + S^{\mathrm{B}}_{\mathrm{cat}} \right) v_{\mathrm{cat}}(\mathbf{G}) - \left(S^{\mathrm{A}}_{\mathrm{ani}} + S^{\mathrm{B}}_{\mathrm{ani}} \right) v_{\mathrm{ani}}(\mathbf{G}) \\ \Omega_{\mathrm{c}} \left(V^{\mathrm{A}}_{\mathrm{loc,KS}}(\mathbf{G}) - V^{\mathrm{B}}_{\mathrm{loc,KS}}(\mathbf{G}) \right) - \left(S^{\mathrm{A}}_{\mathrm{cat}} - S^{\mathrm{B}}_{\mathrm{cat}} \right) v_{\mathrm{cat}}(\mathbf{G}) - \left(S^{\mathrm{A}}_{\mathrm{ani}} - S^{\mathrm{B}}_{\mathrm{ani}} \right) v_{\mathrm{ani}}(\mathbf{G}) \end{pmatrix}. \tag{2.26}$$

In our model, we terminate the nanostructures by hydrogen for group IV semiconductors and by pseudo hydrogens, which have atomic numbers differing from 1, for groups II-VI and III-V semiconductors. In II-VI compounds each cation has 2 valence electrons and each anion has 6 valence electrons forming 4 bonds with 4 neighbor atoms. Each bond is contributed by 1/2 electrons from cation and 3/2 electrons from anion. At the surface of NCs dangling bonds of cation needed to be filled by pseudo hydrogens which must have the atomic number of 3/2 and dangling bonds of anion needed to be filled by pseudo hydrogens which must have the atomic number of 1/2. Analogously, in III-V compound, the nanostructure's surface is terminated by pseudo hydrogens which have the atomic number of 5/4 and 3/4 attached to cation and anion, respectively (figure 2.2).

The A and B systems used to construct the AEPs for passivant are two [111] slabs differ only in the length of the slabs used but the sizes of the supper cells are the same. Slab A includes 12 atoms while slab B includes 16 atoms, both slabs A and B have 4 passivants. The slab structure was chosen because they satisfy three criteria: (i) They are long enough in at least one direction in order to produce a dense grid of

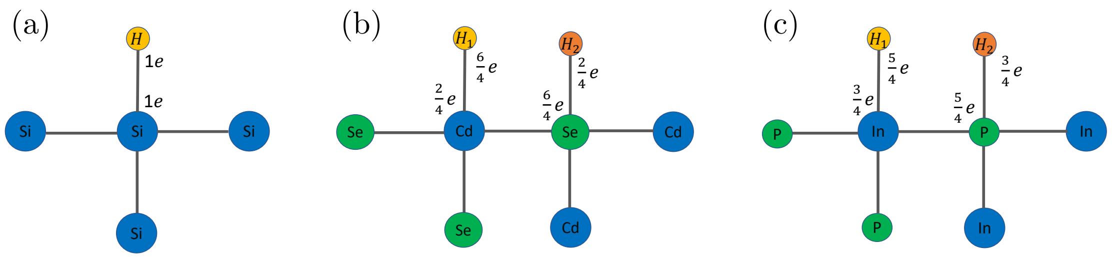

Figure 2.2: Real and pseudo hydrogen passivants of (a) Si, (b) CdSe, and (c) InP

G-point along the extended supercell direction, (ii) they are not too large to be dealt by the standard DFT, and (iii) the physical situation in slab is representative of the situation encountered in the real calculation. The illustration of two slabs A and B are in figure 2.3. We only use the grid points along the extended direction of the supercell, which is the z direction in our case, of $V^{\mathrm{A,B}}_{\mathrm{loc,KS}}(\mathbf{G})$ obtained from the self-consistent DFT calculations.

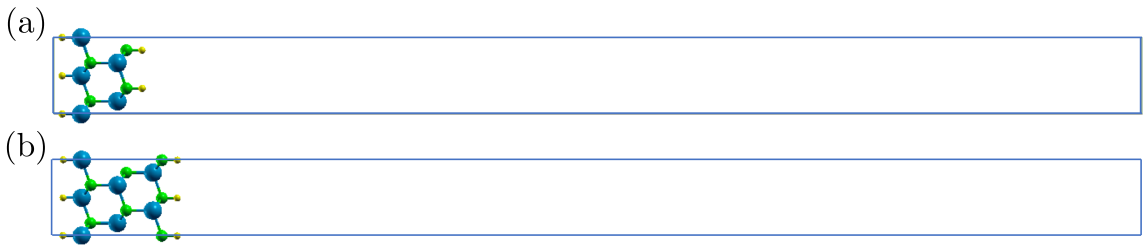

Figure 2.3: Slab A (a) and slab B (b) used to construct the AEPs for passivant H_1 and H_2. Blue color represents cation atoms, green color represents anion atoms and yellow color represents passivants. In the case of VI group semiconductor, cation and anion are the same and H_1, H_2 are the same.

$$V^{\mathrm{A,B}}_{\mathrm{loc,KS}}(\mathbf{G}) \equiv V^{\mathrm{A,B}}_{\mathrm{loc,KS}}(0,0,G). \tag{2.27}$$

Solving equation (2.23) we obtain $v_{H_{1,2}}(\mathbf{G})$, where G is the length of the vector $\mathbf{G}$. For both real and imaginary components of $v_{H_{1,2}}(\mathbf{G})$, we use the spherical approximation: Re $v_{H_{1,2}}(\mathbf{G})$ = Re $v_{H_{1,2}}(|G|)$ and Im $v_{H_{1,2}}(\mathbf{G})$ = Im $v_{H_{1,2}}(|G|)$. The real and the imaginary parts of $v_{H_{1,2}}(\mathbf{G})$ are illustrated in figure 2.4. In the case of VI group semiconductor H_1 and H_2 are the same, therefore the real components of $v_{\mathrm{H}_1}(\mathbf{G})$ and $v_{\mathrm{H}_2}(\mathbf{G})$ are identical while their imaginary components have the same magnitudes but opposite signs. We store our passivant AEP with the imaginary sign corresponding to the passivant orientation [111] in the slab geometry (pointing upwards). The contribution of passivant in the effective potential extracted from DFT calculation in reciprocal

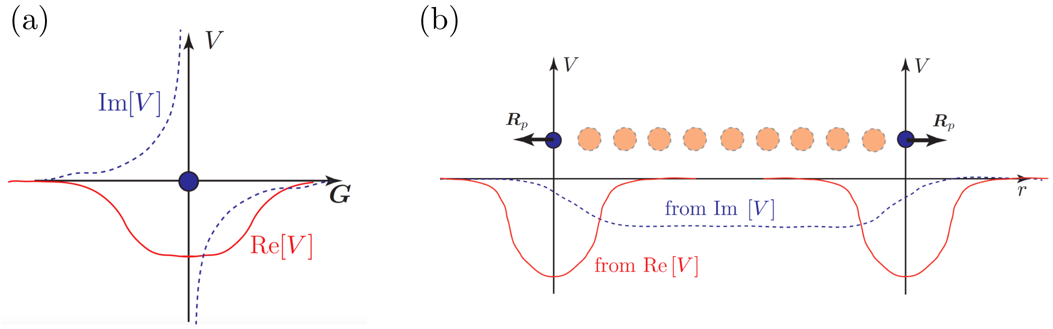

Figure 2.4: (a) The real and imaginary components of the hydrogen AEP in reciprocal space, the real part is even while the imaginary part is odd. (b) AEPs in real space of passivants with vectors pointing in opposite directions, corresponding to the situation in our slabs geometries.

space, $V_{\mathrm{H}}(\mathbf{G})$, can be written as

$$\begin{aligned} V_{\mathrm{H}}(\mathbf{G}) &= \frac{1}{\Omega_{\mathrm{c}}}\sum_{n}^{N_{\mathrm{H}}} e^{-i\mathbf{G}.\boldsymbol{\tau}^{H,n}} v_{\mathrm{H}}(\mathbf{G}) \\ &\approx \frac{1}{\Omega_{\mathrm{c}}}\sum_{n}^{N_{\mathrm{H}}} e^{-i\mathbf{G}.\boldsymbol{\tau}^{H,n}} \left(\mathrm{Re}\left(v_{\mathrm{H}}(\mathbf{G})\right) + i\frac{\mathbf{G}.\mathbf{R}_{\mathrm{p}}}{|\mathbf{G}||\mathbf{R}_{\mathrm{p}}|}\mathrm{Im}\left(v_{\mathrm{H}}(\mathbf{G})\right)\right) \end{aligned} \tag{2.28}$$

where $\mathbf{R}_{\mathrm{p}}$ is the real-space normal vector in Cartesian coordinates, denoting the direction of the antisymmetric component introduced by the imaginary part. Equation (2.28) represents a generalization of the one dimensional case where $\mathbf{G}$ and $\mathbf{R}_{\mathrm{p}}$ are parallel or antiparallel to a situation where they have arbitrary orientation. The only known solutions are for the limiting cases of parallel/antiparallel vectors (prefactor to imaginary part $1/-1$) or perpendicular (prefactor to imaginary part 0 as we want spherical (real) potentials in the plane). We use a cosine function (dot product) connecting both cases as the simplest possible assumption. As will be demonstrated further, it is advantageous to apply a weight factor ω to the imaginary part in certain circumstances:

$$V_{\mathrm{H}}(\mathbf{G}) = \frac{1}{\Omega_{\mathrm{c}}}\sum_{n}^{N_{\mathrm{H}}} e^{-i\mathbf{G}.\boldsymbol{\tau}^{H,n}} \left(\mathrm{Re}(v_{\mathrm{H}}(\mathbf{G})) + i\frac{\mathbf{G}.\mathbf{R}_{\mathrm{p}}}{|\mathbf{G}||\mathbf{R}_{\mathrm{p}}|}\omega\mathrm{Im}(v_{\mathrm{H}}(\mathbf{G}))\right) \tag{2.29}$$

2.2.2 AEPs for InP and CdSe passivants

To generate AEPs for pseudo hydrogens of, for example, InP we use slab A and slab B oriented in [111] direction and the bonds to passivant atoms in this direction as well.

DFT calculations for slab A and slab B were done using the code ABINIT [45, 46], we used elongated supercells of around 10.2 nm length in order to obtain a dense grid of G points. The k-point mesh is 10 × 6 × 1 and the energy cutoff is 35 Hartree. We use Troullier-Martins norm-conserving pseudopotentials for DFT calculations and for the nonlocal parts of the pseudopotentials in the AEP method. Pseudo hydrogens were relaxed using ABINIT, other atoms (In and P) were kept as they are in the bulk system. AEPs for passivants of InP are shown in figure 2.5a,b. The same procedure was applied to generate AEPs for CdSe passivants using zinc-blende (ZB) structure slabs. The supercell was chosen to be ten-time longer than the lattice parameter of CdSe Zinc-blende (ZB) structures (about 10.6 nm). It will be later shown that the AEPs of CdSe passivants produced from the Zinc-blende structure slabs can be transferred to other structures. AEPs for CdSe passivants are shown in 2.6c,d.

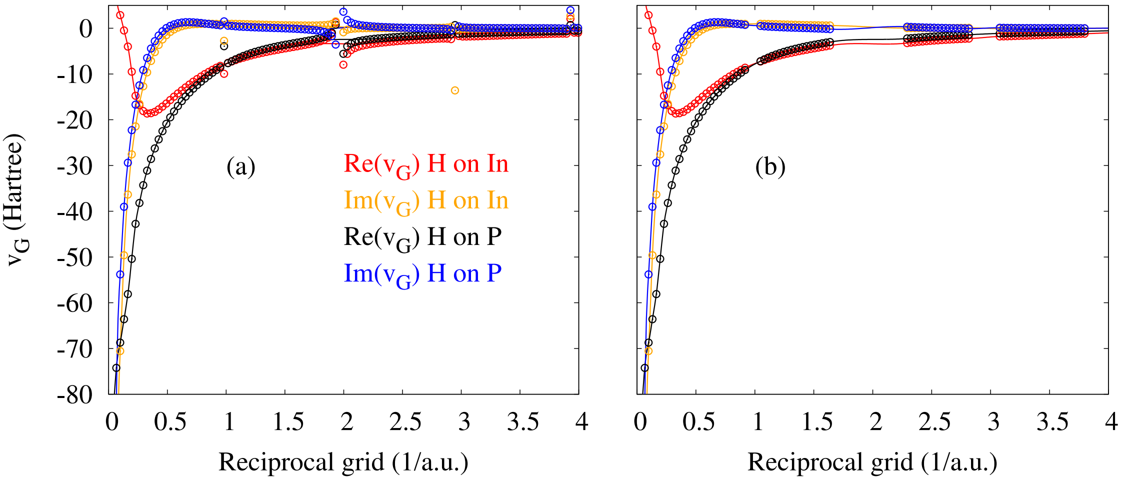

Figure 2.5: AEPs for InP passivants as functions of $|G|$ with (a) raw data points and (b) bad points removed. Red circles represent the real parts, orange circles represent the imaginary parts of AEPs for passivants of In. Black circles represent the real parts, blue circles represent the imaginary parts of AEPs for passivants of P. Lines show the final AEPs.

In the region of $|G| = n2\pi\sqrt(3)/a_0$ (for InP $|G| = n * 0.977\ 1/a.u.$, for CdSe $|G| = n * 0.941\ 1/a.u.$), where n is an integer and a_0 is the bulk lattice constant, the data point extraction suffers from the error which is intrinsically carried over from our bulk AEPs, i.e., the AEPs for InP and CdSe in this case. Since the goal for our passivant AEP is not to correct the deviations existing within the bulk AEPs, we omit the data points in the vicinity of these $|G|$ values. By using these data points, one may indeed obtain better agreement than by ignoring them for the specific structure, but

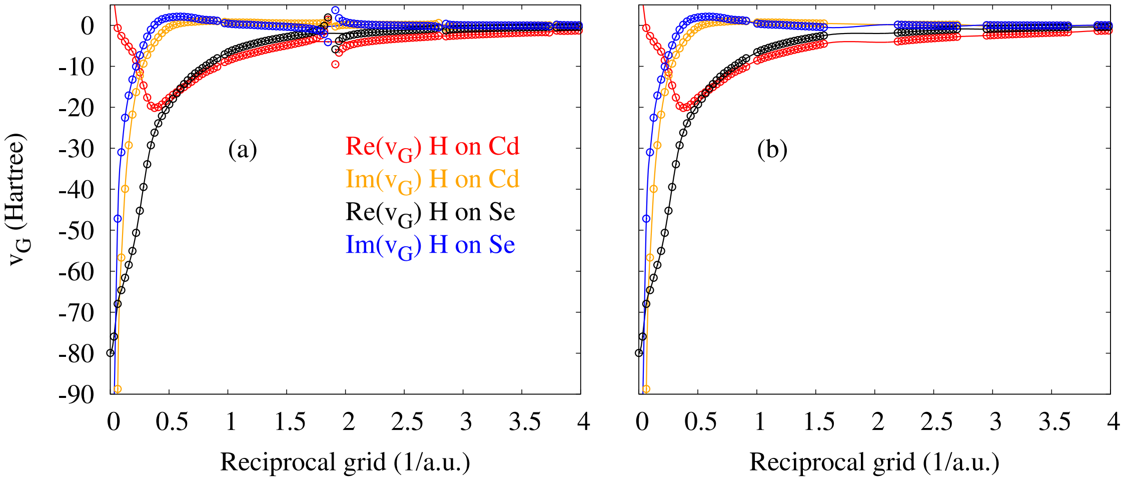

Figure 2.6: AEPs for CdSe passivants as functions of $|G|$ with (a) raw data points and (b) bad points removed. Red circles represent the real parts, orange circles represent the imaginary parts of AEPs for passivants of Cd. Black circles represent the real parts, blue circles represent the imaginary parts of AEPs for passivants of Se. Lines show the final AEPs.

the transferability to structures with different dimensionality would be less accurate. The passivant effective potential shows a very steep imaginary part for small $|G|$ values and the rather smooth real part, comparable to bulk AEPs.

2.2.3 Assessment of the quality of the AEP for different surfaces

The slab [111] structure (figure 2.2), which represents the passivation of a (111) surface, is the geometry used to generate the AEP. As a first step, we compare the DFT results with the AEP results for the same structure. In figure 2.7a, we plot the eigenvalues of the CdSe slab A calculated via DFT (red), AEP only taking the real part into account (black) and the full AEP with real and imaginary component (blue). The band gap is located around state index 38. It is obvious that the imaginary part of the potential improves the quality of the states above band gap significantly. This is a direct consequence of the introduced band-offset discussed previously. Next, we want to challenge the transferability of the derived AEPs by comparing different slab orientations. In figure 2.7b,c, we plot the eigenvalues of different slabs, the error bars show eigenvalue differences for states around the band gap, aligned at the valence band maximum (VBM) level. Our errors are within a range of 20 meV. It is worth noting that the error of the AEP for bulk band gap of CdSe is 10 meV [21]. So all the conduction band states suffer from the 11 meV error coming from the bulk CdSe AEPs and the errors introduced by the passivant AEPs. Both errors seem to be of similar magnitude, which substantiates the good quality of our approach.

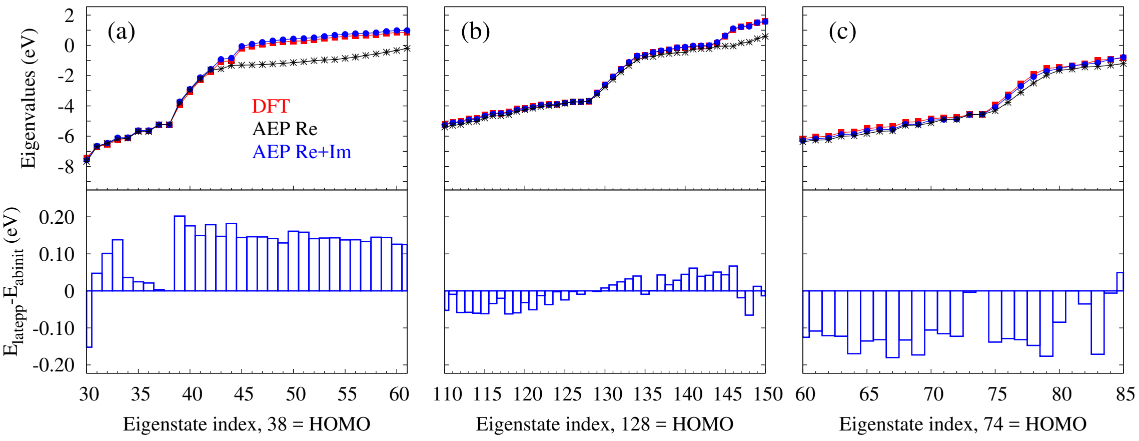

Figure 2.7: Comparison between AEPs and DFT results for (111), (110), and (100) surfaces. Upper panels are eigenvalues aligned at VBM obtained using DFT (red squares), AEPs using only the real component (black stars), and AEPs including the imaginary and the real components of the pseudopotentials (blue circles). The lower panels show the differences between the AEP and the DFT eigenvalues as bar charts.

2.2.4 Results for Si, InP and CdSe nanowires

The areas of applications of our AEPs are nanostructures and we therefore first assess the quality of our results for nanowires (NWs). The structural information is given in table 2.1 and a graphical representation of the atomic positions are given in figure 2.8a for an InP nanowire with 1.6 nm diameter. Each nanowire is constructed along the [110] direction for Si and InP, and along the [0001] for Wurtzite CdSe nanowire. The surfaces of the nanowires are terminated in such a way that each surface atom has only one or two passivants.

The real-space potential is plotted in figure 2.8b. The comparison between DFT (red) and AEP (blue) shows that the AEP reproduces the potential very well in general but significantly overestimates the band offset (the blue line in the vacuum region is significantly above the red line). This effect is related to the density of hydrogen atoms on the surface.

NWs diameter (nm)	Si				InP			CdSe
	1.3	2.1	3.0	4.5	1.3	1.7	1.6	1.4
N_{QW}	37	97	185	437	(16,21)	(32,25)	(26,26)	(24,24)
$N_{\mathrm{H,H}}$	28	44	60	92	(4,24)	(32,4)	(16,16)	(18,18)
ρ(H) (1/nm^2)	12.47	12.37	12.33	11.99	11.50	11.14	10.76	11.69
$E_{\mathrm{gap(DFT)}}$ (eV)	2.147	1.401	1.156	0.878	1.771	1.095	1.207	1.475
$E_{\mathrm{gap(AEP)}}$ (eV)	2.165	1.472	1.233	0.965	1.911	1.082	1.273	1.628

Table 2.1: Structural parameters and band gaps of different nanowires. The Si and InP NWs are in zinc-blende crystal structure while the CdSe NW is in wurtzite structure. NW represents the number of atoms in the NWs. For InP [CdSe], the atom numbers are given as (number of In atoms, number of P atoms) [(number of Cd atoms, number of Se atoms)]. For InP, the number of passivants is given as (In-passivant, P-passivant) [for CdSe (Cd-passivant, Se-passivant)]. The hydrogen densities on the surfaces are given as $\rho(H)$.

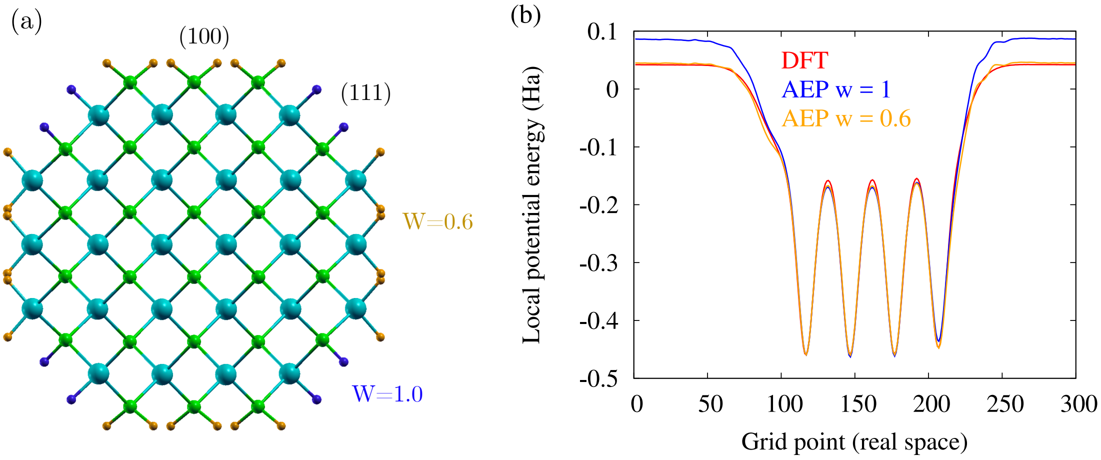

Figure 2.8: (a) The geometry of the InP nanowire with a diameter of 1.6 nm. The hydrogens carrying a weight parameter (ω in Eq. (2.29)) of $\omega = 0.6$ are shown as orange spheres, while the unweighted hydrogens $\omega = 1$ are shown in blue. (b) Corresponding local potential.

As seen from table 2.1 the hydrogen atom surface density is around 11 H-atoms/nm^2 in InP NWs, while it is 6.6 H-atoms/nm^2 in the [111] InP slab used in the AEP construction. Hence, we look for a way to systematically reduce the generated offset based on a density argument. A closer look at the NW geometry, shown in figure 2.8a, reveals that it is composed of facets belonging to 100 and 111 planes. In the high-density 100 surfaces, two hydrogen atoms are connected to one host atom. We use this characteristic to apply weights: if a surface host atom is passivated by two hydrogen atoms, then the density is high and we apply a weight in equation (2.29) of 0.6, which corresponds to the ratio of the densities between slab [111] and [100]. In figure 2.8a, we marked the hydrogen atoms carrying a weight as orange spheres and see that they are mostly localized on the 100 planes. The results for the potential in the vacuum region, i.e., the offset, is significantly improved by the use of weight, as can be seen (orange curve) in figure 2.8b.

The main benefit of introducing a weight to the imaginary part is to correct the offset, as just shown, which has direct repercussions on the eigenvalues of excited states close to the vacuum. In figure 2.9, which shows the eigenvalues in a large energy range, starting at the lowest energy eigenstate at −8 eV up to 4 eV above the gap. The calculations without weight (blue data points) are in good agreement with the DFT results (red data points) until an energy value of around 2 eV above the CBM. At higher energies, deviations become significant, which are well corrected by the weighted potentials (orange data points).

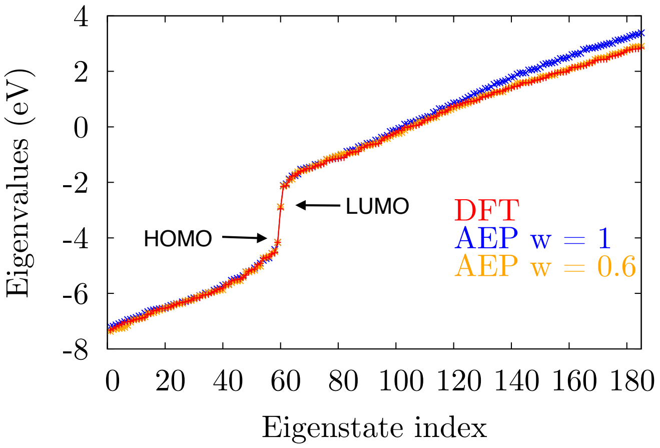

Figure 2.9: Eigenvalues of the $D = 1.6$ nm InP QW (see table 2.1 for structural details). The introduction of the weight factors (orange symbols) is shown to improve the quality of the previous results (blue symbols) for states excited more than 2 eV above the band gap. Red and orange symbols overlap nearly in the entire region.

Finally, we perform a quantitative comparison of the eigenvalues obtained for nanowires of different materials in figure 2.10. In the upper panels, we show a large energy range in the vicinity of the band gap. For both InP, and CdSe, the AEP results (blue crosses) are in very good agreement with the DFT results (red squares). The errors between the DFT and the AEP results are given as bar charts in the lower parts of the figures, showing that all errors are below 150 meV, which is more than satisfactory. The introduction of the weight factor does not change the results significantly in this energy range, as is shown by the orange error bars in the lower panels of figure 2.10.

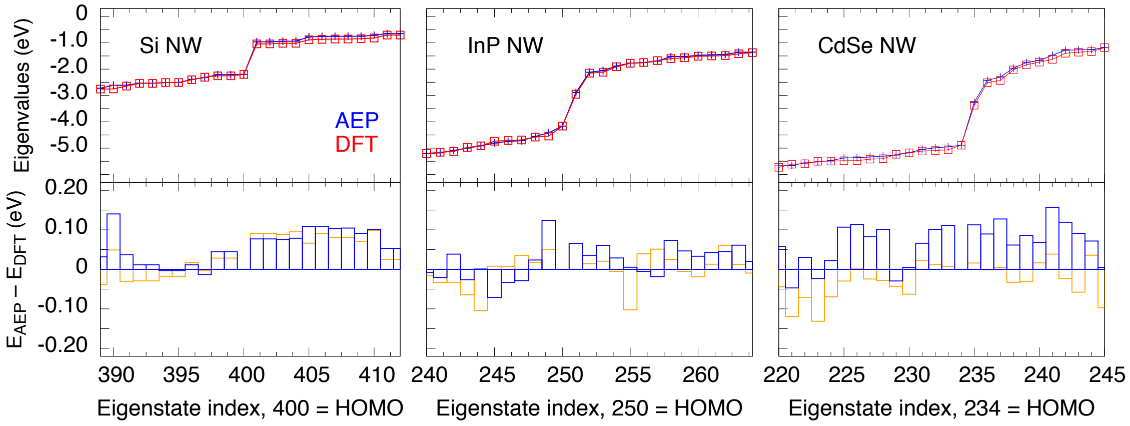

Figure 2.10: Top panels: Eigenvalues of Si, InP, and CdSe nanowires in the proximity of the band gap. Lower panels: Bar charts showing the differences between DFT results and the AEP result including the weight strategy (orange) and the AEP result without weight (blue).

2.2.5 Results for InP and CdSe QDs

The final comparison for QDs is also the most challenging in terms of transferability as the passivant atoms point virtually in all directions. The structural information as well as the numerical results for the band gaps are given in table 2.2 for different InP and CdSe QDs. The average hydrogen densities are similar to the values we obtained for the nanowires (table 2.1). The band gaps are in good agreement with the DFT results for all QDs considered.

QDs diameter (nm)	InP		CdSe	
	1.6	2.4	2.1	2.4
N_{QD}	(43,44)	(141,152)	(81,86)	(128,138)
N_{H}	(36,40)	(64,108)	(46,66)	(60,96)
$\rho(\mathrm{H})$ $(1/\mathrm{nm}^2)$	9.45	9.51	8.9	8.6
$E_{\mathrm{gap(DFT)}}$ (eV)	2.472	1.728	1.712	1.487
$E_{\mathrm{gap(AEP)}}$ (eV)	2.513	1.723	1.764	1.530

Table 2.2: Structural parameters and band gaps of different InP and CdSe QDs. N_{QD} gives the number of In and P (Cd and Se) atoms in the QD. N_{H} gives the number of In-passivants and P-passivant (Cd-passivants and Se-passivant). The hydrogen densities on the surfaces are given as $\rho(\mathrm{H})$.

In figure 2.11, we show the eigenvalues in a large range of energy as well as the error bars in the usual way. The quality of the results is excellent with errors below 150 meV. The quality of the wave function can be judged by projecting them onto the DFT wave functions: $\langle \psi^{\mathrm{AEP}} | \psi^{\mathrm{DFT}} \rangle$ We obtain values very close to 1.0. In figure 2.11c, we show selected wave function as one-dimensional plots across the center of the QD as an illustration. Wave functions of degenerate eigenstates are summed and their degeneracy is denoted in brackets. The values close to one are the numerical values of the projection onto the DFT wave functions. The DFT results (red) and the AEP results with weight (orange) show very good agreement.

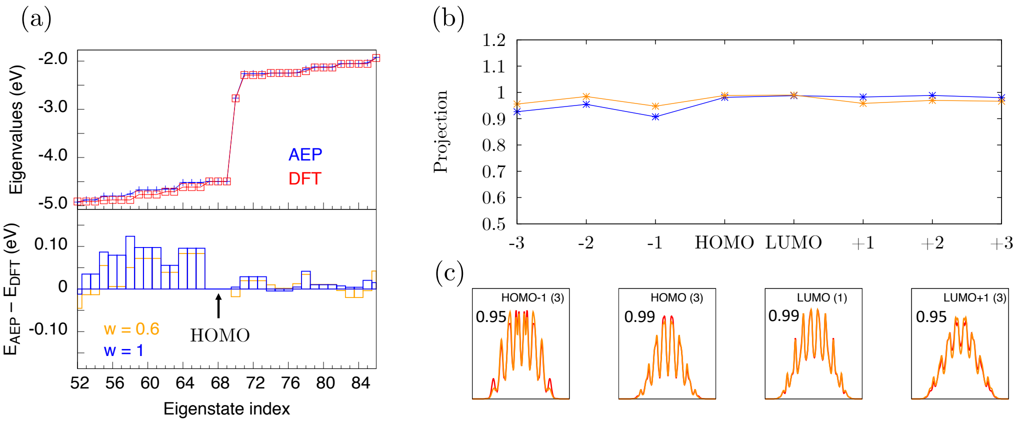

Figure 2.11: DFT and AEP results for 2.4 nm diameter InP QD. (a) The eigenvalues and the eigenvalue differences are given in the upper panel, (b) the projection is calculated as $\langle \psi^{\mathrm{AEP}} | \psi^{\mathrm{DFT}} \rangle$ and describes the quality of the wave functions, and (c) selected wave functions are given explicitly in one dimension across the QD.

2.3 Generation of artificially relaxed QDs

In principle, a QD is generated from a bulk system, as illustrated in figure 2.12. A QD with a given radius is cut out from the bulk system and surface atoms are passivated by hydrogen or pseudo hydrogen. Since the surface atoms which have three passivants are not stable, we avoid this situation in our generation procedure by removing all the surface atoms with three dangling bonds from the QD. By doing so, the bond length in the QD is the bond length of the bulk system. The distances between passivants and the host atoms are defined as the optimal distances in relaxed slabs obtained from DFT.

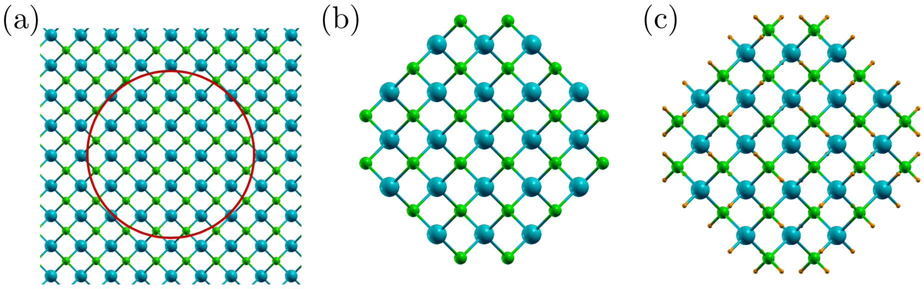

Figure 2.12: (a) The bulk system, (b) a QD without passivants cut from the bulk system, (c) a complete QD with passivants.

We perform a DFT calculation to obtain the forces on each atoms of the QD. Figure 2.13 represents the forces acting on the atoms of InP QDs with different diameters. The forces obtained for a 1.6 nm diameter QD have a maximum value of 7×10^{-3} Ha/Bohr, while in the 2.4 nm diameter QD they have a maximum value of 2×10^{-2} Ha/Bohr which is surprisingly high as it is expected that the larger QD, the smaller maximum force on atoms. Figure 2.13b shows that the atoms with unexpected forces are passivants of In. By looking at the structure, as shown in figure 2.14a, we see that atoms with large forces are passivants of In atoms which are very close to each other (1.26 Å). and that In atoms themself also get more force compared to other In atoms. This situation occurs only in big QDs and for In atoms and their passivants because of the long optimal distance between In and its passivant (1.78 Å). The optimal distance between P and its passivant is 1.6 Å that is small and does not make passivants of P

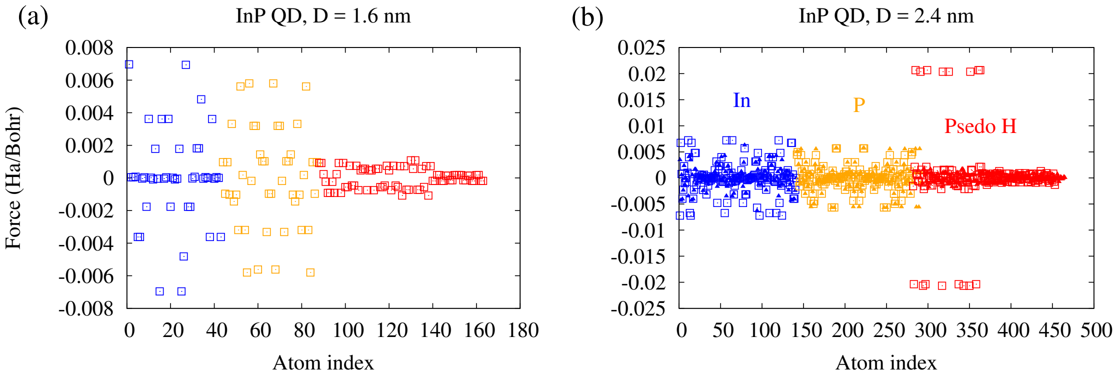

Figure 2.13: Forces acting on the atoms of (a) a 1.6 diameter InP QD and (b) a 2.4 diameter InP QD. The open squares show the forces before refining structure and solid triangles show the forces after refining structure. Blue points represent In atoms, orange points represent P atoms, and red points represent passivants.

atoms at the surface too close to each other. This problem can be resolved by replacing these clusters of passivants of an In atom by a P atom, as shown in figure 2.14b. This simple technique significantly reduces forces acting on atoms. The forces before and after refining the structure are shown in figure 2.13b.

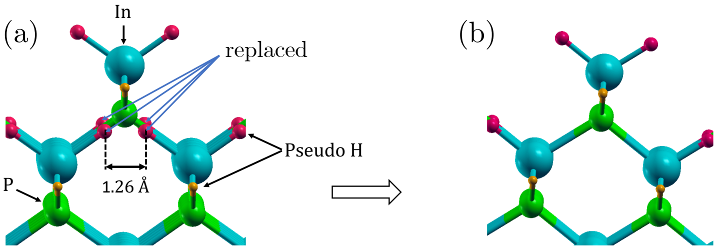

Figure 2.14: QD (a) before and (b) after refinement by replacing clusters of passivants of In atoms by P atoms. Blue and red colour represent In atoms and their passivants respectively. Green and orange colour represent P atoms and their passivants, respectively.

In summary, the procedure of generating an artificially relaxed QD includes five steps: (i) Make a bulk system that should be big enough to contain the QD. (ii) Cut out the QD from the bulk system, the remainder will be later replaced by passivants. (iii) Move anion atoms in the remainder part which coordinate to more than one cation atom in the QD part to the QD part. (iv) Find and remove from the QD atoms at the surface which have three dangling bonds. (v) Add passivants for surface atoms.

To inspect the quality of the non-relaxed QD, we compare DFT calculations of relaxed and non-relaxed QDs. InP QDs are relaxed using the ABINIT code and the QDs are considered to be relaxed when their total energies converge with respect to the maximum force. Table 2.3 shows an excellent agreement in QD gaps between relaxed and non-relaxed InP QDs.

Diameter (nm)	1.6	2.4	3.2
$F_{\max}^{\text{non-relaxed}}$, Ha/Bohr	7.00×10^{-3}	6.28×10^{-3}	4.48×10^{-3}
$F_{\max}^{\text{relaxed}}$, Ha/Bohr	6.40×10^{-5}	4.10×10^{-4}	4.83×10^{-4}
$Gap^{\text{non-relaxed}}$, eV	2.45	1.73	1.49
Gap^{relaxed}, eV	2.51	1.74	1.51

Table 2.3: Comparison between non-relaxed and relaxed InP QDs. The maximum force act on atoms of non-relaxed QDs reduces with the QDs size leading to a better agreement in QD gaps.

It is well known that the interior of the colloidal QD is almost bulk-like while the surface is slightly compressed. The bigger QD the less important surface effect and, therefore, the better our artificially relaxed QD. It is clearly shown in table 2.3, the difference between QD gaps is reduced when the size of QD increases. Figure 2.15 shows DFT eigenvalues and eigenvalue differences for states around the band gap, aligned at the highest occupied molecular orbital (HOMO) level of relaxed and non-relaxed InP QD with a diameter of 1.6 nm.

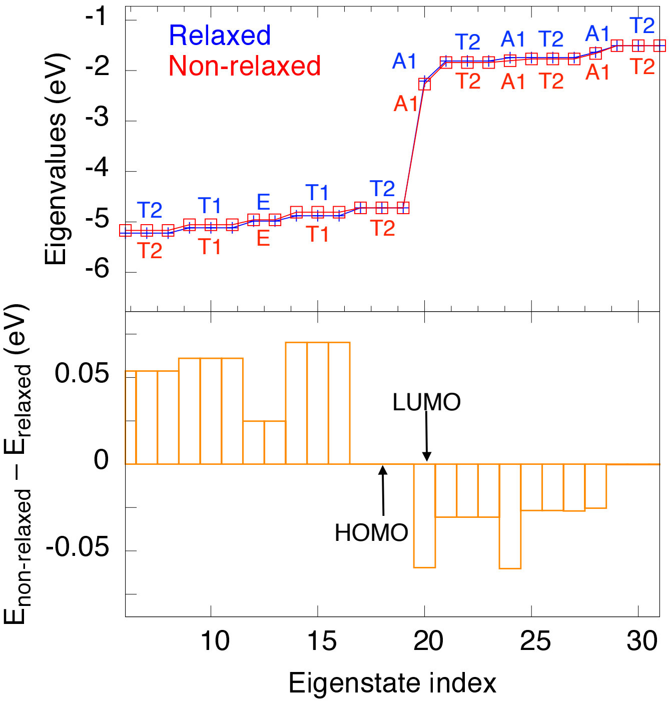

Figure 2.15: Comparison between the relaxed and non-relaxed 1.6 nm diameter InP QD. The upper panel shows the eigenvalues calculated without SO aligned at the HOMO. The lower panel shows the differences between the eigenvalues of the relaxed and non-relaxed QD as bar charts. Non-degenerate wavefunctions are represented by A_1 or A_2 representations, two-fold degenerate wavefunctions are represented by E representation, and three-fold degenerate wavefunctions are represented by T_1 or T_2 representations.

The errors are within a range of 60 meV which is about 2% of band gap value and can be negligible. We also develop a code to analyse the symmetry of wavefunctions. A zinc-blende spherical QD has T_d symmetry, hence, its wavefunction can be represented by A_1, A_2 representation if the wavefunction is non-degenerate, the wavefunction is represented by E representation if it is two-fold degenerate; and if the wavefunction is three-fold degenerate it is represented by either T_1 or T_2 representation. The results show that relaxed and non-relaxed QD give identical symmetry of wavefunction.

It should be noted that up to this point, all calculations we have shown are without the effect of SO coupling. In the presence of SO coupling, all states are doubly degenerate by Kramers degeneracy. A double group is invoked to represent the symmetry of the system and its wavefunctions will be described by more complex representations which are combinations of orbital and spinor components. The SO coupling is added from next chapter.

Chapter 3

Empirical correction

The AEP [21, 61, 116] method allows us to study nanocrystals with experimental sizes with LDA-quality eigenfunctions and eigenvalues. The AEPs are directly obtained from density functional theory [21] using the local density approximation [75] for the exchange-correlation functional. As a consequence, the typical errors from LDA, such as underestimated band gaps and effective masses, are inherited by the AEP. In this work, we apply a simple correction scheme based on a small modification of the non-local part of norm-conserving pseudopotentials δV_{NL}, that enables us to obtain accurate quasiparticle band gaps and effective masses.

3.1 The functional form of the correction

Following the notation of Ref. [116] we have

$$V_{\mathrm{NL}} = \sum_{l,m} |l,m\rangle \, \delta V_l(r) \, \langle l,m| \,, \tag{3.1}$$

and the correction is applied as:

$$\delta V_l^{\mathrm{modified}}(r) = \delta V_l(r) + \beta_l (1 + \cos \frac{\pi r}{r_{\mathrm{c}}}) \quad , \tag{3.2}$$

where the β_l parameter is individually adjusted for every material and angular momentum to fit the bulk band gap to the experimental value.

As the norm-conserving pseudopotential has some desirable properties such as (i) the pseudo and the real potentials agree beyond a chosen "core-radius" r_{c}; (ii) the integrals from 0 to r of the real and the pseudo-densities agree for $r > r_{\mathrm{c}}$ for each valence state; (iii) the logarithmic derivatives of real and pseudo wave functions and their fist energy derivatives agree for $r > r_\mathrm{c}$ [50]. We want to preserve these properties of pseudopotential as much as possible. That is why δV_l is only modified within the radius r_c and kept unchanged for larger r values.

In semiconductors, the HOMO is mostly contributed by the anion p component while the lowest unoccupied molecular orbital (LUMO) is dominant by the cation s component. Therefore we need to apply a modification with a negative (positive) β parameter to the p (s) component of pseudopotential of the anion (cation) to open the band-gap. β parameter of the cation is varied from 0 to 0.2, and β parameter of the anion is varied from -0.2 to 0 with the step of 0.01 to find out a couple of parameters which give us the correct band-gaps, and effective masses.

3.2 Result for InP

Figure 3.1 shows the contour plot of the differences between calculated values and the experimentally measured values of the band-gap and the effective mass of electron. These two contour lines are almost parallel to each other indicating that it is impossible to correct band-gap and effective mass of electron with the same values of β_l. As shown in this figure, there are many pairs of $\beta_{\mathrm{In-s}}$ and $\beta_{\mathrm{P-p}}$ that can correct band-gap or effective mass of electron. In our calculation, we choose the pair of β_l that give the best value for the ΓL, ΓX gaps, and the spin-orbit splitting Δ_{SO} besides band-gap and effective mass.

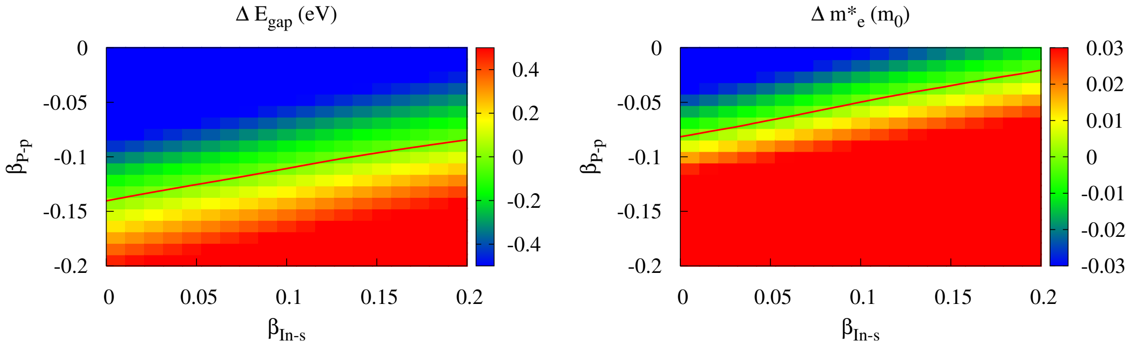

Figure 3.1: Contour plot the differences between calculated values and the experimental values of (a) band-gap (in eV) and (b) the effective mass of electron (in m_0).

The effective mass of electron (m_e^*), band-gaps, ΓL, ΓX gaps, and the spin-orbit splitting Δ_{SO} values of InP bulk system are shown in table 3.1.

InP	Exp [74]	without correction	$\beta_{\mathrm{In}} = 0.14$ $\beta_{\mathrm{P}} = -0.10$	$\beta_{\mathrm{In}} = 0.03$ $\beta_{\mathrm{P}} = -0.07$
E_{gap} (eV)	1.43	0.28	1.43	0.91
ΓL gap (eV)	1.93	1.18	2.21	1.74
ΓX gap (eV)	2.19	1.62	2.40	2.15
Δ_{SO} (meV)	0.11	0.13	0.11	0.11
$m_{\mathrm{e}}^{*}(m_0)$	0.08	0.03	0.12	0.08
$E_{\mathrm{gap}}/m_{\mathrm{e}}^{*}$	17.88	9.33	11.92	11.38

Table 3.1: m_{e}^{*}, band-gap, ΓL and ΓX gaps of InP bulk in experiment and theory with and without β corrections. ($\beta_{\mathrm{In-s}} = 0.14, \beta_{\mathrm{P-p}} = -0.10$) aim to correct the band-gap while ($\beta_{\mathrm{In-s}} = 0.03, \beta_{\mathrm{P-p}} = -0.07$) aim to correct the effective mass of electron.

Though we can not correct both band-gap and m_{e}^{*} precisely at the same time, the correction of band-gap leads to a significant improvement of m_{e}^{*} compared to the non-corrected value. Interestingly, our calculation shows a quite stable value of the ratio between band-gap and m_{e}^{*} regardless of β_l parameters.

The band structures of InP bulk system before and after β correction are shown in figure 3.2. For calculations of InP nanocrystals we use $\beta_{\mathrm{In-s}} = 0.14$ and $\beta_{\mathrm{P-p}} = -0.10$.

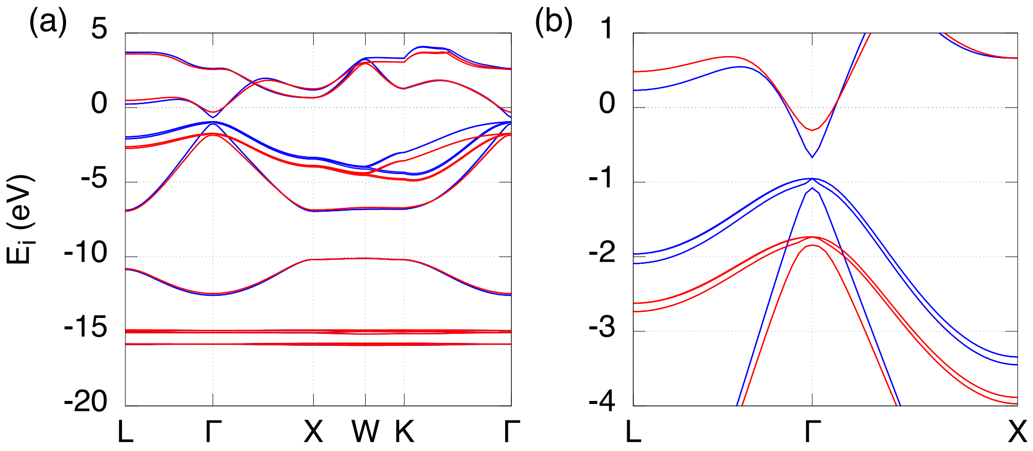

Figure 3.2: (a) Band structure of InP before (blue curves) and after(red curves) corrections.(b) The magnification of (a) in the vicinity of Γ points.

The modified pseudopotentials of In and P are illustrated in figure 3.3, the positive value of $\beta_{\mathrm{In-s}}$ increases the modified s component pseudopotential of In while the negative value of $\beta_{\mathrm{P-p}}$ lowers the p component pseudopotential of P.

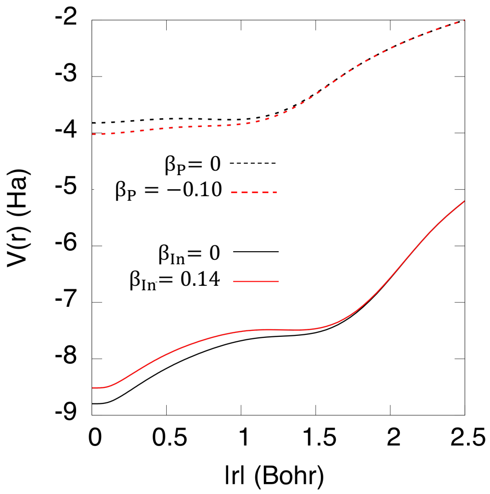

Figure 3.3: Solid curves: In pseudopotential before (black curve) and after (red curve) modification. Dash curves: P pseudopotential before (black curve) and after (red curve) modification.

3.3 Result for CdSe

The effective masses, band-gaps, ΓL, ΓX gaps, and Δ_{SO} values of ZB CdSe bulk system are shown in table 3.2.

ZB CdSe	Exp [74]	GW-PP [36]	without correction	$\beta_{\mathrm{Cd}} = 0.14$ $\beta_{\mathrm{Se}} = -0.18$	$\beta_{\mathrm{Cd}} = 0.10$ $\beta_{\mathrm{Se}} = -0.10$
Band-gap (eV)	1.82	1.48	0.097	1.82	1.10
ΓL gap (eV)	#	3.39	1.94	3.55	2.87
ΓX gap (eV)	#	3.95	2.78	4.19	3.55
Δ_{SO} (meV)	0.42	#	0.41	0.46	0.45
$m_{\mathrm{e}}^{*}(m_0)$	0.13	#	0.025	0.21	0.13
$E_{\mathrm{gap}}/m_{\mathrm{e}}^{*}$	14.00	#	3.88	8.67	8.46

Table 3.2: m_{e}^{*}, band-gap, ΓL and ΓX gaps of CdSe bulk in experiment and theory with and without β corrections. ($\beta_{\mathrm{Cd-s}} = 0.14, \beta_{\mathrm{Se-p}} = -0.18$) aim to correct the band-gap while ($\beta_{\mathrm{Cd-s}} = 0.10, \beta_{\mathrm{Se-p}} = -0.10$) aim to correct the effective mass of electron.

Similar to InP, the ratio between band-gap and m_{e} of ZB CdSe bulk changes very slightly with respect to β parameters. We correct the band-gap to the experimental value at $0K$ temperature with $\beta_{\mathrm{Cd-s}} = 0.14$ and $\beta_{\mathrm{Se-p}} = -0.18$. After the correction, the spin-orbit splitting Δ_{SO} is about 9% overestimated but with 420 meV of Δ_{SO}, the SO band locates quite deep under VBM and does not influence that much to the optical properties of CdSe systems. As the experimental values of ΓL, ΓX gaps are not available, we compare them to GW-PP calculations which are expected to be at high quality.

The band structures of ZB CdSe bulk system before and after β correction are shown in figure 3.4.

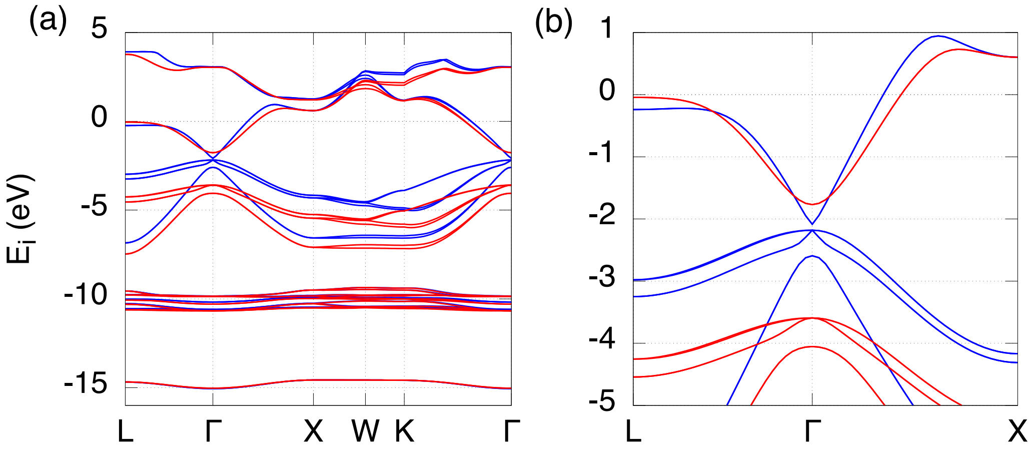

Figure 3.4: (a) Band structure of ZB CdSe before (blue curves) and after (red curves) corrections.(b) The magnification of (a) in the vicinity of Γ points.

In Wurtzite CdSe bulk, the broken symmetry in the z direction (or c axis) leads to the so-called CF splitting Δ_{CF}, which is the splitting between the A- and the B-band holes. In our calculations, the lattice parameters are determined by an Abinit relaxation with a fixed value of the ratio $c/a = 1.633$. The internal parameter u defined as the nearest neighbour distance along the c-axis in the unit of c is then 0.375, which are the ideal values of c and u for CdSe Wurtzite structure. A significant deviation from the ideal values of c and u leads to severe distortions of A, B bands, and can change the electronic and optical properties of WZ CdSe systems. Data of WZ CdSe bulk are presented in table 3.3. The band structures of WZ CdSe bulk system before and after β correction are depicted in figure 3.5.

The modified pseudopotentials of Cd and Se are illustrated in figure 3.6. Similar to InP, the positive value of $\beta_{\mathrm{Cd-s}}$ increases the s component pseudopotential of Cd while the negative value of $\beta_{\mathrm{Se-p}}$ lowers the p component pseudopotential of Se.

WZ CdSe	m_e^* (m_0)	$m_A^{*\parallel}$ (m_0)	$m_A^{*\perp}$ (m_0)	$m_B^{*\parallel}$ (m_0)	$m_B^{*\perp}$ (m_0)	Band-gap (eV)	Δ_{CF} (meV)	Δ_{SO} (eV)
Exp [74]	0.12	≥ 1	0.45	#	0.9	1.83	26	0.42
without correction	0.03	1.33	0.06	0.03	0.08	0.16	38	0.40
$\beta_{Cd} = 0.11$ $\beta_{Se} = -0.18$	0.19	1.74	0.42	0.25	0.39	1.83	27	0.45
$\beta_{Cd} = 0.10$ $\beta_{Se} = -0.05$	0.12	1.48	0.17	0.11		0.78	32	0.49

Table 3.3: Effective masses, band-gap, CF splitting Δ_{CF} and spin-orbit splitting Δ_{SO} of WZ CdSe bulk in experiment and theory with and without β corrections.

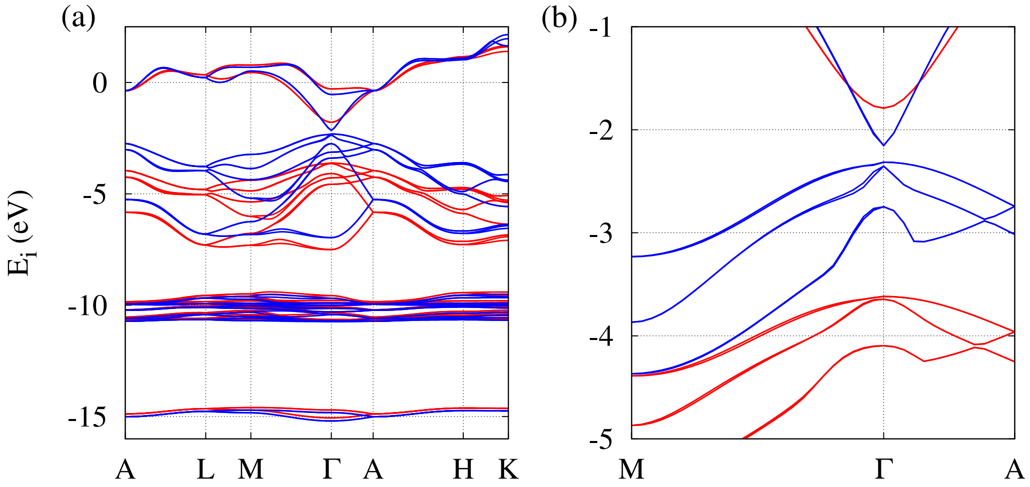

Figure 3.5: (a) Band structure of WZ CdSe before (blue curves) and after (red curves) corrections.(b) The magnification of (a) in the vicinity of Γ points.

3.4 Result for HgTe

HgTe has emerged as an interesting material for decades due to its unique electronic properties [22, 43, 88, 91]. HgTe bulk is a semi-metal with the Fermi level lying between the heavy hole and light hole bands, while the Γ_6 band in the band structure of HgTe is lower in energy compared to the Γ_8 (heavy hole and light hole) bands (see figure 3.7). Original LDA calculation of the band structure of HgTe predicts an incorrect order of Γ_6 and Γ_7 bands. The β correction not only gives the correct order of Γ_6 and Γ_7 bands (see figure 3.7) but also produces correct values of level splittings and effective masses (see table 3.4).

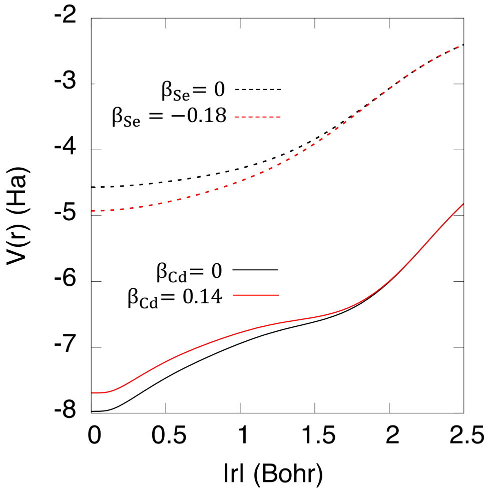

Figure 3.6: Solid curves: Cd pseudopotential before (black curve) and after (red curve) modification. Dash curves: Se pseudopotential before (black curve) and after (red curve) modification.

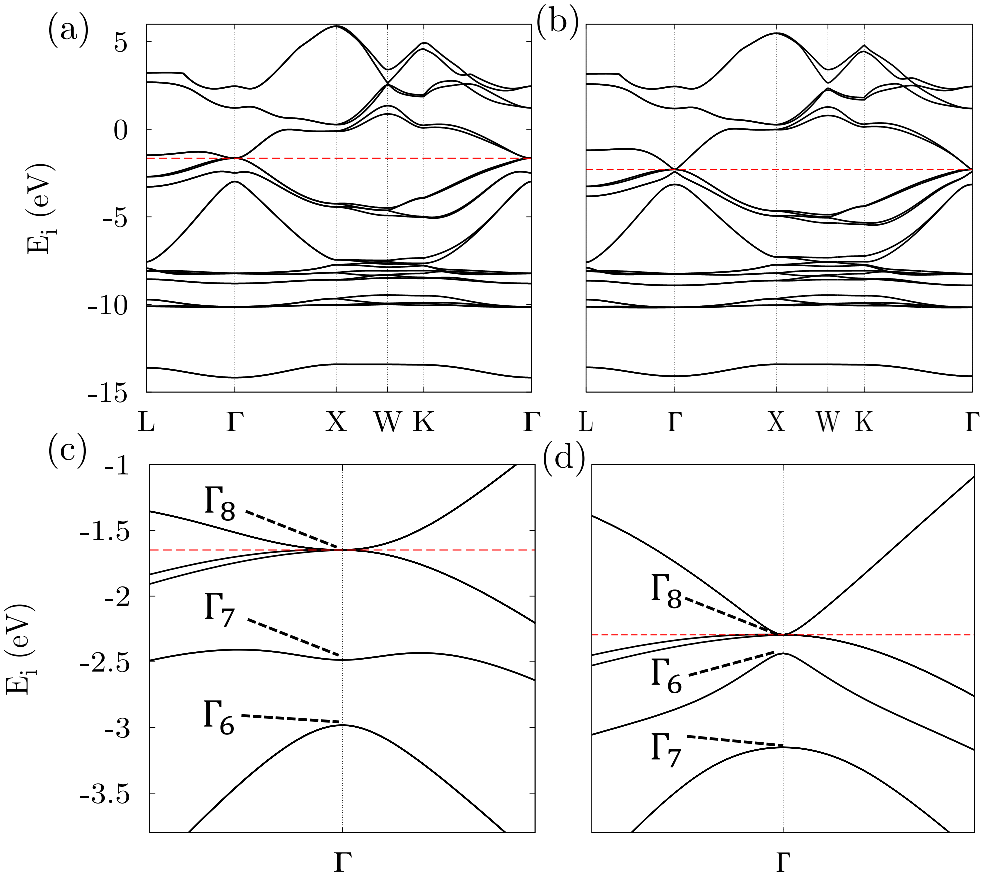

Figure 3.7: Band structure of HgTe (a) before and (b) after β_l correction. Figure (c) and (d) are magnifications of figures (a) and (b) respectively in the vicinity of Γ point. Red line indicates the Fermi level.

Tabel 3.4 shows good agreement between our results and experiment and other theoretical methods. As in typical semiconductors, band-gap is defined as the splitting between the Γ_8 and Γ_6 bands, Δ_{SO} is the splitting between the Γ_8 and Γ_7 bands.

HgTe	Band-gap (eV)	Δ_{SO} (eV)	$m_{\mathrm{lh}}(\Gamma_8)$ (m_0)	$m_{\mathrm{hh}}(\Gamma_8)$ (m_0) [100]	$m_{\mathrm{hh}}(\Gamma_8)$ (m_0) [110]	$m_{\mathrm{hh}}(\Gamma_8)$ (m_0) [111]	$m(\Gamma_6)$ (m_0)
without correction	-1.30	0.837	0.167	0.210	0.699	1.089	0.216
$\beta_{\mathrm{Hg}} = 0.18$ $\beta_{\mathrm{Te}} = -0.18$	-0.14	0.856	0.023	0.337	0.928	1.327	0.024
HSE [85]	-0.27	0.890	#	#	#	#	#
EPM [91]	-0.29	0.898	0.039	0.933	1.559	2.022	0.050
k.p [91]	-0.29	0.898	0.052	0.948	1.271	1.429	0.069
Exp[74]	-0.14	1.080	0.031	0.321	0.406	0.445	0.028

Table 3.4: Effective masses, band-gap and spin-orbit splitting Δ_{SO} of HgTe bulk in experiment and theory with and without β corrections.

The modified pseudopotentials of Hg and Te are illustrated in figure 3.8.

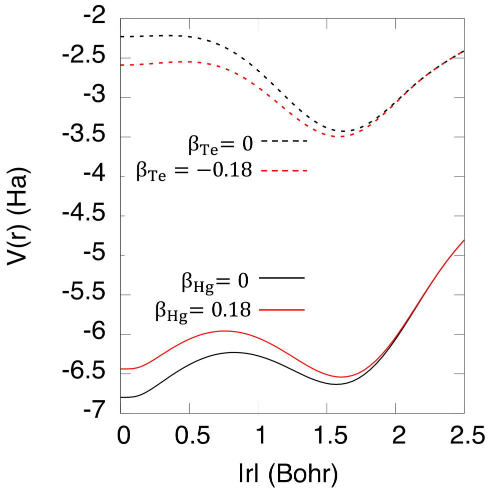

Figure 3.8: Solid curves: Hg pseudopotential before (black curve) and after (red curve) modification. Dash curves: Te pseudopotential before (black curve) and after (red curve) modification.

The β corrections shift the eigenvalues around band-edge but do not change the main feature of band structures. The projections of the wave functions after correction onto that before correction are always more than 0.95 indicating that the wave function is not significantly affected by the β corrections.

In summary, our correction scheme based on a modification of the non-local part of norm-conserving pseudopotentials allows us to correct the effective masses, band-gap, ΓL, ΓX gaps, Δ_{SO} and Δ_{CF} and keep the wavefunction nearly unchanged at the LDA quality. That is a good starting point to study the optical properties of nanocrystals.

Chapter 4

Configuration interaction method

Configuration interaction (CI) is the matrix mechanics solution of the time-independent non-relativistic electronic Schrödinger equation. Moreover, it is one of the most effective improvements of the Hartree-Fock theory by adding the correlation effect. While wave-function is a single Slater determinant in the Hartree-Fock method, the CI wave-function is a linear combination of Slater determinants, with the linear coefficients being determined variationally. In this chapter, we introduce the method for a systematic generation of Slater determinants starting from the one-electron orbitals obtained from the Ab inito calculation.

4.1 N-particle wave-function

To construct the N-particle basis function we follow the arguments of Szabo and Ostlund [103]. Assume we have a complete set of functions $\psi_i(x_1)$ of a single variable x_1. Then any function $\phi(x_1)$ can be expanded as

$$\phi(x_1) = \sum_i a_i \psi_i(x_1). \tag{4.1}$$

Now we consider a two-particle system and the function $\phi(x_1, x_2)$. If we fix x_2, then

$$\phi(x_1, x_2) = \sum_i a_i(x_2) \psi_i(x_1), \tag{4.2}$$

where $a_i(x_2)$ is a function of variable x_2 and can be written as

$$a_i(x_2) = \sum_j b_{ij}\psi_j(x_2). \tag{4.3}$$

From 4.2 and 4.3 we have

$$\phi(x_1, x_2) = \sum_{ij} b_{ij}\psi_i(x_1)\psi_j(x_2). \tag{4.4}$$

The same process can be expanded for N-particle wave-function $\phi(x_1, x_2, ..., x_N)$. However, by the Pauli exclusion principle, the many-particle wave-function must be anti-symmetric with respect to the exchange of the coordinates of any two electrons. In the case of $\phi(x_1, x_2)$, it means

$$\phi(x_1, x_2) = -\phi(x_2, x_1). \tag{4.5}$$

It is equivalent to $b_{ij} = -b_{ji}$ and $b_{ii} = 0$, or

$$\phi(x_1, x_2) = \sum_{j>i} b_{ij}[\psi_i(x_1)\psi_j(x_2) - \psi_j(x_1)\psi_i(x_2)]. \tag{4.6}$$

In determinant form

$$\phi(x_1, x_2) = b_{ij} \begin{vmatrix} \psi_i(x_1) & \psi_j(x_1) \\ \psi_i(x_2) & \psi_j(x_2) \end{vmatrix}. \tag{4.7}$$

Similarly, any N-particle wave-function can be constructed as a linear combination of all possible N-particle Slater determinants formed from a complete set of single-particle wave-function $\psi_i(x)$. The solution of equation (1.1) in this complete basis set can be described as

$$|\Psi_j\rangle = \sum_i c_{ij} |\phi_i\rangle, \tag{4.8}$$

where $|\phi_i\rangle$ denotes N-particle basis functions and can be written as substitutions or excitations from the Hartree-Fock "reference" determinants, i.e.

$$|\Psi_j\rangle = c_0 |\phi_0\rangle + \sum_{ra} c_a^r |\phi_a^r\rangle + \sum_{a<b,r>s} c_{ab}^{rs} |\phi_{ab}^{rs}\rangle + \sum_{r<s<t,a<b<c} c_{abc}^{rst} |\phi_{abc}^{rst}\rangle + ... \tag{4.9}$$

where $|\phi_a^r\rangle$ means Slater determinant formed by replacing spin-orbital a in $|\phi_0\rangle$ with spin-orbital r, etc.

In most of the case, it is impossible to get a complete set of single-particle basis function $\{\psi_i(x)\}$. Instead, a large enough basis set is used to produce useful results with a reasonable computational cost. The quality of the single-particle basis set can be checked by comparing the results of calculations using a progressively larger basis set. If the calculation is done with all possible N-particle basis functions $\{|\phi_i\rangle\}$ formed by a given single-particle basis set $\{\psi_i(x)\}$ then it is called full-CI calculations. In case of the complete single-particle basis set $\{\psi_i(x)\}$, the calculation is complete-CI. Unfortunately, even with incomplete single-particle basis set, a full-CI calculation is still computationally expensive, leading to a requirement of the reduced CI space. So far, the most used CI approximation is CI singles and doubles (CISD), which includes only those N-particle basis functions which represent single or double excitations relative to the reference state.

4.2 CI calculation procedure

In the first step, we solve the single-particle Schrödinger equation using the AEP approach [21, 61, 116], which allows us to study NCs with experimental sizes with Ab initio quality wave functions $\psi_i(\mathbf{r}, \sigma)$. The AEPs are directly obtained from density functional theory [21] using the local density approximation (LDA) [75] for the exchange-correlation functional. As already mentioned in the previous chapter, the empirical β correction on the non-local part of pseudopotential is invoked for correct band-gap and effective masses.

In the second step, we use the AEP single-particle basis functions set $|\phi_i\rangle$ to construct a set of single-substitution Slater determinants $\Phi_{\mathrm{h,e}}$ obtained from the ground-state Slater determinant Φ_0 by promoting an electron from the occupied valence band state ψ_{h} with energy ε_{h} to the unoccupied conduction band state ψ_{e} with energy ε_{e} [8, 38]. The exciton wavefunctions Ψ^{α} (where α denotes the exciton quantum numbers) are expanded in terms of this determinantal basis set [38]:

$$\Psi^{\alpha} = \sum_{\mathrm{h}}^{N_{\mathrm{h}}} \sum_{\mathrm{e}}^{N_{\mathrm{e}}} C^{\alpha}_{\mathrm{h,e}} \Phi_{\mathrm{h,e}} \tag{4.10}$$

N_{h} and N_{e} denote the number of valence (states below the Fermi level that can be occupied by holes) and conduction band states (states above the Fermi level that can be occupied by electrons) included in the expansion of the exciton wavefunctions. The matrix elements of the many-particle Hamiltonian H in the basis set $\Phi_{\mathrm{h,e}}$ are calculated as [38]:

$$
\begin{aligned}
H_{\mathrm{he,h'e'}} &= \langle \Phi_{\mathrm{h,e}} | \, H \, | \Phi_{\mathrm{h',e'}} \rangle \\
&= (\varepsilon_{\mathrm{e}} - \varepsilon_{\mathrm{h}}) \delta_{\mathrm{h,h'}} \delta_{\mathrm{e,e'}} - J_{\mathrm{he,h'e'}} + K_{\mathrm{he,h'e'}}
\end{aligned}
\tag{4.11}
$$

where J and K are the Coulomb and exchange integrals, respectively:

$$
J_{\mathrm{he,h'e'}} = e^2 \sum_{\sigma_1,\sigma_2} \int\int \frac{\psi^*_{\mathrm{h'}}(\mathbf{r}_1,\sigma_1)\psi^*_{\mathrm{e}}(\mathbf{r}_2,\sigma_2)\psi_{\mathrm{h}}(\mathbf{r}_1,\sigma_1)\psi_{\mathrm{e'}}(\mathbf{r}_2,\sigma_2)}{\epsilon(\mathbf{r}_1,\mathbf{r}_2)|\mathbf{r}_1-\mathbf{r}_2|} d\mathbf{r}_1 d\mathbf{r}_2, \tag{4.12}
$$

$$
K_{\mathrm{he,h'e'}} = e^2 \sum_{\sigma_1,\sigma_2} \int\int \frac{\psi^*_{\mathrm{h'}}(\mathbf{r}_1,\sigma_1)\psi^*_{\mathrm{e}}(\mathbf{r}_2,\sigma_2)\psi_{\mathrm{e'}}(\mathbf{r}_1,\sigma_1)\psi_{\mathrm{h}}(\mathbf{r}_2,\sigma_2)}{\epsilon(\mathbf{r}_1,\mathbf{r}_2)|\mathbf{r}_1-\mathbf{r}_2|} d\mathbf{r}_1 d\mathbf{r}_2. \tag{4.13}
$$

The screening function $\epsilon(\mathbf{r}_1, \mathbf{r}_2)$ is microscopic, i.e. it naturally includes the full range (long- and short-range) of interaction and homogeneous: $\epsilon(\mathbf{r}_1, \mathbf{r}_2) = \epsilon(|\mathbf{r}_1 - \mathbf{r}_2|)$. The inverse dielectric function in reciprocal space $\epsilon^{-1}(k)$ includes an electronic (high-frequency) $\epsilon^{-1}_{\mathrm{el}}$ and an ionic (low-frequency) contribution $\epsilon^{-1}_{\mathrm{ion}}$ [38, 49]:

$$
\epsilon^{-1}(k) = \epsilon^{-1}_{\mathrm{el}}(k) + \epsilon^{-1}_{\mathrm{ion}}(k). \tag{4.14}
$$

The electronic part $\epsilon^{-1}_{\mathrm{el}}$ is approximated by the Thomas-Fermi model proposed by Resta [95] and the ionic (or polaronic) part $\epsilon^{-1}_{\mathrm{ion}}$ is described by Haken [49]:

$$
\epsilon^{-1}_{\mathrm{el}}(k) = \frac{k^2 + q^2 \sin(k\rho_\infty)/(\epsilon^{\mathrm{dot}}_\infty k \rho_\infty)}{k^2 + q^2}, \tag{4.15}
$$

$$
\Delta\epsilon^{-1}_{\mathrm{ion}}(k) = \Big(\frac{1}{\epsilon^{\mathrm{dot}}_0} - \frac{1}{\epsilon^{\mathrm{dot}}_\infty}\Big) + \Big(\frac{1/2}{1+\rho^2_{\mathrm{h}}k^2} + \frac{1/2}{1+\rho^2_{\mathrm{e}}k^2}\Big). \tag{4.16}
$$

Here $q = 2\pi^{-1/2}(3\pi^2 n_0)^{1/3}$ is the Thomas-Fermi wave vector, n_0 is the valence electron density, ρ_∞ is the screening radius which can be calculated from $\sinh(q\rho_\infty)/(q\rho_\infty) = \epsilon^{\mathrm{dot}}_\infty$, and $\rho_{\mathrm{h,e}} = (\hbar/2m_{\mathrm{h,e}}\omega_{\mathrm{LO}})^{1/2}$, where $m_{\mathrm{h,e}}$ are hole (h) and electron (e) effective masses, ω_{LO} is the frequency of the bulk LO phonon mode [38]. The high-frequency dielectric constant of the NC is obtained from a modified Penn model [38, 90],

$$
\epsilon^{\mathrm{dot}}_\infty(R) = 1 + (\epsilon^{\mathrm{bulk}}_\infty - 1)\frac{\big[E^{\mathrm{bulk}}_{\mathrm{gap}} + \Delta E\big]^2}{\big[E^{\mathrm{dot}}_{\mathrm{gap}} + \Delta E\big]^2} \tag{4.17}
$$

where $\epsilon^{\mathrm{bulk}}_\infty$ is the bulk high-frequency dielectric constant of the underlying bulk, $E^{\mathrm{bulk}}_{\mathrm{gap}}$ and $E^{\mathrm{dot}}_{\mathrm{gap}}$ are the single-particle bulk and NC band gaps, ΔE denotes the difference between the so-called E_2 and E_0 transitions in bulk. E_2 is the transition with the strongest absorption in a semiconductor with tetrahedral crystal structure [113]. The low-frequency dielectric constant is given as [38]:

$$\epsilon_0^{\mathrm{dot}}(R) = \epsilon_\infty^{\mathrm{dot}}(R) + (\epsilon_0^{\mathrm{bulk}} - \epsilon_\infty^{\mathrm{bulk}}). \tag{4.18}$$

So the dielectric function depends both on the electron-hole separation and the NC size. The final step is the diagonalization of the many-body Hamiltonian.

Some parameters in the Thomas-Fermi and Haken models of InP, CdSe, and HgTe are shown in table 4.1.

Unit: a.u	q	ρ_h	ρ_e	$\epsilon_\infty^{\mathrm{bulk}}$	$\epsilon_0^{\mathrm{bulk}}$	ΔE
InP	1.303	22.34	63.18	9.61	12.56	3.13
CdSe	1.256	33.70	63.40	9.30	6.20	$4.03^{ZB}/4.77^{WZ}$
HgTe	1.198	55.20	174.70	15.20	21.00	2.64

Table 4.1: Parameters in the Thomas-Fermi and Haken models of InP, CdSe, and HgTe

High and low-frequency dielectric constants of InP, CdSe, and HgTe nanocrystals are presented in figures 4.1, 4.2, and 4.3, respectively. It is shown that the macroscopic dielectric constant increases significantly with the size of quantum dot; therefore, reducing the Coulomb and exchange interactions.

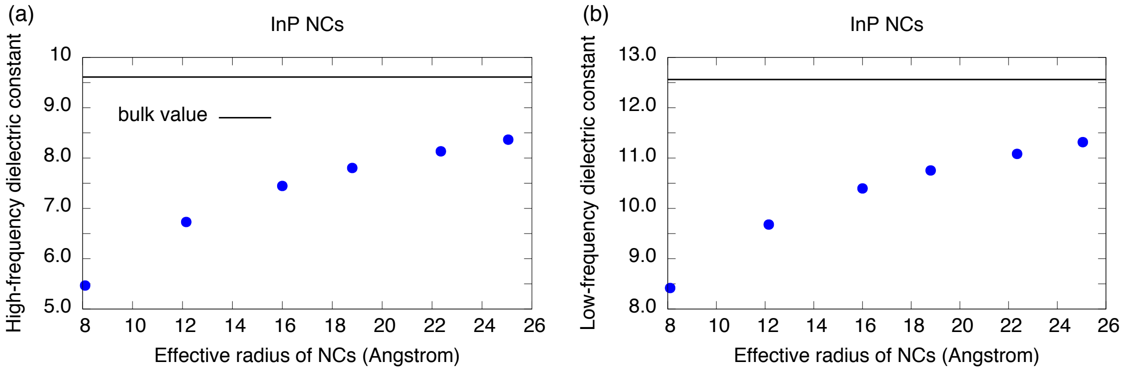

Figure 4.1: Size-dependence of (a) $\epsilon_\infty^{\mathrm{bulk}}(R)$ and (b) $\epsilon_0^{\mathrm{bulk}}(R)$ of InP quantum dots. Black lines present high- and low-frequency dielectric constant of InP bulk which are 9.61 and 12.56 [74], respectively.

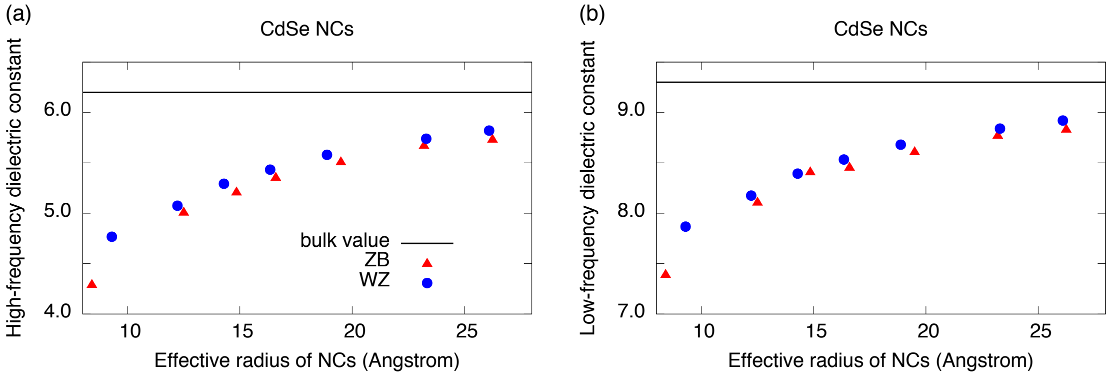

Figure 4.2: Size-dependence of (a) $\epsilon_{\infty}^{\text{bulk}}(R)$ and (b) $\epsilon_{0}^{\text{bulk}}(R)$ of CdSe quantum dots. Black lines present high- and low-frequency dielectric constant of CdSe bulk which are 6.2 and 9.3 [74], respectively.

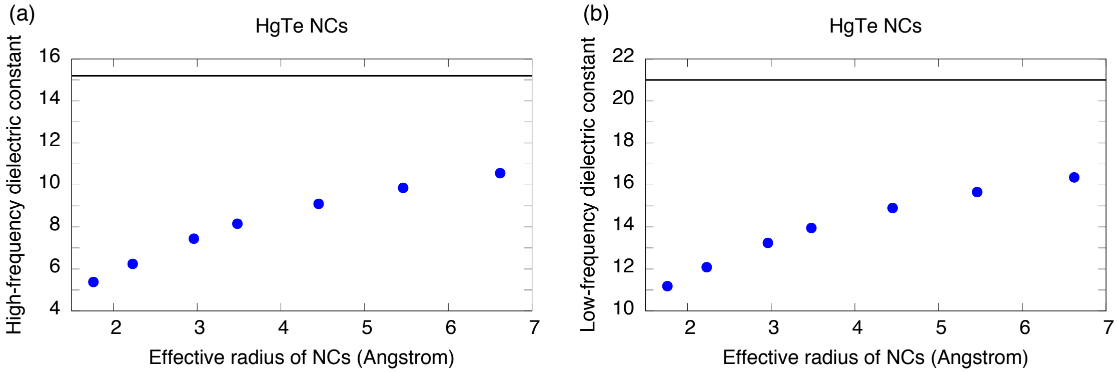

Figure 4.3: Size-dependence of (a) $\epsilon_{\infty}^{\text{bulk}}(R)$ and (b) $\epsilon_{0}^{\text{bulk}}(R)$ of HgTe quantum dots. Black lines present high- and low-frequency dielectric constant of HgTe bulk which are 15.2 and 21.0 [74], respectively.

The CI calculation procedure of electronic excitations is schematically shown in figure 4.4. The single-particle calculations are performed using the AEP method, which is implemented in the Latepp code. The MX package allows one to perform CI calculations of electronic excitations in semiconductor nanostructures with an arbitrary number of electrons in the conduction band and holes in the valence band. The package contains three codes: mxmat, mxci, and dipole, which are normally run in sequence. The codes communicate with each other via binary files.

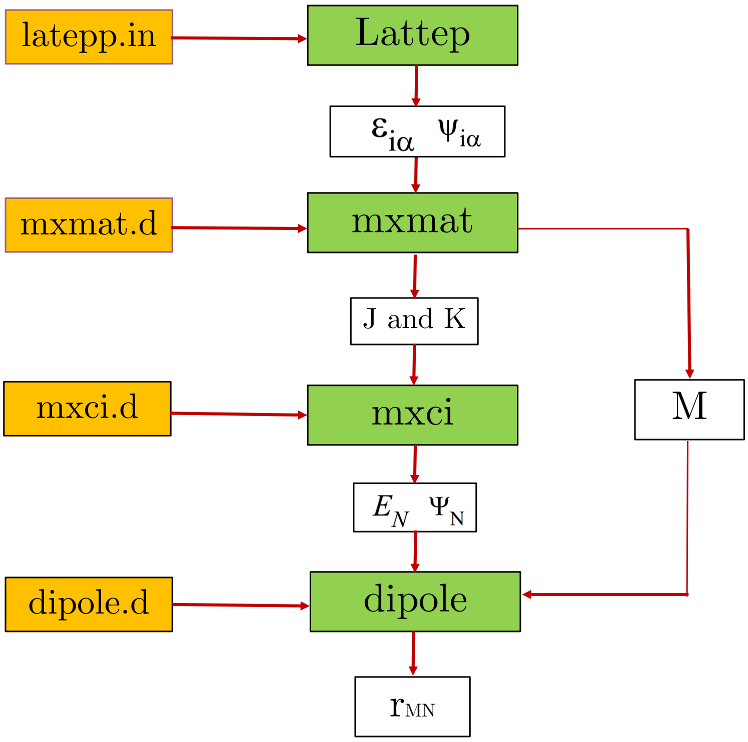
latepp.in
Lattep
$\varepsilon_{i\alpha}$ $\Psi_{i\alpha}$
mxmat.d
mxmat
J and K
mxci.d
mxci
M
E_N Ψ_N
dipole.d
dipole
r_{MN}

Figure 4.4: Diagram summarises the input and output of the calculation procedure. latepp.in, mxmat.d, mxci.d, and dipole.d are input files of Latepp, mxmat, mxci, and dipole codes, respectively.

The MX package requires as input a set of single-particle energies $\varepsilon_{i\alpha}$ and orthonormal wave-function $\psi_{i\alpha}$. Here the suffix i denotes the orbital quantum number and α denotes the spin quantum number ($\alpha = 1, 2$). The output of the MX package consists of the Coulomb and exchange integrals, the energies E_N and wave-functions Ψ_N of the N-particle electronic excited states, as well as the dipole matrix elements between the one-particle states (M) and the N-particle states (r_{MN}).

Chapter 5

Excitonic fine structure of colloidal nanocrystals

In this chapter we study the excitonic fine structure of colloidal nanocrystals (a.k.a. quantum dots) using atomic effective pseudopotentials in combination with the screened configuration interaction method and show excellent agreement with experiment. Many optical properties of nanostructures emerge as a consequence of the so-called excitonic fine structure (FS). The recombination dynamics, e.g., is strongly influenced by the splitting between the lower dark state and the energetically first bright state of the excitonic FS; the so-called dark-bright (DB) splitting. For DB splittings larger than the thermal energy, the carriers can become trapped in the lower energy dark state [10, 28, 34, 68] prohibiting an efficient emission. More generally, the polarization properties of the emission at low temperature is a result of the FS and has direct consequences for any possible application of colloidal nanocrystals (NCs) based on their optical properties [5, 13, 16, 48, 73, 102] or their spin in the area of quantum information [1, 55, 76, 114]. The excitonic FS originates from the electron-hole exchange interaction in the presence of spin-orbit coupling. In Fig. 5.1 we show a schematic picture explaining the situation in NCs with wurtzite (WZ, left) and zinc-blende (ZB, right) crystal structures, both of which can be realized experimentally for CdSe NCs. The single-particle eigenvalues for the lowest unoccupied orbitals (e_0) and the highest occupied orbitals (h_0 and h_1) create the band edge excitonic states.

In the first step in Fig. 5.1 we create the electron-hole ($e-h$) pairs as simple products of the single-particle states and without considering the FS, the states are four- or eight–fold degenerate, depending on the crystal structure. The splitting between h_0

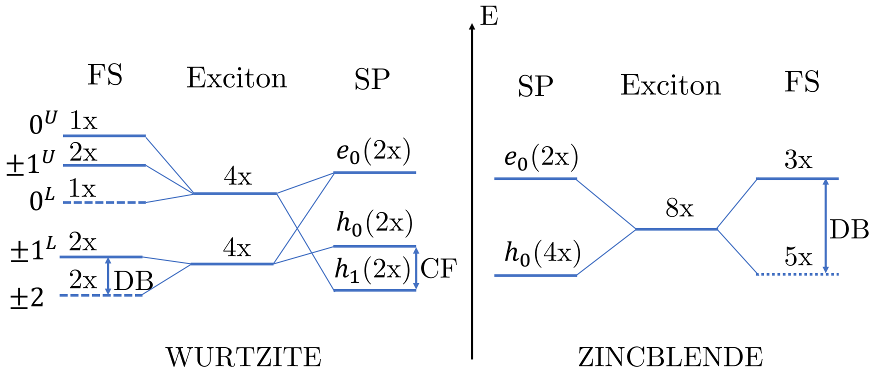

Figure 5.1: Schematic representation of the FS of "spherical" WZ and ZB NCs. The single-particle (SP) levels are labeled with e_0 (unoccupied states), $h_{0,1}$ (occupied states). The $e-h$ pair (middle) columns show the exciton without considering the exchange interaction. The energy splittings in the exciton FS are not to scale and typically in the tens of meV range. Solid (dashed) lines show optically bright (dark) states. The difference in energy between the lowest dark and bright states is the DB splitting. In WZ NCs, the h_0 and h_1 states are split by the CF splitting.

and h_1 in the WZ structure, called crystal-field (CF) splitting, originates from the lower symmetry of the WZ ($C_{3\mathrm{v}}$) compared to the ZB structure (T_d) [113]. In the next step, we include the electron-hole exchange interaction, which leads to the exciton FS, strongly magnified in Fig. 5.1. For the labeling in the WZ structure, we use for historical reasons [34] the total angular momentum J of 1 or 2, which originates from the combination of the e_0 state with $J_e^z = 1/2$ and the h_0 state with $J_h^z = 3/2$. The letters U and L refer to upper and lower. Note that the exciton states are not pure $J = 1, 2$ states and that upper/lower will also reverse order in the following. The DB splitting mentioned previously is labeled with (DB) in Fig. 5.1. Note that in the related field of epitaxial self-assembled quantum dots the ability to control the FS (and minimize it) with external fields has lead to the realization of one of the best sources of single- and entangled photons [42, 81, 83].

5.1 Excitonic fine structure of CdSe nanocrystals

In this section, we show that results of atomistic atomic effective pseudopotentials (AEPs) [21, 61, 116] in combination with screened configuration interaction [38] are in qualitative disagreement with the popular EMA model of FS [34] and its recently revisited version [98]. We show that the dark states, in general, are in qualitative disagreement with the atomistic results and especially the DB splitting. We compare our atomistic results to available experiments and show very good agreement. We further discuss the FS of ZB and WZ CdSe NCs with different aspect ratios and highlight differences and similarities. The experimentally measurable (at low temperature) FS is shown for both crystal structures as a function of NC size and ellipticity. We can quantitatively identify the aspect ratio at which the ZB and WZ structure show almost identical FS. We also show that ZB or WZ NCs with large aspect ratios (strongly prolate) exhibit similar FS as well. However, nearly spherical ZB and WZ structures have a very distinct FS.

5.1.1 Comparison to Experiment and to EMA results

First, we compare our results to existing experiments in figure 5.2. The DB splitting was measured by several groups [34, 86, 112] as a function of the size of the NCs and is shown with black symbols. All the experiments were performed on CdSe WZ NCs at low temperature. We show our results for both ZB and WZ NCs as red and blue circles, respectively. We also included earlier theoretical results based on semi-empirical pseudopotentials [38] as green squares. We can see that the theoretical results compare very well with the experiments in the entire size range.

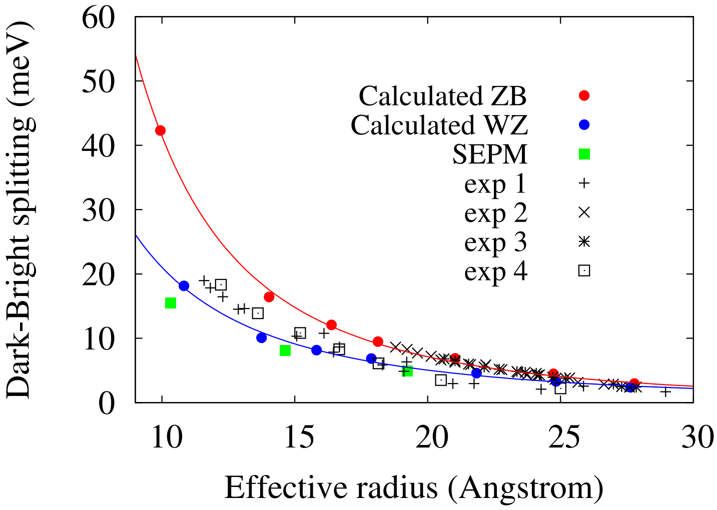

Figure 5.2: Dark-bright splittings of "spherical" ZB and WZ CdSe NCs in comparison with SEPM calculations in Ref. [38] and experiments in Refs. [34] (exp 1), [112] PLE (exp 2), [112] PL (exp 3), and [86] (exp 4).

In figure 5.3a) we directly compare our atomistic results (filled circles fitted by solid lines) to the most recent EMA results [98] (dashed lines). The five different excitonic states (see Fig. 5.1) are labeled with $\pm 2, \pm 1^L, 0^L, \pm 1^U$, and 0^U and shown in red, blue, black, orange, and purple, respectively. To compare atomistic and EMA results, lines of the same color should be compared as these belong to the same states. All the states are aligned to the ±2 (red) state, consequently, the atomistic and EMA results for ±2 (red) overlap. The comparison reveals that both results are in qualitative disagreement. Most striking are $\pm1^L$ states that show an opposite curvature as a function of NC radius. Also the 0^L states show no size dependence in the EMA, while it is strongly increasing in the atomistic calculations. If we exclude the exchange interaction in the CI calculation, the size-dependence of the splitting between 0^L and ±2 states is unchanged, implying that the origin of this splitting is not the exchange interaction but the confinement effect on the crystal field splitting. Therefore, our suggestion to improve the EMA is to introduce a size-dependent crystal field splitting.

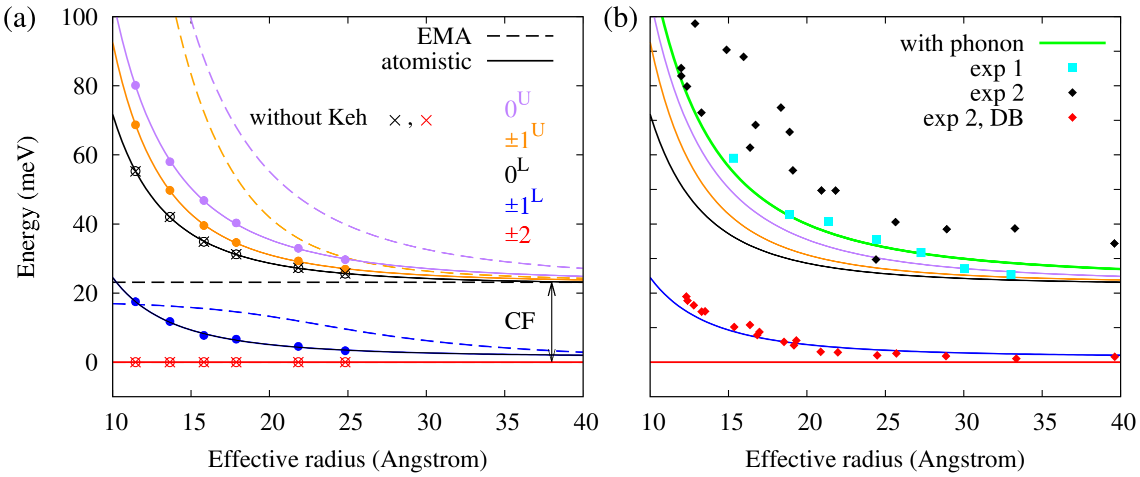

Figure 5.3: Exciton FS versus radius of “spherical” WZ NCs. (a) Comparison between atomistic results (circles and solid lines) and EMA (dashed lines) for the five different exciton states $\pm2, \pm1^L, 0^L, \pm1^U$ and 0^U (see figure 5.1). Filled and empty circles represent bright and dark states, respectively. The crosses show excitonic states without electron-hole exchange interaction, in this case, ±2 and $\pm1^L$ are degenerate; 0^L, $\pm1^U$, and 0^U are degenerate. The results are aligned to the ±2 states. (b) Comparison between atomistic theoretical results and experiments. The thick green curve represents the atomistic calculations including the lattice relaxation phononic effect taken from Ref. [51]. Exp 1, exp 2 refer to the experiments from Refs. [87] and [34], respectively.

In figure 5.3b) we show a further, more detailed, comparison between the atomistic results and experiment. The experiments (exp 1 [34], exp 2 [87]) probe the energy shift between the absorption and the emission peaks, the so-called Stokes shift. Our calculations use the same crystal structure in the excited and in the ground state. The experiment, on the other hand, probes two different geometries, since the geometry of the excited states is relaxed before emission. This structural relaxation effect (the reorganization energy) was calculated *ab-initio* for CdSe colloidal QDs in Ref. [51] and we use the values obtained there to correct our “static” results. The final results are shown as thick green line in figure 5.3b) and compare extremely well with the results of “exp 1” and the small sized NCs of “exp 2”. Experimental results for larger NCs in ”exp 2” [34] are somewhat higher and it resembles a general shift to higher energy. Striking is the fact that the experimental results do not seem to converge to the bulk crystal field splitting for the largest radii shown in figure 5.3b) but to a somewhat larger value. We could speculate that the NCs are strained, but further studies would be necessary to confirm this hypothesis. Our results for the DB splitting are in very good agreement with the results of ”exp 2, DB” [34] (see figure 5.3).

Our final comparison to experiment requires the calculation of the oscillator strength of the different transitions. We first present our theoretical results in Figure 5.4 where we show the absorption as a function of the energy and NC size for (a) “spherical” NCs (the real NCs are somewhat faceted, because of the atomistic construction) and slightly prolate NCs, with an aspect ratio (length along the c-axis divided by in-plane diameter) around 1.16. The blue curves show transitions polarized in-plane and the red curves show transitions polarized along the c-axis in the WZ structure. The energy transitions correspond to the state $\pm 1^L$, $\pm 1^U$ and 0^L (see figure 5.1), in order of increasing energy. It is striking that the oscillator strength is significantly reduced for the lower energy $\pm 1^L$ transition in the prolate NCs.

Another way to plot these results is shown in Fig. 5.5, where the sum of the oscillator strength of the $\pm 1^U$ and 0^U (black and blue in figure 5.5) and the oscillator strength of $\pm 1^L$ (red and green in figure 5.5) are shown, both normalized to the total oscillator strength. The results for the “spherical” NC are shown as stars, and for the slightly prolate NCs as circles. The experimental results [87] are shown as open red and black circles. We can see that the theoretical results fit very well to experiment for the slightly elongated structures. This is in agreement with the many observations that the synthesized WZ CdSe NCs are not perfectly spherical but slightly elongated with an AR varying from 1.0 to 1.3 [82, 84, 87].

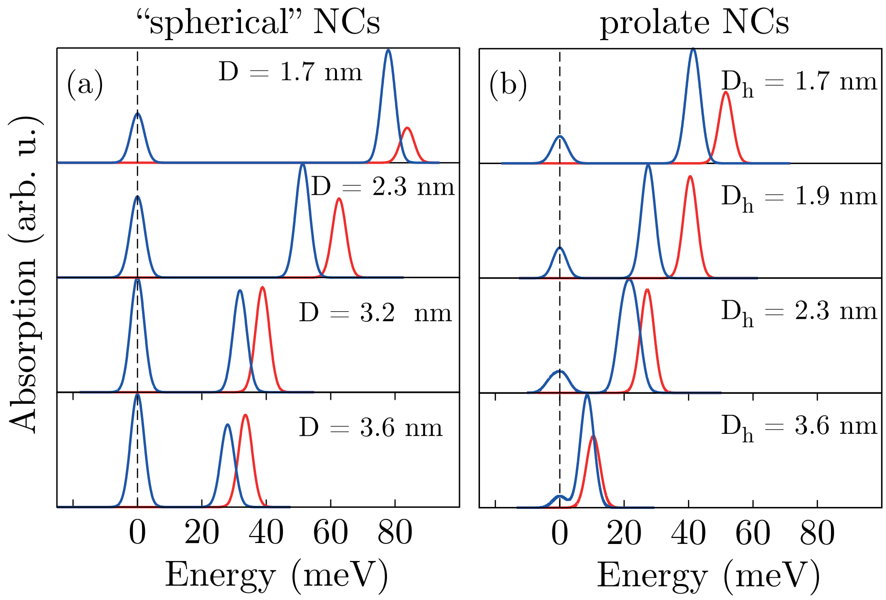

Figure 5.4: Oscillator strength of (a) spherical WZ CdSe NCs and (b) slightly elongated WZ CdSe NCs. Red peaks are z-polarized (along c-axis in WZ and [001] in ZB) and blue peaks are in-plane polarized. All spectra are aligned at the $\pm 1^L$ peak which is marked by the black dashed line.

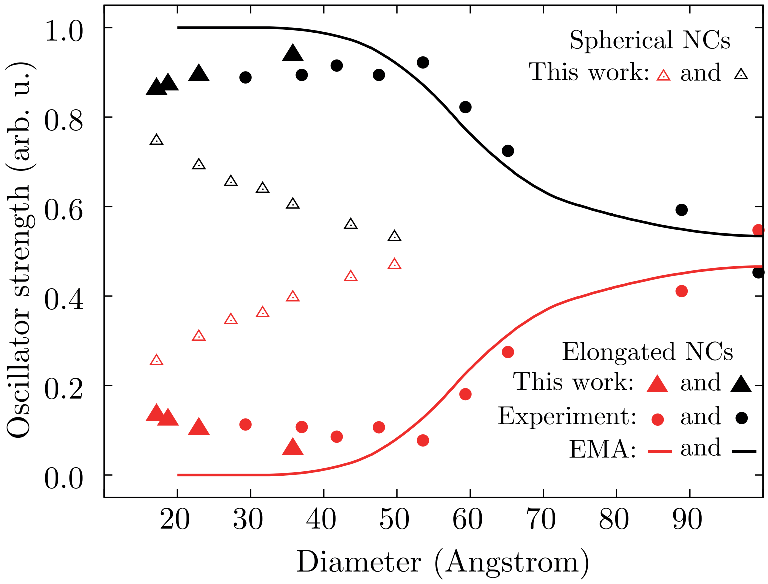

Figure 5.5: Oscillator strength calculated for spherical (empty triangle) and slightly prolate (filled triangle) WZ CdSe NCs in comparison with experimental measurement [87] (black and red circles) and with EMA results (solid lines). Results shown in red (line, circle, triangles) represent the oscillator strength of the $\pm 1^L$ state. Results shown in black (line, circle, triangles) represent the sum of the oscillator strength of the 0^U and $\pm 1^U$ states. The total oscillator transition strength of three bright excitons is normalized to one.

5.1.2 Comparison between the FS of WZ and ZB NCs.

A schematic representation for the FS of WZ and ZB was shown for “spherical” NCs in figure 5.1. The term “spherical” stands for the overall shape, which is as close as possible to spherical but remains faceted (where the facets are determined by the underlying atomic lattice). An alternative description is based on the point-group symmetry of the entire NCs; which is T_d for the “spherical” ZB NCs and C_{3v} for the “spherical” WZ NCs. An elongation of the ZB NCs along the [001] axis leads to a symmetry reduction to C_{3v}. In figure 5.6 we schematically illustrate how the point group symmetry changes when going from a “spherical” to an ellipsoidal (oblate) shape, for ZB NCs. We consider first the larger effect of the splitting of the single-particle valence band states to then include the electron-hole exchange interaction to obtain the FS. From this schematic representation we can see that the elongation has the effect to split the degenerate valence band states of Γ_8 symmetry into two, akin the splitting into heavy- and light-hole states in a quantum well [113]. The CF splitting in the WZ structure (figure 5.1) corresponds to this elongation-induced splitting in the ZB NCs. The final FS is qualitatively very similar between the elongated ZB and the WZ structures according to Fig. 5.6. In the case of a prolate shape, the Γ_4 and the $\Gamma_5 \oplus \Gamma_6$ states are energetically in reversed order and the FS accordingly.

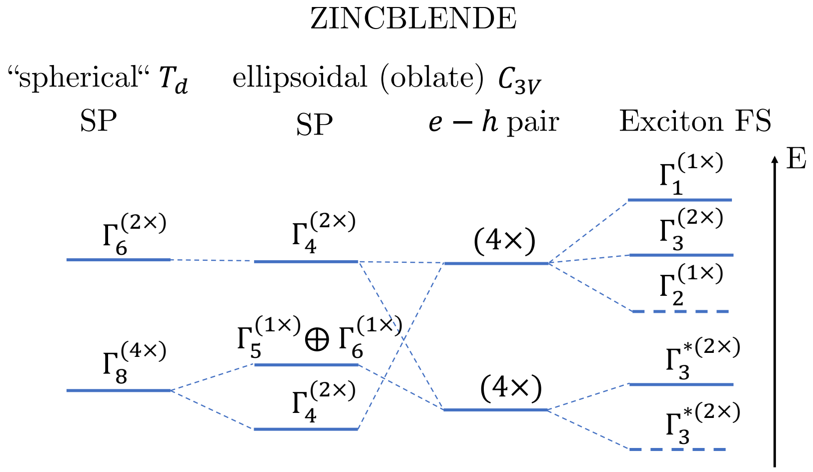
ZINCBLENDE
“spherical“ T_d
SP
ellipsoidal (oblate) C_{3V}
SP
$e-h$ pair
Exciton FS
E
$\Gamma_6^{(2\times)}$
$\Gamma_8^{(4\times)}$
$\Gamma_4^{(2\times)}$
$\Gamma_5^{(1\times)} \oplus \Gamma_6^{(1\times)}$
$\Gamma_4^{(2\times)}$
(4×)
(4×)
$\Gamma_1^{(1\times)}$
$\Gamma_3^{(2\times)}$
$\Gamma_2^{(1\times)}$
$\Gamma_3^{*(2\times)}$
$\Gamma_3^{*(2\times)}$

Figure 5.6: Schematic representation of the FS in “spherical” and oblate ZB NCs. The single-particle (SP) and exciton FS levels are labeled by their irreducible representations. The energy splittings in the FS are not to scale and typically in the range of tens of meV. Solid (dashed) lines show optically bright (dark) states.

We now proceed to calculate quantitatively the FS of ellipsoidal ZB and WZ NCs.

Two examples of the atomistic structures we use in the calculation of the larger structures with D_h = 3.6 nm are given in figure 5.7. The oblate NC includes 183 Cd, 208 Se and 236 pseudo-H atoms. The prolate NC includes 541 Cd, 580 Se, and 432 pseudo-H atoms. For the smaller NCs with $D_h = 2.8$ nm we use a cylindrical shape terminated by two half-spheres as the elliptical shape becomes very narrow and somewhat unrealistic. In Figure 5.8 we show the projections of the NC's h_0 state (see figure 5.1) onto the corresponding bulk Bloch bands. The upper panels of Figure 5.8 show the h_0 projection for ZB NCs onto the heavy-hole (hh) and light-hole (lh) bands of bulk ZB CdSe. The lower panels of Figure 5.8 show the corresponding projection for the WZ NCs onto the WZ bulk bands, denoted as A- and B-bands [113]. All the projections are shown as a function of the aspect ratio (AR). For an aspect ratio of one in the ZB NCs (upper panels), the h_0 state has equal contributions from hh and lh, so that the square and triangles are superimposed. As stated above (see figure 5.6) the ellipticity (changing AR) leads to a splitting of the hh/lh bulk ZB bands and the NC state h_0 changes rather abruptly from being hh-like for ARs below one to being lh-like for ARs above one. This abrupt change is obvious for both sizes, 2.8 nm diameter D_h (left panels in figure 5.8, see figure 5.7 for D_h definition) and 3.6 nm D_h (right panels in figure 5.8). For the WZ structure with an AR of one, the bulk valence bands are already split by the crystal field (figure 5.1) and the NC's top of the valence band state h_0 has a dominant contribution from the bulk A-band (over 60%) and a small contribution from B-band (less than 15%). Changing the AR has a similar effect as observed for the ZB structure, i.e., we observe a transition between dominant A-band to dominant B-band h_0 states. However the transition is smooth, corresponding to an anticrossing rather than a crossing. The anticrossing point for the NCs with horizontal diameter D_h of 2.8 and 3.6 nm are 1.54 and 1.70 respectively. This result fits reasonably well

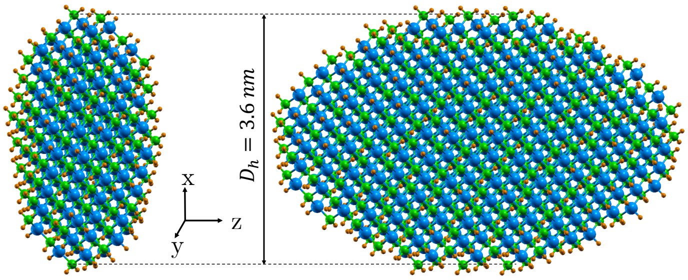

Figure 5.7: Oblate NC with an aspect ratio of 0.5 (left) and prolate NC with an aspect ratio of 1.5 (right). Cd, Se, and H atoms are rendered in blue, green, and orange, respectively.

with experimental results on the polarization factor of nanorods with diameter from 3.0 to 3.5 nm that changes rapidly from nearly zero to $\sim$ 70% when the aspect ratio increases from 1 to 2 [54].

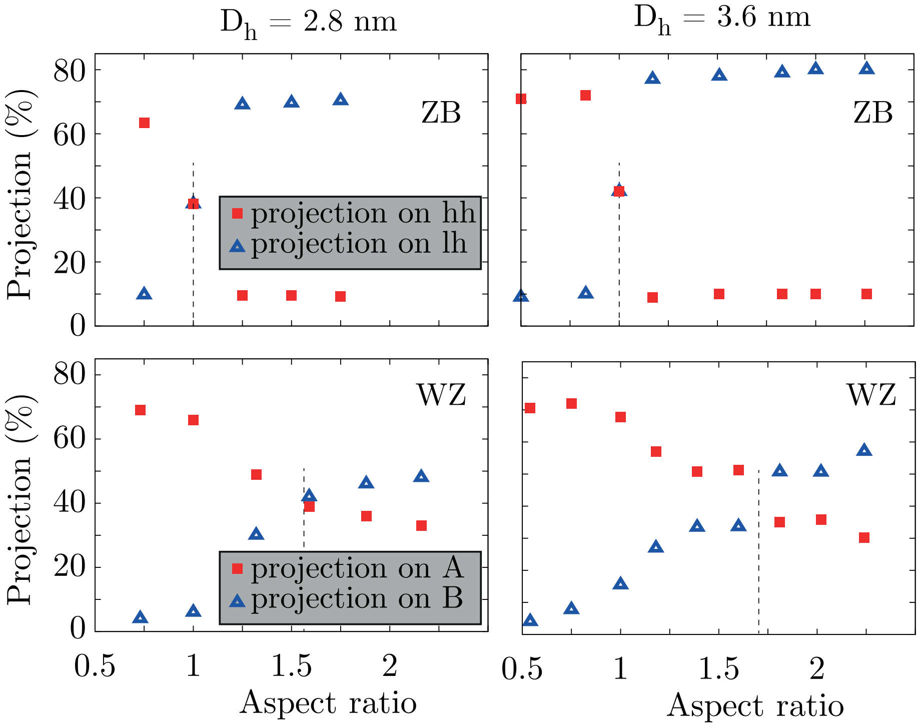

Figure 5.8: Projection of the h_0 state onto the bulk heavy hole and light hole bands for two ZB NCs with different D_h (top panels), and projection of the h_0 state onto the bulk A- and B-band for two WZ NCs with different D_h (bottom panels).

From figure 5.8 we expect a qualitative change of the ground exciton FS as a function of the AR. In Figures 5.10 and 5.11 we show the dependence of the FS on the AR for both WZ and ZB NCs, and two different sizes. For the ZB NCs with an AR of one, we obtain the results expected from the group theory analysis (figure 5.1) with a three-fold higher-energy bright state (Γ_5 in T_d point group) and a five-fold lower energy dark-state ($\Gamma_3 \oplus \Gamma_4$ in T_d point group). As already observed for the h_0 band character (figure 5.8) the change around the AR of one is rather abrupt. The excitonic states split and shift energetically. For the AR > 1 (prolate structures, C_{3v} point group) the h_0 state has Γ_4 symmetry and the h_1 state has $\Gamma_5 \oplus \Gamma_6$ symmetry (energetically in reversed order compared to figure 5.6) and the FS has a bundle of three lower energy states and two upper states. This situation is reversed when the AR < 1 for the larger structure (figure 5.11), in accordance with our hole state analysis (figure 5.8).

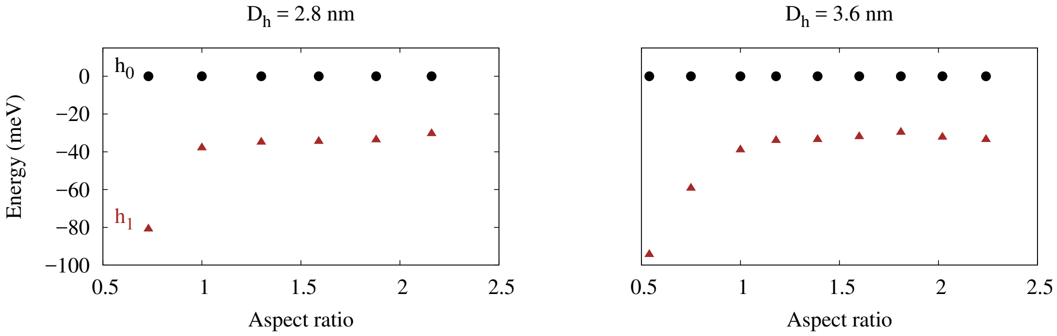

Figure 5.9: The single-particle energy of the h_0 and h_1 states (both are aligned at the h_0 energy) for two WZ NCs.

For the smaller structure in figure 5.10 this reversal is not quite complete, even at our smallest AR of 0.75 where the state 0^{L} is still energetically close to the lower energy states $\pm1^{\mathrm{L}}$ and ±2.

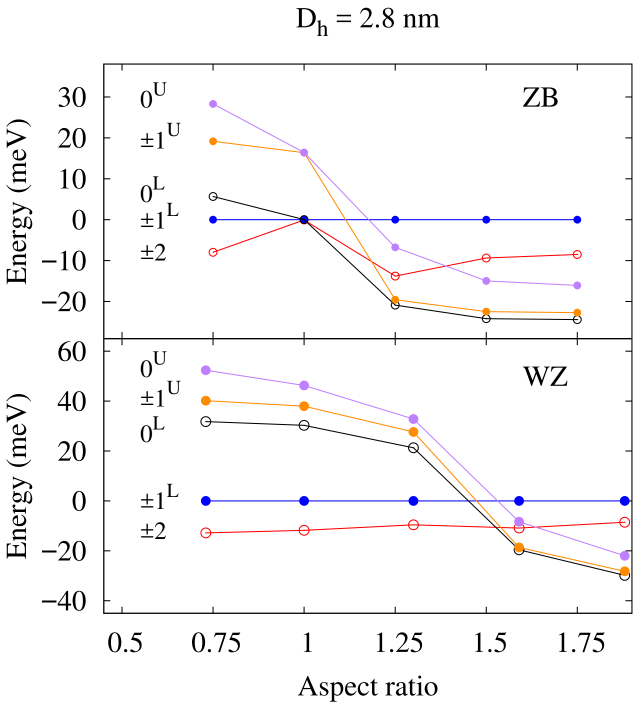

Figure 5.10: FS of ellipsoidal ZB (top) and WZ (bottom) CdSe NCs with the same horizontal diameter D$_{\mathrm{h}}$ of 2.8 nm but different vertical lengths, thus different aspect ratios. The exciton levels $\pm2, \pm1^L, 0^L, \pm1^U$ and 0^U are represented by red, blue, black, orange, and purple circles, respectively. Open circles present dark exciton states and the filled circles present the bright exciton states.

EMA predicts that the energy splitting between the h_0 and h_1 states due to the uniaxial shape distortion $\Delta_{h_0h_1}$ is governed by the ratio of the A- and B-band effective masses along the parallel direction $\beta = m_{\parallel}^{B}/m_{\parallel}^{A}$. The AEP-calculated β in this work is 0.14 which, within the EMA, leads to a constant $\Delta_{h_0 h_1}$ [33, 34] (the crystal-field splitting). The non-constant value of $\Delta_{h_0 h_1}$ shown in Figs. 5.9 points out another contradiction between atomistic and EMA results.

For the WZ NCs with $\mathrm{D_h} = 2.8$ nm (3.6 nm) with AR < 1.3 (1.6), the FS corresponds to the schematic of figure 5.1. For the larger ARs, the reversal of the h_0 and h_1 states occurs and the FS changes qualitatively: the three states originating from h_1 (see figure 5.1) are below the two states originating from h_0. These values of critical ARs fit very well with the empirical pseudopotential calculations of Ref.[115]. In loose terms we could state that the NC's elongation has overcome the intrinsic CF splitting. Of course both effects work on different length scales, the CF being an atomistic structural effect and the elongation being an overall shape effect.

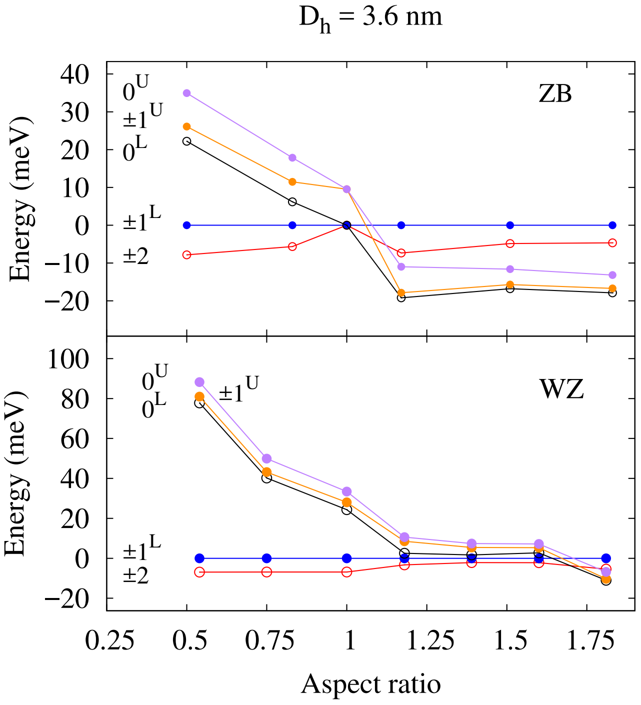

Figure 5.11: Figure corresponding to figure 5.10 but for a horizontal diameter $\mathrm{D_h}$ of 3.6 nm.

In Fig. 5.12 we calculate the FS of WZ NCs with different AR following the EMA described in reference [34] and add the long-range exchange interaction as described in reference [98]. In the EMA, the $\pm 1^U$ state denotes the state with higher (Upper) energy and the $\pm 1^L$ state the state with lower energy, regardless of their symmetry. Therefore, instead of the crossing shown in Fig. 5.10 and 5.11 we see an anticrossing between the

$\pm 1^U$ and $\pm 1^L$ states. Furthermore, the energy range of the FS is significantly different, being about a factor of three larger in the EMA. Also qualitatively, both figures differ significantly.

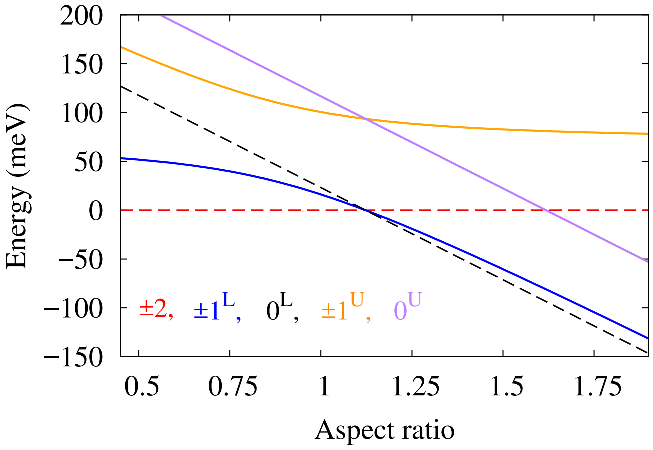

Figure 5.12: Figure corresponding to Fig. 5.10 and Fig. 5.11 but calculated using EMA for a horizontal diameter Dh of 2.8 nm.

In the next step we study the differences and the similarities between FS of WZ and ZB NCs. In figure 5.13 and 5.14 we show the calculated oscillator strength for CdSe NCs with $\mathrm{D_h} = 2.8$ nm (figure 5.13) and $\mathrm{D_h} = 3.6$ nm (figure 5.14) in the WZ and ZB structure for varying AR. The oscillator strength corresponds to a low temperature absorption measurement with high energy resolution (we use a broadening of 5 meV). Note that for a low-temperature photoluminescence experiment, the dynamics of the carriers must be taken into account and high energy states with significant oscillator strength may not emit efficiently [113]. Transitions with xy-polarization (where z is along the c-axis in WZ and along the crystallographic [001] direction in ZB) are shown in blue and with z-polarization in red. The comparison between WZ and ZB "spherical" NCs with an AR of one reveals the significant difference: for ZB NCs only one transition is optically active and is unpolarized (x,y,z components equally strong) while the WZ NCs show three optically active transitions split by as much as 50 meV. If we compare the results between ZB and WZ for the extreme cases of strongly oblate (AR ≈ 0.5 for the 3.6 nm NCs and ≈ 0.75 for the 2.8 nm NCs) or strongly prolate (AR ≈ 1.8 for both), we see a qualitatively similar FS, especially for the larger (3.6 nm) NCs. The oblate case shows a strong low energy xy-polarized transition, split from two weaker higher energy transitions with xy- and z-polarization (figure 5.14). Quantitatively the splitting between the lower energy transition and the two higher energy transitions is significantly larger for the WZ NCs (30 meV vs. 80 meV). Interestingly, the energetic position of the z-polarized transition is a good indicator of the AR. For small ARs (oblate) it is found energetically above the xy-transitions, for large ARs energetically below. We can also find very similar FS between WZ and ZB if we compare NCs with different ARs. For example, if we compare the ZB NC with AR = 0.75 with the WZ NC with AR = 1.30, for the smaller NC with $D_h = 2.8$ (figure 5.13) we see a very similar energy structure with only rather small differences in the oscillator strength of the z-polarized transition.

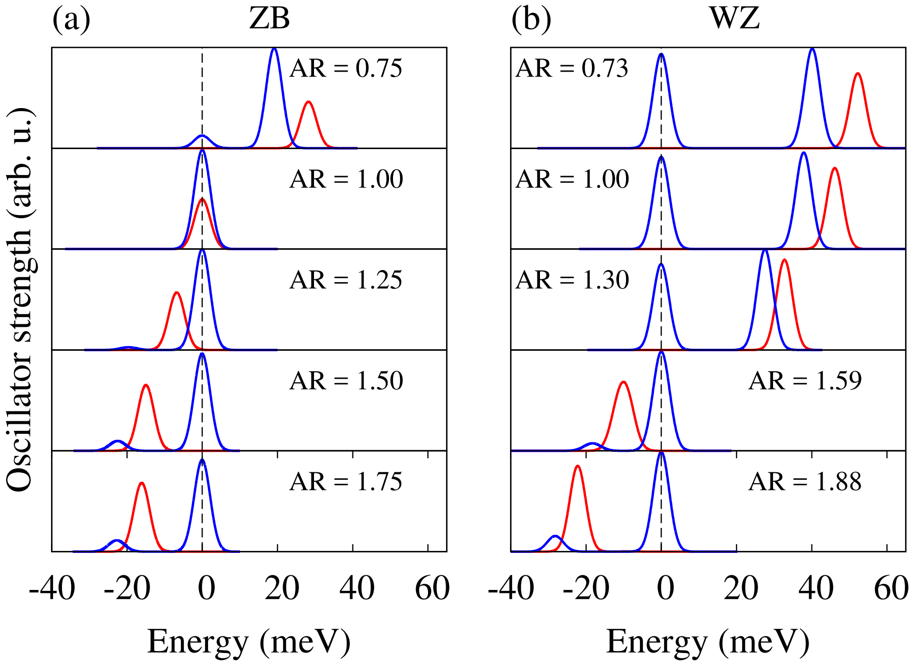

Figure 5.13: Oscillator strength of ellipsoidal (a) ZB and (b) WZ CdSe NCs with the same horizontal diameter of 2.8 nm but different vertical lengths, thus different aspect ratios. Red peaks are z-polarized (along c-axis in WZ and [001] in ZB) and blue peaks are in-plane polarized. All spectra are aligned at the $\pm 1^L$ peak which is marked by the black dashed line.

For the larger structures with $D_h = 3.6$ (figure 5.14), the FS of “spherical” WZ (AR=1) with prolate ZB with AR = 0.5 is very similar and can probably not be resolved experimentally.

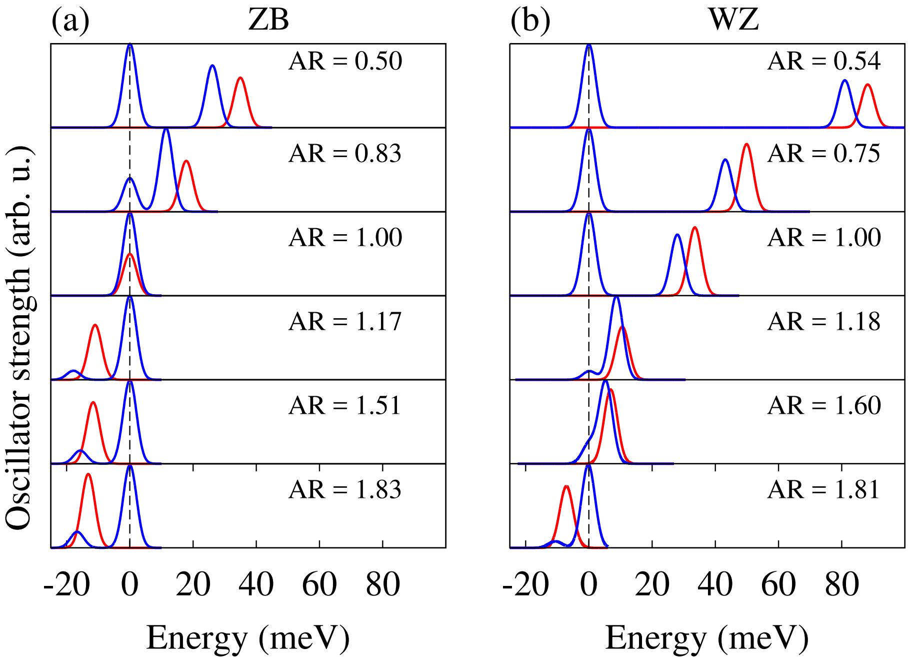

Figure 5.14: Figure corresponding to figure 5.13 but for a horizontal diameter of 3.6 nm.

5.1.3 Exciton lifetime of CdSe NCs

5.1.3.1 Experiment measurement

The Photoluminescence (PL) decay can be described by a three-level system (Figure 5.15) composed of a dark ground exciton state $|F\rangle$, a bright upper exciton state $|A\rangle$, and a zero exciton ground state $|G\rangle$ [68]. The dark-bright energy splitting is ΔE. $\Gamma_{\rm A}$ and $\Gamma_{\rm F}$ are the radiative rates of the bright and dark exciton, respectively. γ_0 is the spin-relaxation rate from bright to dark exciton state and $\gamma_{\rm th} = \gamma_0 N_{\rm B}$ is the spin-relaxation rate induced by thermal mixing of bright and dark excitons, where $N_{\rm B} = \frac{1}{exp(\frac{\Delta E}{k_{\rm B}T})-1}$ is the Bose-Einstein phonon occupation.

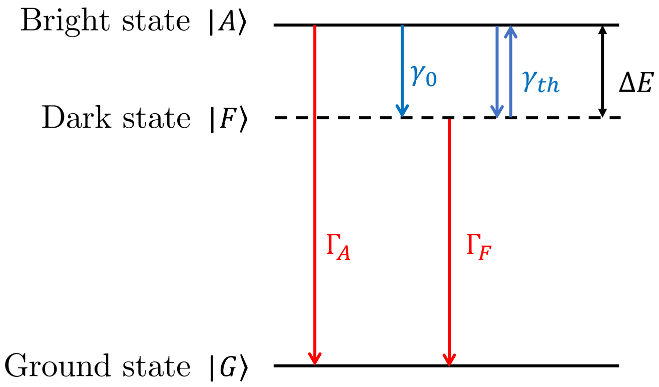

Figure 5.15: Three-level system used to interpret the data. It is composed of a zero exciton state $|G\rangle$ and two states denoted $|A\rangle$ and $|F\rangle$, corresponding to the bright and dark excitons.

The signal intensity $I(t)$ is given by:

$$I(t) = \eta_{\mathrm{A}}\rho_{\mathrm{A}}\Gamma_{\mathrm{A}} + \eta_{\mathrm{F}}\rho_{\mathrm{F}}\Gamma_{\mathrm{F}} \tag{5.1}$$

Here, η_i is the quantum yield, ρ_i is the time-dependent population, and Γ_i is the radiative rate of the state i. The spectrally filtered PL decay can be fitted by biexponential decay with characteristic times τ_{short} and τ_{long} as shown in figure 5.16 [11].

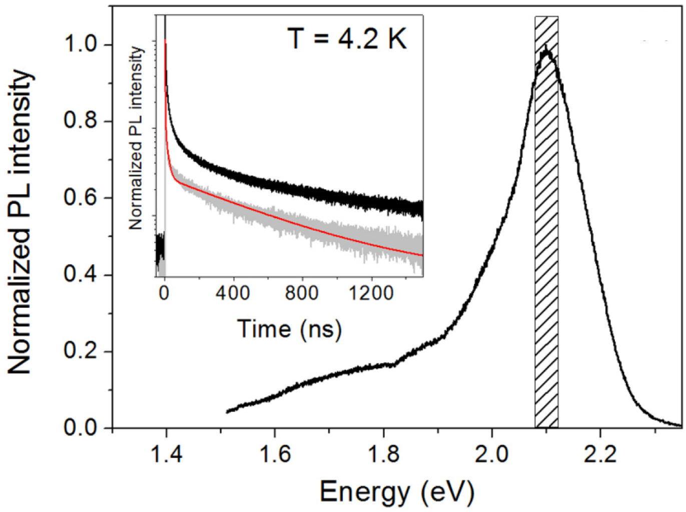

Figure 5.16: Time-integrated PL spectrum of InP/ZnS nano particle, with 2.9 nm core and 2-nm thick shell. Inset: Spectrally integrated PL decay (black) and spectrally filtered PL decay (gray) fitted by biexponential decay (red line) with characteristic times $\tau_{\mathrm{short}} = 1.5$ ns and $\tau_{\mathrm{long}} = 430$ ns.

Assuming that the thermalisation between the bright and the dark states is very fast ($\gamma_0 \gg \Gamma_\mathrm{A}$) and the quantum yield of both the bright and dark excitons is 1 [15], we have:

$$I(t) = A_\mathrm{L}e^{-\Gamma_\mathrm{L}t} + A_\mathrm{S}e^{-\Gamma_\mathrm{S}t} = \frac{\Gamma_\mathrm{A}N_\mathrm{B} + \Gamma_\mathrm{F}}{1+2N_\mathrm{B}}e^{-\Gamma_\mathrm{L}t} + \Gamma_\mathrm{A}\Big[\rho_\mathrm{A}(0) - \frac{N_\mathrm{B}}{1+2N_\mathrm{B}}\Big]e^{-\Gamma_\mathrm{S}t}, \quad (5.2)$$

with $\rho_\mathrm{A}(0)$ the population of the bright state after the nonresonant excitation. A_L and A_S are the normalized amplitudes, Γ_L and Γ_S are the decay rates of the long and the short component of PL decay, respectively. Γ_L and Γ_S are functions of the bright and dark exciton radiative rates Γ_A and Γ_F.

$$\Gamma_\mathrm{L} = \frac{\Gamma_\mathrm{A} + \Gamma_\mathrm{F}}{2} - \frac{\Gamma_\mathrm{A} - \Gamma_\mathrm{F}}{2}tanh\Big(\frac{\Delta E}{2k_\mathrm{B}T}\Big) \quad (5.3)$$

$$\Gamma_\mathrm{S} = \gamma_0(1 + 2N_\mathrm{B}) \quad (5.4)$$

At very low temperatures: $k_\mathrm{B}T \ll \Delta E$, $tanh\Big(\frac{\Delta E}{2k_\mathrm{B}T}\Big) \to 1$, $N_\mathrm{B} = \frac{1}{exp(\frac{\Delta E}{k_\mathrm{B}T})-1} \to 0$, hence:

$$(5.3) \Leftrightarrow \Gamma_\mathrm{L} = \Gamma_\mathrm{F}$$
$$(5.4) \Leftrightarrow \Gamma_\mathrm{S} = \gamma_0.$$

Therefore, the dark exciton radiative rate and the bright-to-dark spin-flip rates can be obtained directly from the bi-exponential decay at low temperatures.

At high temperatures: $k_\mathrm{B}T \gg \Delta E$, $tanh\Big(\frac{\Delta E}{2k_\mathrm{B}T}\Big) \to 0$, $N_\mathrm{B} = \frac{1}{exp(\frac{\Delta E}{k_\mathrm{B}T})-1} \to \infty$ and note that $\Gamma_\mathrm{A} \gg \Gamma_\mathrm{F}$, we have:

$$\Gamma_\mathrm{L} = \Gamma_\mathrm{A}/2 \quad (5.5)$$

$\Gamma_\mathrm{S} \to \infty$ and the second term in the equation (5.2) vanishes.

The dark-bright splitting ΔE can be derived from Γ_A and Γ_F by using the equation (5.3). Besides, ΔE can also be obtained from the normalised amplitude of the biexponential decay, since $A_\mathrm{S} = A_\mathrm{L} = 0.5$ for $k_\mathrm{B}T = \Delta E$ [11].

5.1.3.2 Theoretical calculation

The radiative lifetime for the transition from the initial excitonic state Ψ_i to the final excitonic state Ψ_f is defined by standard perturbation theory [31]:

$$\frac{1}{\tau_{if}} = \frac{4nF^2\alpha\omega_{if}^3}{3c^2}|M_{if}|^2. \tag{5.6}$$

Where n is the refractive index of the surrounding medium, F is the screening factor and defined as $F = 3\epsilon/(\epsilon_{QD} + 2\epsilon)$ with $\epsilon = n^2$ and ϵ_{QD} is the dielectric constant of the nanocrystal, α is the fine structure constant, $\hbar\omega_{if}$ is the transition energy, c is the speed of light in vacuum and $|M_{if}|$ is the CI dipole matrix element [20]. We are studying single excitation, hence $|M_{if}|$ is given as

$$M_{if} = \sum_{\mathrm{h,e}} C^{*(i)}_{\mathrm{h,e}} C^{(f)}_{\mathrm{h,e}} \langle \psi_{\mathrm{h}} | r | \psi_{\mathrm{e}} \rangle. \tag{5.7}$$

Where ψ_{h} and ψ_{e} are the single-particle wavefunctions of the valence and conduction states obtained from the Ab-initio calculation and included in the CI expansion. $C^{(i)}_{\mathrm{h,e}}, C^{(f)}_{\mathrm{h,e}}$ are the coefficients of the CI expansion of the initial and final states, respectively.

In our study, $\langle \psi_{\mathrm{h}} | r | \psi_{\mathrm{e}} \rangle$ and M_{if} are calculated within the mxmat code and the mxdipole code, respectively. τ_{if} is calculated from equation (5.6), the calculation is implemented in the oscitau code.

5.1.3.3 Results

In our simulation, the semiconductor quantum dot is terminated by hydrogen or pseudo hydrogen in order to remove all surface states that originated from dangling bonds. In experiment, the semiconductor nanocrystals can be coated by other semiconductors [11, 58, 77, 97, 108]; inorganic molecules or organic ligands [28, 29, 80]. Both our calculation and experimental results show that the exciton ground state is optically inactive (dark exciton $|F\rangle$) and right above this state is the bright exciton state $|A\rangle$. Though the transition from and to the dark exciton state is optically inactive it can be prompted by phonon-assisted processes. At low temperature, these processes are very slow compared to the direct optical transition leading to a long-lived exciton state. As mentioned earlier, at high temperature, because of the thermal population of the higher energy bright states, the exciton lifetime is shortened rapidity and has the value of twice the lifetime of the bright exciton $|A\rangle$ (see equation (5.5)). It is shown experimentally and theoretically that an external magnetic field [86], [60] and surface states [19], induce the mixing between the dark and the bright states, hence enhance the dark exciton decay rate and reduce the bright exciton decay rate.

Figure 5.17 shows the calculated bright exciton lifetime of CdSe NCs in comparison with experimental results which is determined at room temperature.

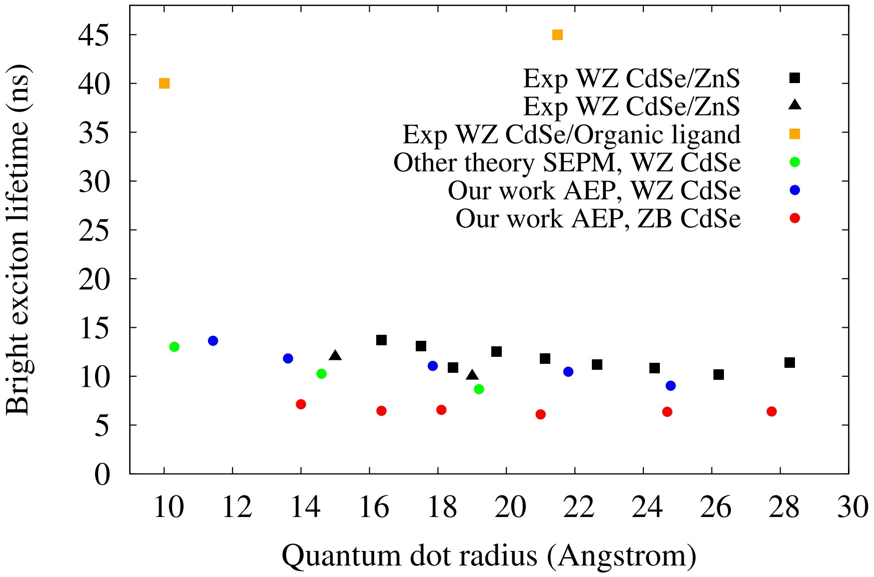

Figure 5.17: The calculated radiative lifetime of the bright exciton of the WZ CdSe QDs in comparison with experimental results. Black square and triangle present experimental results of WZ CdSe/ZnS NCs in ref.[58] and ref.[68], respectively. Orange square shows the measurement of WZ CdSe NCs coated by organic ligand in ref.[28]. Green circle is the result obtained by the SEMP method [20]. Blue and red circles are AEP results for WZ and ZB CdSe NCs. AEP results are in good agreement with SEPM and experimental results of core-shell nanoparticles but significantly different from the QDs coated by organic ligands.

The refractive index of toluene $n = 1.496$ is used in our calculations. Our results are in good agreement with experimental results of core-shell nanoparticles but significantly different from the results for the QDs coated by organic ligands. It is because the core-shell systems are usually quite clean in the interface and introduce much fewer defect states compare to systems with organic ligands.

To model the effect of defect states on the exciton lifetime, we remove one passivant of an anion atom. This removal causes surface states that are located in the band gap. The surface states lead to the mixing of the bright and the dark states which makes the lifetime of the bright exciton a bit longer and the lifetime of the dark exciton thousands time shorter.

5.1.4 Conclusion

We calculate the FS of colloidal CdSe QDs based on atomistic pseudopotentials and configuration interaction theory and compare the results to recent theoretical predictions based on EMA models and reveal qualitative deficiencies of the latter approach. This calls for a new parametrization of the EMA and expresses a more general warning about the use of continuum descriptions for small nanostructures. Especially the FS, which has its origin in the atomistic nature may be especially challenging to model based on a continuum description. Our results are in very good agreement with experiment. We further use our methodology to compare the FS of WZ and ZB NCs of different sizes and especially with different aspect ratios. We pinpoint similarities between both FSs when the structures are either both (WZ, ZB) strongly oblate or both strongly prolate. We also find very similar FS if we compare a ZB NC with AR $= 0.75$ with a WZ NC with AR 1.3. We rationalize these results by a discussion of the orbital character of the hole states that contributes to the exciton: The deviation from spherical shape (oblate or prolate) has a similar effect on the splitting of the valence bands as the intrinsic crystal field splitting in the WZ structure. Consequently an oblate ZB NC can exhibit a similar top of the valence band state h_0 to a “spherical” WZ NC, and hence a similar FS. However, the FS of “spherical” ZB and WZ NCs of similar sizes are significantly different. We further show that the z-polarized transition may be used as an indicator for the AR. About the exciton lifetime, though ZB and WZ CdSe spherical NCs have completely different FS, they appear to have similar bright exciton lifetime. Additionally, the exciton lifetime is strongly affected by the ligand or surrounding medium.

5.2 Excitonic fine structure of InP nanocrystals

Due to the ease in synthesis and the applicable optical properties, over past decades, Cd containing NCs have been extensively studied both theoretically and experimentally, results in an insight into electronic and optical properties of Cd-based NCs. They are promising for many fields of applications; however, the high toxicity of Cd-based materials is still challenging. As an alternative, InP NCs have comparable optical properties with Cd-based NCs, and importantly InP has less toxicity. InP had not been attractive before because InP NCs synthesis protocols were more challenging to implement due to the use of an expensive and highly pyrophoric phosphorus precursor [6, 71, 79]. Recently, new synthesis protocols based on a cheap and easy-to-use phosphorus precursor that leads to high-quality InP NCs have been published [11, 100, 105]. These protocols facilitate the production of InP NCs and should lead to more optical studies by enabling more easy access to high-quality materials [11]. Experimental studies reveal a Stokes shift in the range of several meV between absorption and emission spectra of InP NCs. At low temperature, the photoluminescence stems from the thermal mixing between the lowest dark and bright excitonic states. The temperature dependence of photoluminescence spectra shows a bi-exponential decay enable for the calculation of the bright and dark exciton lifetime [11, 80]. Empirical pseudopotential calculations of the dark-bright splitting and exciton energy of InP NCs show good agreement with the experiment [38].

5.2.1 CI convergence

As shown in figure 5.1, in ZB NCs, HOMO is four-fold degenerate and LUMO is two-fold degenerate with spin-orbit coupling is taken into account. Therefore, without electron-hole interaction, the first exciton level is eight-fold degenerate. In the presence of electron-hole interaction, the lowest-energy electron with angular momentum $J_e = \frac{1}{2}$ and the highest-energy hole with angular momentum $J_h = \frac{3}{2}$ can not be considered separately but should be treated as a combined exchange-correlated exciton with a total angular momentum J of 1 or 2 results in the two levels of exciton. One is three-fold and bright, corresponds to $J = 1$ and the other one is five-fold and dark, corresponds to $J = 2$.

In the configuration-interaction calculations, the interaction between different configurations and hence, the correlation effect is included. If the basis set is complete, then the correlation energy is exact. In practice, we use the basis set that is sufficient to obtain useful results with reasonable effort, and what we get is then the correlation energy of the given basis set. The convergence of the CI expansion with respect to the size of the basis is presented in figure 5.18. As shown in figure 5.18, the convergence of the lowest exciton levels is quite slow, while the convergence of the exchange splittings is relatively fast. For this 16 nm in radius InP quantum dot, with the basis set of $N_\mathrm{v} = 10$ and $N_\mathrm{c} = 4$ our calculated exchange splitting is converged within 0.5 meV.

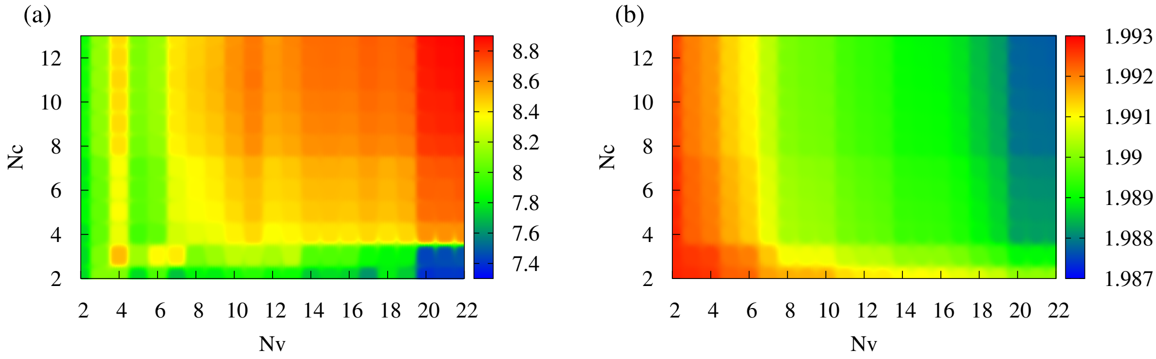

Figure 5.18: The convergence of (a) the DB splitting, (b) the first bright exciton energy with the number of valence-band states N_v and conduction-band states N_c (not including spin) of the InP quantum dot with $D = 3.2$ nm.

5.2.2 Excitonic fine structure of spherical InP NCs

Experimentally, the DB splitting of NCs can be determined from either Fluorescence Line-Narrowing (FLN) spectra [34] or the temperature dependence of the Photoluminescence (PL) decay [11]. In the first method, the first peak of FLN is attributed to the Zero Phonon Line (ZPL) from the dark state, so its shift from the laser was taken as a reference for the dark-bright splitting. In the second method, from the temperature dependence of the PL decay, the dark exciton lifetime Γ_F and the bright exciton lifetime Γ_A are calculated at low and high-temperature limitation and used as parameters to determine Δ_DB. For CdSe NCs, both methods produce similar values of Δ_DB. For InP NCs, however, FLN spectra derive larger Δ_DB compared to the other one. This discrepancy between two methods in InP NCs can be explained by attributing the first FLN peak to acoustic phonon sideband instead of ZPL [14]. Figure 5.19b shows a good comparison between our calculated and experimentally measured DB splitting of spherical InP NCs. Figure 5.19a shows our results on the diagonal Coulomb integrals between the first lowest unoccupied and the highest occupied states in comparison with the EMP method in ref. [38]. The effect of electron-hole Coulomb interaction is to lower the exciton energy levels several hundreds of meV.

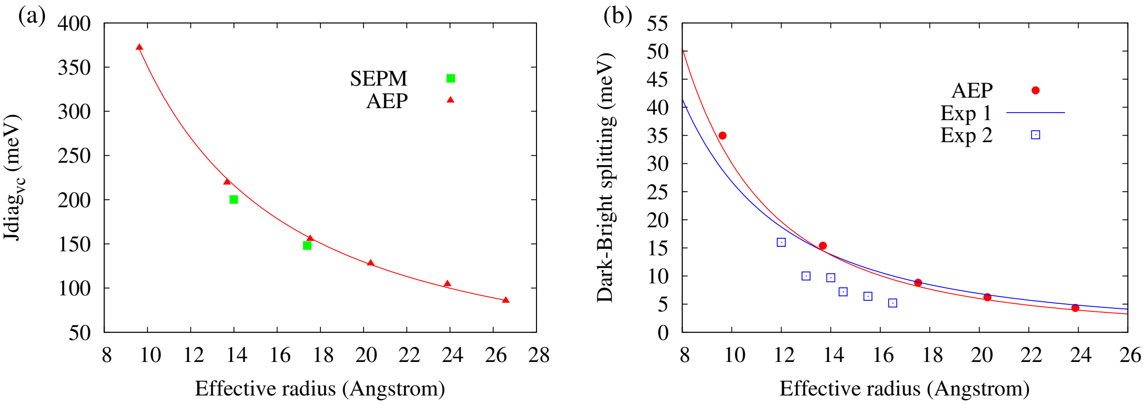

Figure 5.19: (a) The diagonal Coulomb integral between the lowest conduction state and the highest valence state of InP quantum dots. (b) The DB splitting of InP quantum dots. Exp 1, 2 are experimental results extracted from Ref. [78] and [11], respectively.

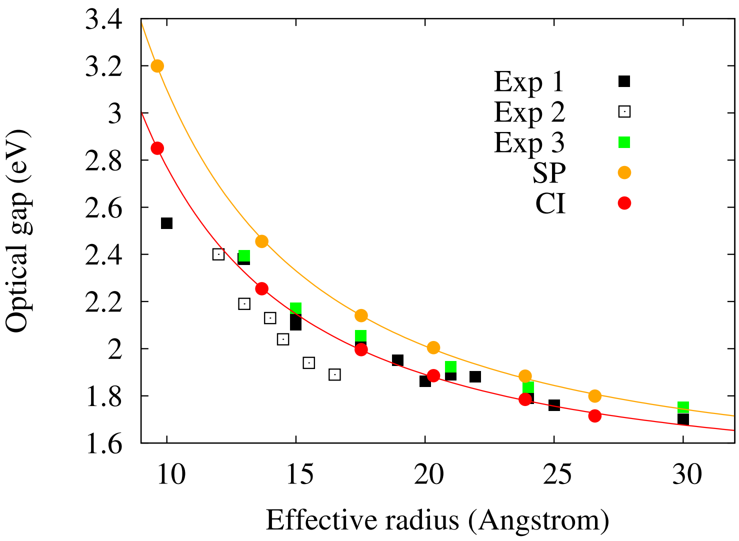

Figure 5.20: The first bright exciton energy of spherical InP quantum dots, experiment values are taken from refs. [11, 79, 80], respectively.

We calculate the optical gaps of NCs, taking into account electron-hole interactions and correction effect. Our results reproduce very well experimental data (see figure 5.20). The correlation energy of quantum dots with our chosen basis set is from several meV to few tens of meV, which is small and negligible. The difference in energy between SP and CI calculation is exciton binding energy. The exciton binding energy of spherical

InP NCs increases from 84 meV to 350 meV when the radius of NC decreases from 26.6 Å to 9.6 Å.

5.2.3 Conclusion

We calculate the Coulomb, exchange, correlation interaction, and the band-edge exciton energy of spherical InP NCs, providing an insight into the optical properties of spherical InP NCs. The Coulomb interaction between electrons and holes lowers the exciton energy several hundreds of meV. The exchange interaction split the band-edge exciton into 5-fold degenerate dark states and 3-fold degenerate bright states. The DB splitting is from several meV to tens of meV and decreases when the size of NC increases. In the confinement regime, the correlation effect is small and can be neglected. The good agreement between our results and experimental measurements indicates the efficiency of our method.

5.3 Excitonic fine structure of HgTe nanocrystals

Since the last decade HgTe colloidal NCs detectors with mechanical flexibility, wide spectral sensing range, fast response, and high detectivity have been extensively investigated [104]. The optical band gap of HgTe NCs in the range of near-infrared and mid-infrared is promising for infrared imaging technology [70]. Many experimental measurements have been performed to gain insight into the optical properties of HgTe nanocrystals[2, 47, 62, 63, 67, 72, 96, 99, 104], however, the theoretical study on HgTe nanocrystals is still limited. There have been several theoretical studies using the tight-binding model [3], [63], in which the exciton energy and absorption spectra of spherical QDs [3] and tetrahedral QDs with round tips [63] are calculated. In this work, we study the optical properties of HgTe QDs using the AEP method, and obtain a good agreement for the exciton energy with experiments. Besides, we investigate the fine structure of the spherical HgTe NCs and absorption spectra of exciton and trion that can be useful for experiment measurements in the future.

5.3.1 Electronic properties of HgTe nanocrystals

In figure 5.21b the eigenvalues around the HOMO and LUMO of a 3.8 nm in diameter NCs are presented together with the states symmetry. By analyzing the symmetry of wavefunctions, we figure out that HOMO has Γ_8 symmetry and LUMO has Γ_6 symmetry. This result implies that HOMO mostly originates from Γ_8 bands while LUMO is primarily from the Γ_6 bands. It should be noted that the double group is needed to analyse the symmetry of the wavefunction in the presence of spin-orbit coupling. Therefore the representations of T_d point group in this analysis are different from that of the analysis in figure 2.15 of chapter 2 where the spin-orbit coupling is ignored. The HOMO and LUMO wavefunctions are shown in the inset of figure 5.21b to be confined nicely inside the quantum dot.

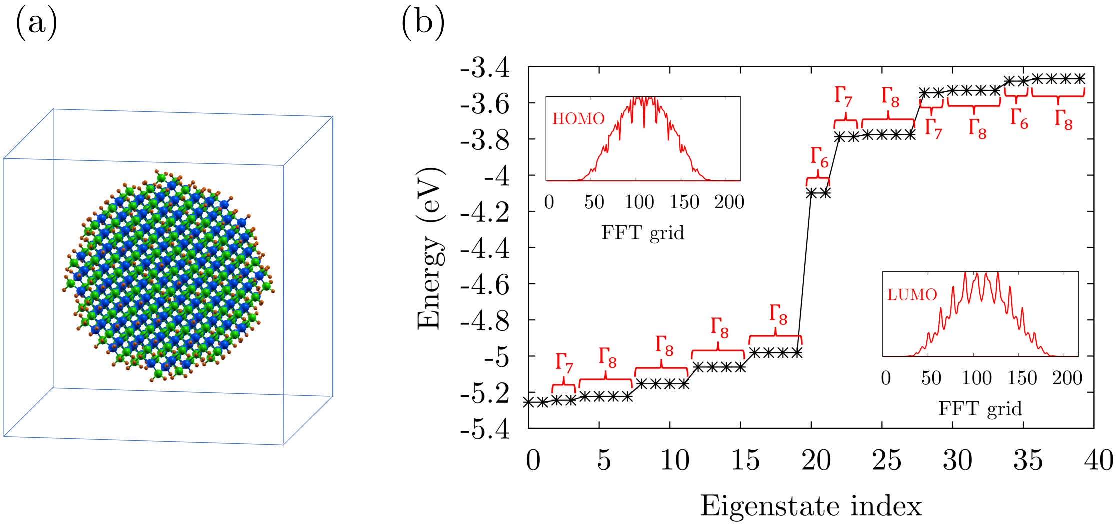

Figure 5.21: (a) A spherical HgTe NC with a diameter of 3.8 nm. (b) Eigenvalues of this quantum dot, HOMO's and LUMO's index is 20 and 21, respectively. HOMO is four-fold degenerate while LUMO is two-fold degenerate. The 1D plot of HOMO (e_0) and LUMO (h_0) wavefunctions indicating they are nicely confined inside the quantum dot. The symmetry of each states are shown.

Fig.5.22 shows the projection of the HOMO and LUMO wavefunctions onto the Γ_6 and Γ_8 bands of HgTe bulk. The results again indicate that the HOMO of HgTe NCs originates mostly from the Γ_8 band (above 60%) and the LUMO has dominant component from the Γ_6 band (above 50%). The crossing between the Γ_6 and Γ_8 levels can be explained by the molecular orbital theory, depicted in figure 5.23.

Figure 5.24 presents eigenvalues of HgTe and CdSe NCs with different sizes. Compared to the CdSe NCs, the HgTe NCs have smaller SP gaps. The gap of CdSe NCs increases from 2.1 eV to 2.6 eV as the QD diameter decreases from 5.6 nm to 2.8 nm. The gap of HgTe NCs increases from 0.4 eV to 1.1 eV as the QD diameter decreases from 6.9 nm to 2.5 nm.

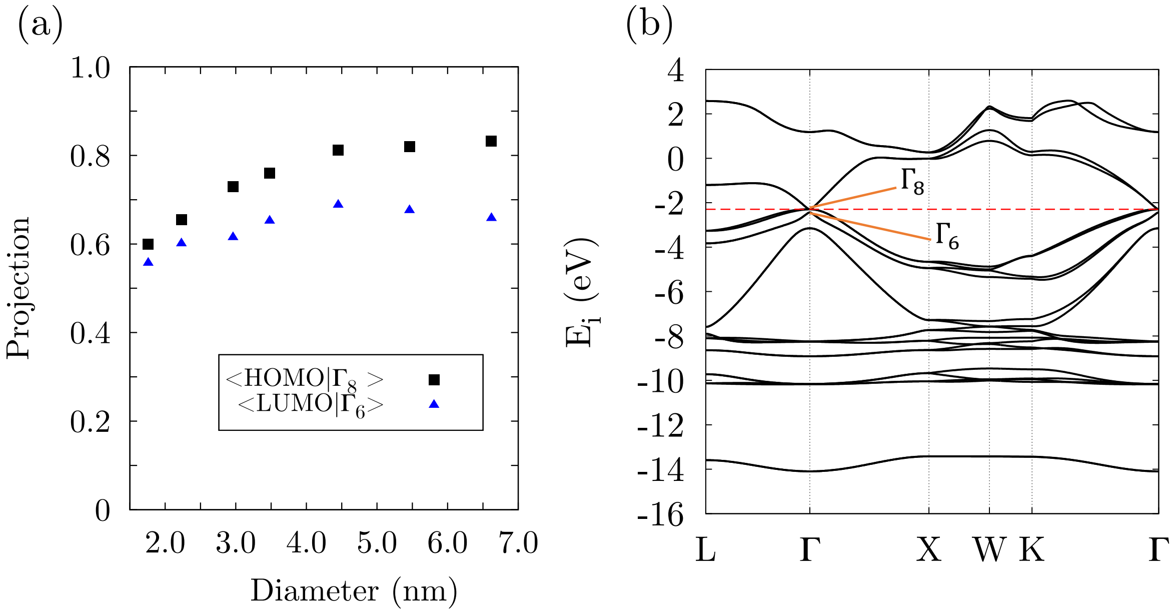

Figure 5.22: (a) Projection of HOMO and LUMO wavefunctions of HgTe NCs onto the wavefunctions of the bulk system. The results show that HOMO wavefunction of QDs is mostly from heavy hole and light hole (Γ_8) bands while LUMO wavefunction is mainly originated from the Γ_6 band. (b) Band structure of HgTe bulk.

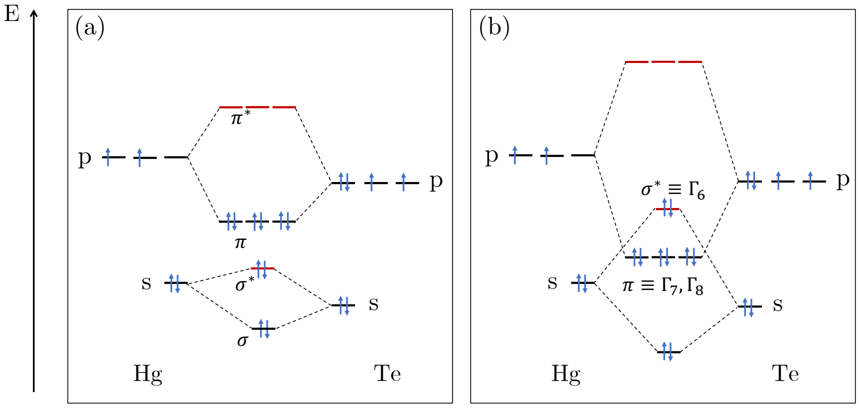

Figure 5.23: Molecular orbital diagram of HgTe. (a) In bulk, the lowest unoccupied (anti-bonding π^*) and the highest occupied (bonding π) states have p states character. (b) In NCs, under the confinement effect, the bonding and anti-bonding of s and p channels split, resulting in the crossing between the anti-bonding state σ^* of the s and the bonding states π and σ of the p channels. Therefore in NCs, the lowest unoccupied state is σ^* and has s character.

5.3.2 Optical properties of HgTe nanocrystals

The convergence of the CI expansion with respect to the size of the basis of HgTe NC with the diameter of 3.8 nm is presented in figure 5.25. As shown in figure 5.25, with

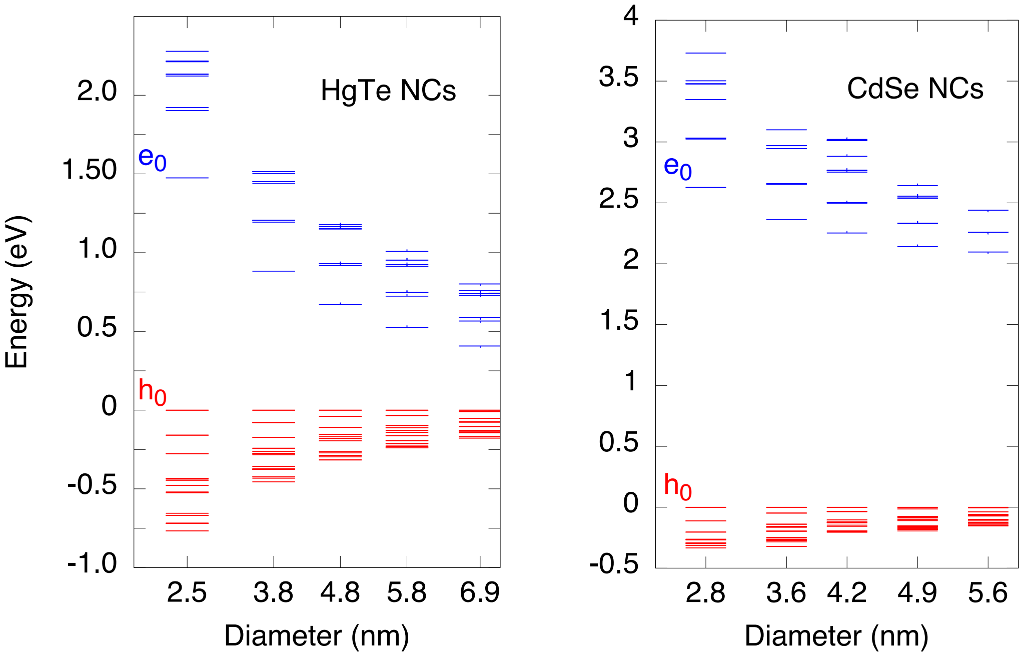

Figure 5.24: Energy levels of HgTe and CdSe NCs with different sizes.

the basis set of $N_{\rm v} = 14$ and $N_{\rm c} = 8$ the calculated DB splitting is converged within 0.04 meV and exciton energy is converged within 0.3 meV

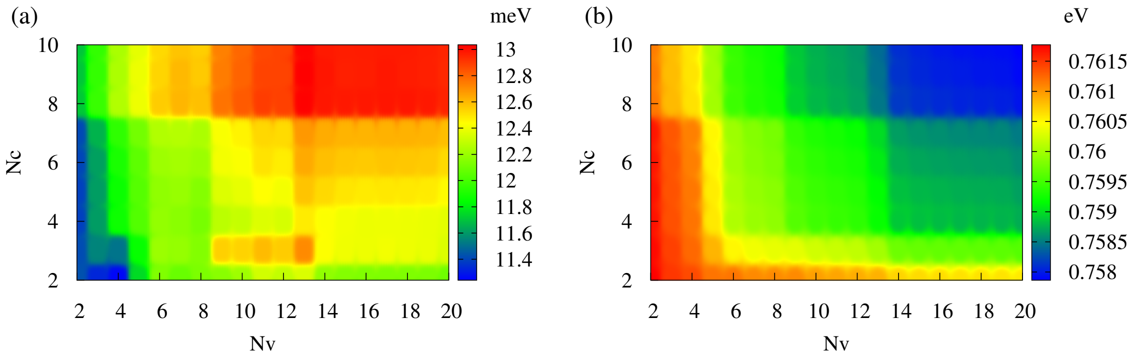

Figure 5.25: The convergence of (a) the DB splitting, (b) the first bright exciton energy with the number of valence-band states $N_{\rm v}$ and conduction-band states N_c (not including spin) included in the CI expansion of the HgTe quantum dot with $D = 3.8$ nm.

Figure 5.26 represents the Coulomb integral between the lowest electron state and the highest hole state and the DB splitting (exchange splitting) of HgTe NCs in comparison to CdSe NCs. The Coulomb integrals in HgTe NC are several tens of meV smaller than in CdSe NC with the same size, while the exchange splitting in HgTe NCs is slightly larger than in CdSe NCs.

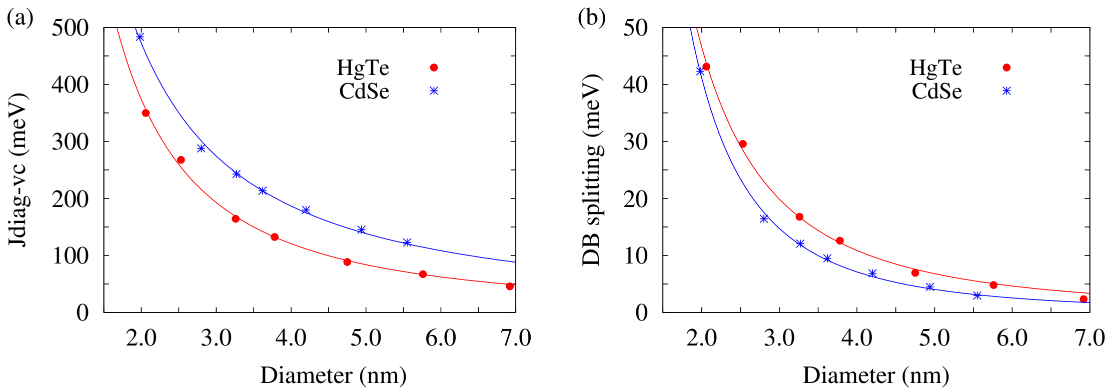

Figure 5.26: (a) The diagonal Coulomb integral between the highest valence sate and the lowest conduction state, (b) The DB splitting of HgTe and CdSe QDs.

The single-particle (SP) and the optical (CI) gap of HgTe NCs with different sizes are shown in figure 5.27. The difference in energy between SP and CI gap is the exciton binding energy, the exciton binding energy of HgTe NCs increases from 45 meV to 320 meV when the NC size decreases from 6.9 nm to 2.5 nm.

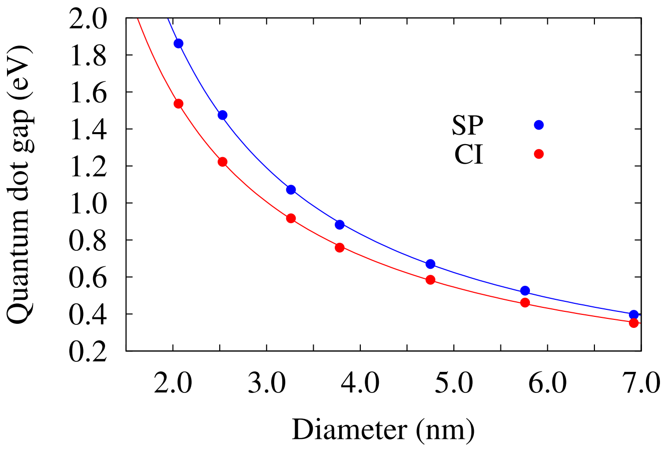

Figure 5.27: The single particle (SP) and the optical (CI) gap of HgTe NCs for various sizes.

We compare the AEP calculated exciton wavelength with some experimental measurements in figure 5.28 . HgTe NCs in the experiment can have nearly spherical shape [99], tetrahedron shape [70], [63] or tetrahedron shape with round tips [63]. However, the AEP and CI calculations are properly done for only spherical shapes. The results of tetrahedron shape and tetrahedron shape with round tips are derived from the result of the spherical shape structure by equating the volume of the spherical NCs to the tetrahedron or the tetrahedron with round tips to calculate their corresponding effective diameter. Our results are in a very good agreement with experimental results for all types of NC shapes.

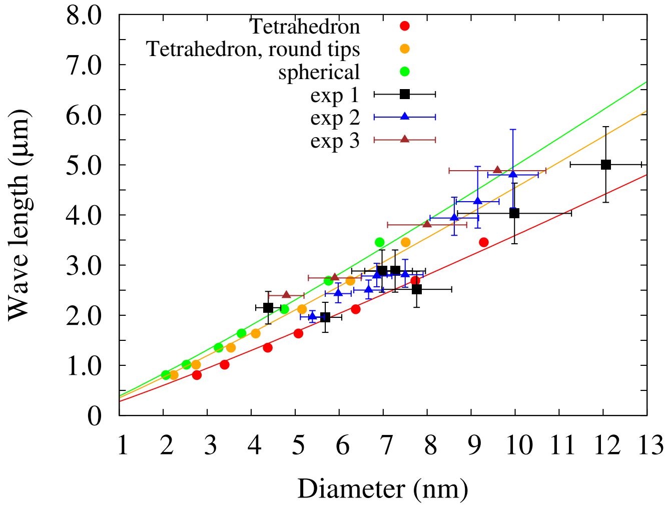

Figure 5.28: Exciton energy measured by various groups in comparison with our calculations. Experiment: Black squares show exciton energy of QDs in various shapes including spherical, tetrahedron, multipods [70]. Blue triangles represent exciton energy for tetrahedron QDs at small size and tetrahedron with round tips QDs at bigger size [63]. Brown triangles are exciton energy of nearly spherical QDs [99]. Theory: Green filled circles are our calculations for spherical QDs, orange and red filled circles are our results using the adjustment from spherical to tetrahedron with round tips and regular tetrahedron QDs, respectively.

In figure 5.29, we compare the AEP calculated exciton wavelength with the results of tight-binding (TB). The exciton wavelength of the tetrahedron with round tips obtained by TB is about 0.5 μm smaller than the AEP result. The AEP result fits better to experiment for the three largest NCs, which are claimed to have tetrahedron with round tips shapes [63]. For spherical NCs, AEP result also shows a better agreement with the experiment compared to the TB result.

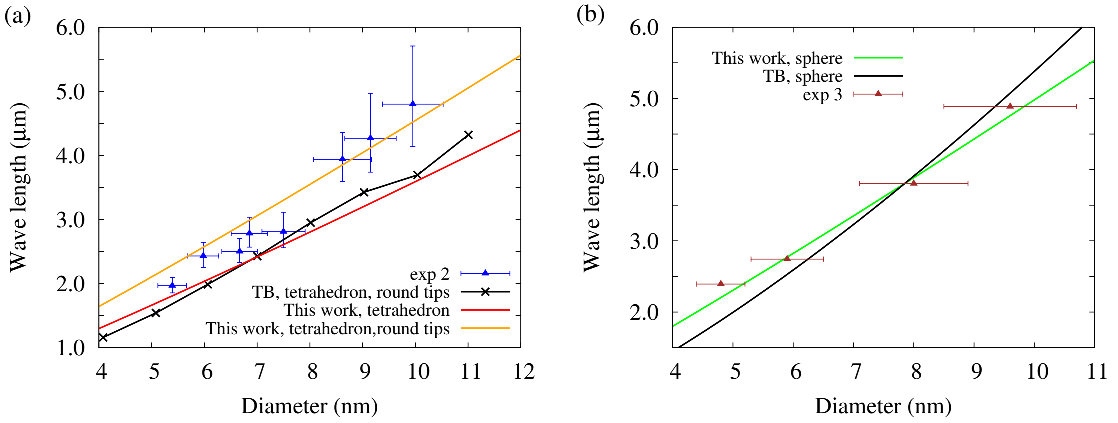

Figure 5.29: Comparison between our model and TB. (a) Exciton energy for tetrahedron with round tips QDs: orange and red curves are fitting curves to our calculation for tetrahedron with round tips and regular tetrahedron QDs, respectively. The black crosses and curve show the TB result for tetrahedron with round tips QD [63]. Blue triangles are experimental measurement for tetrahedron QDs at small size and tetrahedron with round tips at bigger size [63]. (b) Exciton energy for spherical QDs: Green curve is fitting curve to our calculation for spherical QDs, black curve is TB result for spherical QDs [3] and brown triangles are experimental results for nearly spherical QDs [99].

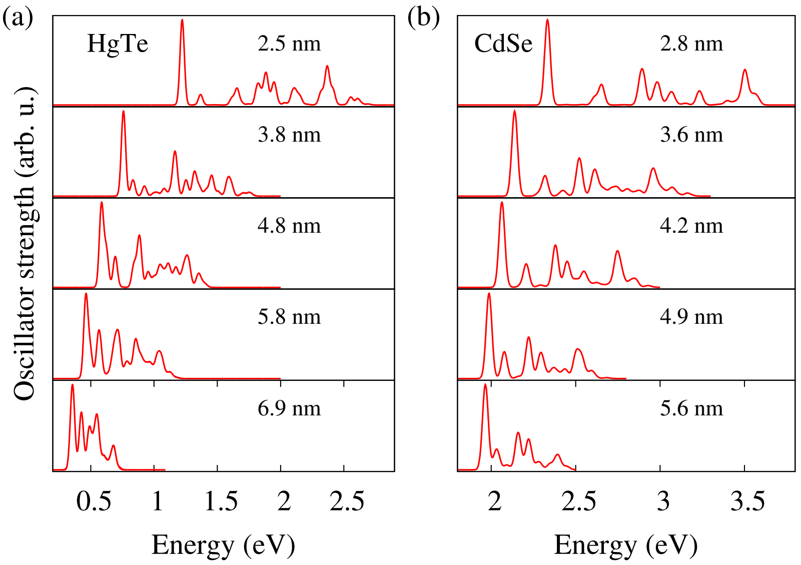

Figure 5.30: Absorption spectra of (a) HgTe and (b) CdSe NCs with different diameters.

Figure 5.30 shows the absorption spectra of HgTe and CdSe NCs with different sizes. In both HgTe and CdSe NCs peaks of the absorption spectra are more clearly resolved in smaller NCs. The absorption spectra require large enough basis sets to be described appropriately. The dependence on the basis set of the absorption spectrum of D = 5.8 nm HgTe NC is represented in figure 5.31. The high-energy peaks stem from deeper hole states and higher electron states, therefore more hole and electron states are needed in the basis set. With a small basis set, only low-energy peaks are described. The origin of the absorption peaks are shown in detail in 5.32.

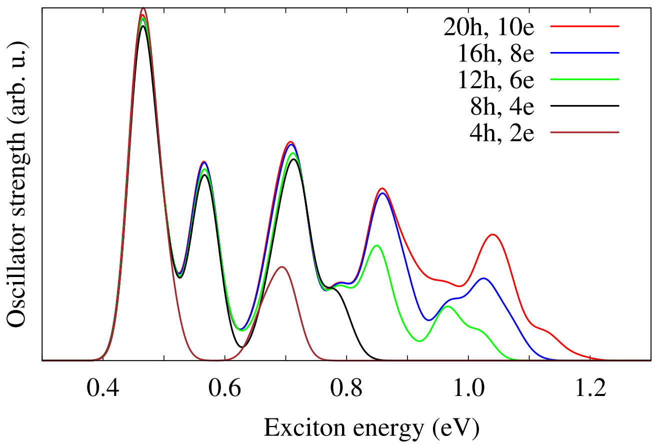

Figure 5.31: Dependence of the absorption spectra of the D = 5.8 nm HgTe NCs on the basis set.

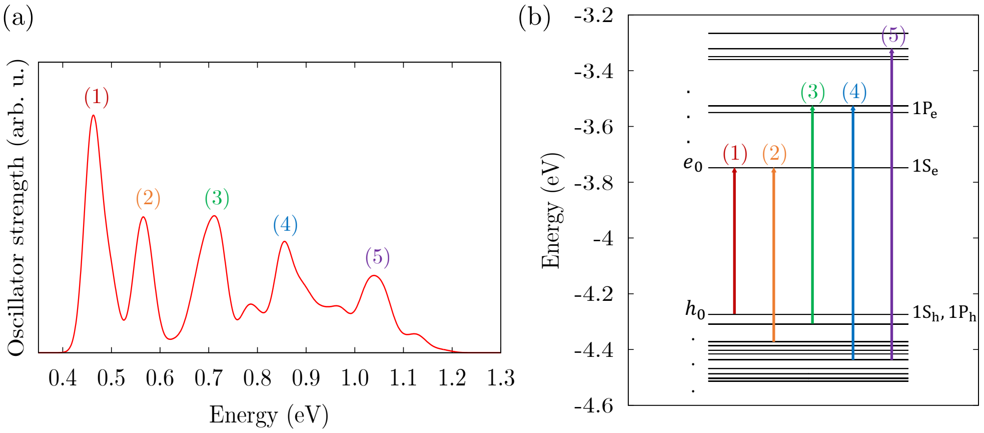

Figure 5.32: Analyzing the origin of 5 resolved peaks in the absorption spectra of the D = 5.8 HgTe NCs.

We investigate the band-edge negative trion of HgTe and CdSe NCs, figure 5.33 represents the first negative trion and the first exciton peaks of HgTe and CdSe. The difference in energy between the negative trion peak and the exciton peak is almost double in CdSe compare to HgTe NCs. Figure 5.34 shows the splitting between the negative trion and the exciton peak with respect to the NCs sizes.

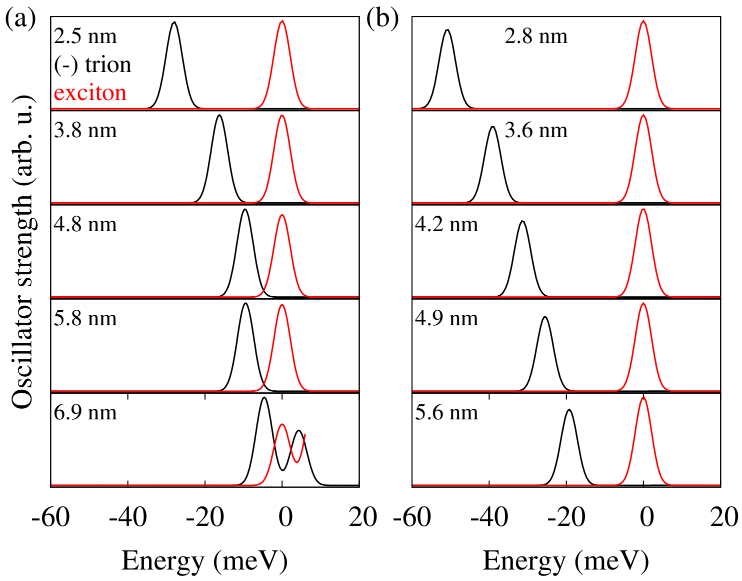

Figure 5.33: Band-edge exciton and trion (-) peaks of (a) HgTe and (b) CdSe NCs at different diameters.

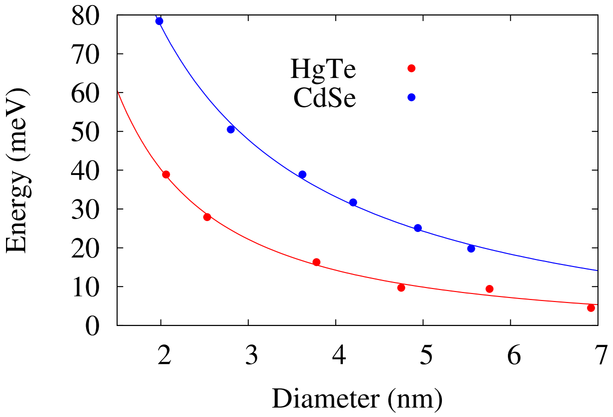

Figure 5.34: The difference in energy between the band-edge exciton and trion (-) peaks of HgTe (red) and CdSe (blue). This splitting in CdSe is almost double that of HgTe.

5.3.3 Conclusion

Our study shows an interesting transformation in electronic properties from HgTe bulk to HgTe NCs. In HgTe bulk the Γ_6 band, with a negative effective mass, is occupied and lay under the Γ_8 band. Nevertheless, in HgTe NCs, the HOMO state is shown to have Γ_8 character and the LUMO is primarily from Γ_6 band. The result on the optical gap of HgTe NCs is in good agreement with experiment, the DB splitting is calculated atomistically for the first time providing useful information for future studies. We also investigate the absorption spectra of HgTe NCs in comparison to CdSe NCs. The difference in energy between the exciton and negative trion peaks is calculated.

Summary and Outlook

In this thesis, the newly developed AEP method is presented. The use of AEPs allows us to bypass a self-consistent procedure and to address eigenstates around a certain region of the spectrum (e.g., around the band-gap). Therefore, AEP enables the study of the optical properties of many-atoms systems, where mainly the energy states around band-gap are involved. The NCs in all calculations are terminated by pseudo hydrogen atoms and relaxed artificially by the way they are generated. To improve the underestimated band-gap and effective masses that inherited from the LDA results, an empirical correction is applied to the non-local part of norm-conserving pseudopotential.

To obtain the FS and optical properties of NCs, the screened CI theory is used in combination with AEP methods. We focus on three materials: CdSe, InP, and HgTe for their wide applications and fabrications. The results on CdSe NCs show good agreement with experiments. The qualitative disagreement between AEP and EMA results on the FS of CdSe NCs suggests an improvement of EMA. The comparison of the WZ and ZB FS as a function of size and ellipticity show that the absorption of significantly oblate zinc-blende nanocrystals can be very similar to "spherical" wurtzite nanocrystals. On the other hand, if the nanocrystals have no ellipticity but different crystal structures, the fine structure differs significantly. Conversely, structures with high ellipticity, either oblate or prolate, with different crystal structures, show similar fine structures. The results on InP NCs show good agreement between AEP and SEPM. Both theories reproduce well the experimental measurements on the DB splitting and the optical gap of NCs. The results on HgTe NCs are in good comparison with measured optical gaps. The calculated DB splitting, size-dependent absorption spectra and the exciton-trion splitting can be useful for further studies on this promising material.

For the outlook, the study of the exciton lifetime still needs more development. From the SP results obtained by AEP method, the research on the biexciton and trion is totally possible and that will contribute more understanding about the optical properties of NCs.

Bibliography

[1] N. Accanto, F. Masia, I. Moreels, Z. Hens, W. Langbein, and P. Borri. Engineering the spin–flip limited exciton dephasing in colloidal CdSe/CdS quantum dots. *ACS nano*, 6(6):5227–5233, 2012.

[2] A. Al-Otaify, S. V. Kershaw, S. Gupta, A. L. Rogach, G. Allan, C. Delerue, and D. J. Binks. Multiple exciton generation and ultrafast exciton dynamics in HgTe colloidal quantum dots. *Physical Chemistry Chemical Physics*, 15(39):16864–16873, 2013.

[3] G. Allan and C. Delerue. Tight-binding calculations of the optical properties of HgTe nanocrystals. *Physical Review B*, 86(16):165437, 2012.

[4] W. Andreoni, A. Baldereschi, and R. Car. Effects of cation order on the energy bands of gaas-alas heterostructures. *Solid State Communications*, 27(9):821–824, 1978.

[5] J. Bao and M. G. Bawendi. A colloidal quantum dot spectrometer. *Nature*, 523(7558):67, 2015.

[6] D. Battaglia and X. Peng. Formation of high quality InP and InAs nanocrystals in a noncoordinating solvent. *Nano Letters*, 2(9):1027–1030, 2002.

[7] A. D. Becke. A new mixing of Hartree-Fock and local density-functional theories. *The Journal of chemical physics*, 98(2):1372–1377, 1993.

[8] G. Bester. Electronic excitations in nanostructures: an empirical pseudopotential based approach. *Journal of Physics: Condensed Matter*, 21(2):023202, 2009.

[9] G. Bester, S. Nair, and A. Zunger. Pseudopotential calculation of the excitonic fine structure of million-atom self-assembled InGaAs/GaAs quantum dots. *Phys. Rev. B*, 67:161306(R), 2003.

[10] L. Biadala, Y. Louyer, P. Tamarat, and B. Lounis. Direct observation of the two lowest exciton zero-phonon lines in single CdSe/ZnS nanocrystals. *Physical review letters*, 103(3):037404, 2009.

[11] L. Biadala, B. Siebers, Y. Beyazit, M. D. Tessier, D. Dupont, Z. Hens, D. R. Yakovlev, and M. Bayer. Band-edge exciton fine structure and recombination dynamics in InP/ZnS colloidal nanocrystals. *ACS nano*, 10(3):3356–3364, 2016.

[12] M. Born and J. R. Oppenheimer. On the quantum theory of molecules. *Annalen der Physik (in German)*, 389, 1927.

[13] K. Bourzac. Quantum dots go on display. *Nature News*, 493(7432):283, 2013.

[14] A. Brodu, M. V. Ballottin, J. Buhot, E. J. Van Harten, D. Dupont, A. La Porta, P. T. Prins, M. D. Tessier, M. A. Versteegh, V. Zwiller, et al. Exciton fine structure and lattice dynamics in InP/ZnSe core/shell quantum dots. *ACS photonics*, 5(8):3353–3362, 2018.

[15] X. Brokmann, L. Coolen, M. Dahan, and J. Hermier. Measurement of the radiative and nonradiative decay rates of single CdSe nanocrystals through a controlled modification of their spontaneous emission. *Physical Review Letters*, 93(10):107403, 2004.

[16] M. Bruchez, M. Moronne, P. Gin, S. Weiss, and A. P. Alivisatos. Semiconductor nanocrystals as fluorescent biological labels. *science*, 281(5385):2013–2016, 1998.

[17] D. Brust, M. L. Cohen, and J. Phillips. Reflectance and photoemission from si. *Physical Review Letters*, 9(9):389, 1962.

[18] D. Brust, J. Phillips, and F. Bassani. Critical points and ultraviolet reflectivity of semiconductors. *Physical Review Letters*, 9(3):94, 1962.

[19] M. Califano, A. Franceschetti, and A. Zunger. Temperature dependence of excitonic radiative decay in CdSe quantum dots: the role of surface hole traps. *Nano Letters*, 5(12):2360–2364, 2005.

[20] M. Califano, A. Franceschetti, and A. Zunger. Lifetime and polarization of the radiative decay of excitons, biexcitons, and trions in CdSe nanocrystal quantum dots. *Physical Review B*, 75(11):115401, 2007.

[21] J. R. Cárdenas and G. Bester. Atomic effective pseudopotentials for semiconductors. *Phys. Rev. B*, 86:115332, 2012.

[22] M. Cardona, R. Kremer, R. Lauck, G. Siegle, A. Muñoz, and A. Romero. Electronic, vibrational, and thermodynamic properties of metacinnabar β-HgS, HgSe, and HgTe. *Physical Review B*, 80(19):195204, 2009.

[23] E. Caruthers and P. Lin-Chung. Pseudopotential calculations for (gaas) 1-(alas) 1 and related monolayer heterostructures. *Physical Review B*, 17(6):2705, 1978.

[24] J. R. Chelikowsky and M. L. Cohen. Nonlocal pseudopotential calculations for the electronic structure of eleven diamond and zinc-blende semiconductors. *Physical Review B*, 14(2):556, 1976.

[25] J. Chen, J. Song, X. Sun, W. Deng, C. Jiang, W. Lei, J. Huang, and R. Liu. An oleic acid-capped cdse quantum-dot sensitized solar cell. *Applied physics letters*, 94(15):153115, 2009.

[26] M. L. Cohen. Density functional theory and pseudopotentials: A panacea for calculating properties of materials. *International journal of quantum chemistry*, 61(4):603–611, 1997.

[27] M. L. Cohen and T. Bergstresser. Band structures and pseudopotential form factors for fourteen semiconductors of the diamond and zinc-blende structures. *Physical Review*, 141(2):789, 1966.

[28] C. de Mello Donegá, M. Bode, and A. Meijerink. Size-and temperature-dependence of exciton lifetimes in CdSe quantum dots. *Physical Review B*, 74(8):085320, 2006.

[29] C. de Mello Donega and R. Koole. Size dependence of the spontaneous emission rate and absorption cross section of CdSe and cdte quantum dots. *The Journal of Physical Chemistry C*, 113(16):6511–6520, 2009.

[30] C. Delerue, G. Allan, and Y. Niquet. Collective excitations in charged nanocrystals and in close-packed arrays of charged nanocrystals. *Physical Review B*, 72(19):195316, 2005.

[31] D. Dexter. Theory of the optical properties of imperfections in nonmetals. In *Solid state physics*, volume 6, pages 353–411. Elsevier, 1958.

[32] J. G. Díaz and G. W. Bryant. Electronic and optical fine structure of GaAs nanocrystals: The role of d-orbitals in a tight-binding approach. *Phys. Rev. B*, 73(7):929, Feb. 2006.

[33] A. L. Efros and A. V. Rodina. Band-edge absorption and luminescence of nonspherical nanometer-size crystals. *Physical Review B*, 47(15):10005, 1993.

[34] A. L. Efros, M. Rosen, M. Kuno, M. Nirmal, D. J. Norris, and M. Bawendi. Band-edge exciton in quantum dots of semiconductors with a degenerate valence band: Dark and bright exciton states. *Phys. Rev. B*, 54:4843–4856, Aug 1996.

[35] E. Fermi. Eine statistische methode zur bestimmung einiger eigenschaften des atoms und ihre anwendung auf die theorie des periodischen systems der elemente. *Zeitschrift für Physik*, 48:73–79, 1928.

[36] A. Fleszar and W. Hanke. Electronic structure of ii b- vi semiconductors in the gw approximation. *Physical Review B*, 71(4):045207, 2005.

[37] V. Fock. Näherungsmethode zur lösung des quantenmechanischen mehrkörperproblems. *Zeitschrift für Physik*, 61(1-2):126–148, 1930.

[38] A. Franceschetti, H. Fu, L. W. Wang, and A. Zunger. Many-body pseudopotential theory of excitons in InP and CdSe quantum dots. *Phys. Rev. B*, 60:1819–1829, Jul 1999.

[39] A. Franceschetti, L. Wang, H. Fu, and A. Zunger. Short-range versus long-range electron-hole exchange interactions in semiconductor quantum dots. *Physical Review B*, 58(20):R13367, 1998.

[40] H. Fu and A. Zunger. Local-density-derived semiempirical nonlocal pseudopotentials for InP with applications to large quantum dots. *Physical Review B*, 55(3):1642, 1997.

[41] H. Fu and A. Zunger. Excitons in inp quantum dots. *Physical Review B*, 57(24):R15064, 1998.

[42] W. Gao, P. Fallahi, E. Togan, J. Miguel-Sánchez, and A. Imamoglu. Observation of entanglement between a quantum dot spin and a single photon. *Nature*, 491(7424):426, 2012.

[43] K.-U. Gawlik, L. Kipp, M. Skibowski, N. Orłowski, and R. Manzke. HgSe: metal or semiconductor? *Physical review letters*, 78(16):3165, 1997.

[44] F. M. Gomez-Campos and M. Califano. Hole surface trapping in CdSe nanocrystals: dynamics, rate fluctuations, and implications for blinking. *Nano letters*, 12(9):4508–4517, 2012.

[45] X. Gonze, B. Amadon, P.-M. Anglade, J.-M. Beuken, F. Bottin, P. Boulanger, F. Bruneval, D. Caliste, R. Caracas, M. Côté, et al. Abinit: First-principles approach to material and nanosystem properties. *Computer Physics Communications*, 180(12):2582–2615, 2009.

[46] X. Gonze, J.-M. Beuken, R. Caracas, F. Detraux, M. Fuchs, G.-M. Rignanese, L. Sindic, M. Verstraete, G. Zerah, F. Jollet, et al. First-principles computation of material properties: the abinit software project. *Computational Materials Science*, 25(3):478–492, 2002.

[47] N. Goubet, A. Jagtap, C. Livache, B. Martinez, H. Portalès, X. Z. Xu, R. P. Lobo, B. Dubertret, and E. Lhuillier. Terahertz HgTe nanocrystals: beyond confinement. *Journal of the American Chemical Society*, 140(15):5033–5036, 2018.

[48] J. Q. Grim, S. Christodoulou, F. Di Stasio, R. Krahne, R. Cingolani, L. Manna, and I. Moreels. Continuous-wave biexciton lasing at room temperature using solution-processed quantum wells. *Nature nanotechnology*, 9(11):891, 2014.

[49] H. Haken. Z. physik 146, 527 (1956). *Nuovo cim*, 10:1230, 1956.

[50] D. Hamann, M. Schlüter, and C. Chiang. Norm-conserving pseudopotentials. *Physical Review Letters*, 43(20):1494, 1979.

[51] P. Han and G. Bester. Fundamental difference between measured and calculated exciton-phonon coupling in nanostructures. *Physical Review B*, 99(10):100302, 2019.

[52] D. R. Hartree. The wave mechanics of an atom with a non-coulomb central field. part ii. some results and discussion. In *Mathematical Proceedings of the Cambridge Philosophical Society*, volume 24, pages 111–132. Cambridge University Press, 1928.

[53] P. Hohenberg and W. Kohn. Inhomogeneous electron gas. *Physical review*, 136(3B):B864, 1964.

[54] J. Hu, L.-s. Li, W. Yang, L. Manna, L.-w. Wang, and A. P. Alivisatos. Linearly polarized emission from colloidal semiconductor quantum rods. *Science*, 292(5524):2060–2063, 2001.

[55] N. Janβen, K. M. Whitaker, D. R. Gamelin, and R. Bratschitsch. Ultrafast spin dynamics in colloidal ZnO quantum dots. *Nano letters*, 8(7):1991–1994, 2008.

[56] J. Jasieniak, M. Califano, and S. E. Watkins. Size-dependent valence and conduction band-edge energies of semiconductor nanocrystals. *ACS nano*, 5(7):5888–5902, 2011.

[57] J. Jasieniak, L. Smith, J. Van Embden, P. Mulvaney, and M. Califano. Re-examination of the size-dependent absorption properties of CdSe quantum dots. *The Journal of Physical Chemistry C*, 113(45):19468–19474, 2009.

[58] A. Javier, D. Magana, T. Jennings, and G. F. Strouse. Nanosecond exciton recombination dynamics in colloidal CdSe quantum dots under ambient conditions. *Applied physics letters*, 83(7):1423–1425, 2003.

[59] S. O. Jeon and J. Y. Lee. Relationship between the particle size of quantum dots and bistability of the quantum dot embedded organic memory devices. *Journal of Industrial and Engineering Chemistry*, 17(1):105–108, 2011.

[60] E. Johnston-Halperin, D. Awschalom, S. Crooker, A. L. Efros, M. Rosen, X. Peng, and A. Alivisatos. Spin spectroscopy of dark excitons in CdSe quantum dots to 60 t. *Physical Review B*, 63(20):205309, 2001.

[61] A. Karpulevich, H. Bui, D. Antonov, P. Han, and G. Bester. Nonspherical atomic effective pseudopotentials for surface passivation. *Phys. Rev. B*, 94:205417, Nov 2016.

[62] S. Keuleyan, E. Lhuillier, and P. Guyot-Sionnest. Synthesis of colloidal HgTe quantum dots for narrow mid-ir emission and detection. *Journal of the American Chemical Society*, 133(41):16422–16424, 2011.

[63] S. E. Keuleyan, P. Guyot-Sionnest, C. Delerue, and G. Allan. Mercury telluride colloidal quantum dots: Electronic structure, size-dependent spectra, and photocurrent detection up to 12 μm. *ACS nano*, 8(8):8676–8682, 2014.

[64] D. L. Klein, R. Roth, A. K. Lim, A. P. Alivisatos, and P. L. McEuen. A single-electron transistor made from a cadmium selenide nanocrystal. *Nature*, 389(6652):699, 1997.

[65] W. Kohn and L. J. Sham. Self-consistent equations including exchange and correlation effects. *Physical review*, 140(4A):A1133, 1965.

[66] M. Korkusinski, O. Voznyy, and P. Hawrylak. Fine structure and size dependence of exciton and biexciton optical spectra in CdSe nanocrystals. *Physical Review B*, 82(24):245304, 2010.

[67] M. V. Kovalenko, E. Kaufmann, D. Pachinger, J. Roither, M. Huber, J. Stangl, G. Hesser, F. Schäffler, and W. Heiss. Colloidal HgTe nanocrystals with widely tunable narrow band gap energies: from telecommunications to molecular vibrations. *Journal of the American Chemical Society*, 128(11):3516–3517, 2006.

[68] O. Labeau, P. Tamarat, and B. Lounis. Temperature dependence of the luminescence lifetime of single CdSe/ZnS quantum dots. *Physical Review Letters*, 90(25):257404, 2003.

[69] K. Leung, S. Pokrant, and K. B. Whaley. Exciton fine structure in CdSe nanoclusters. *Physical Review B*, 57(19):12291, 1998.

[70] E. Lhuillier, S. Keuleyan, and P. Guyot-Sionnest. Optical properties of HgTe colloidal quantum dots. *Nanotechnology*, 23(17):175705, 2012.

[71] L. Li and P. Reiss. One-pot synthesis of highly luminescent InP/ZnS nanocrystals without precursor injection. *Journal of the American Chemical Society*, 130(35):11588–11589, 2008.

[72] C. Livache, B. Martinez, N. Goubet, C. Gréboval, J. Qu, A. Chu, S. Royer, S. Ithurria, M. G. Silly, B. Dubertret, et al. A colloidal quantum dot infrared photodetector and its use for intraband detection. *Nature communications*, 10(1):2125, 2019.

[73] M. Lorenzon, S. Christodoulou, G. Vaccaro, J. Pedrini, F. Meinardi, I. Moreels, and S. Brovelli. Reversed oxygen sensing using colloidal quantum wells towards highly emissive photoresponsive varnishes. *Nature communications*, 6:6434, 2015.

[74] O. Madelung. *Semiconductors: data handbook.* Springer Science & Business Media, 2012.

[75] R. M. Martin and R. M. Martin. *Electronic structure: basic theory and practical methods.* Cambridge university press, 2004.

[76] F. Masia, N. Accanto, W. Langbein, and P. Borri. Spin-flip limited exciton dephasing in CdSe/ZnS colloidal quantum dots. *Physical review letters*, 108(8):087401, 2012.

[77] G. Messin, J.-P. Hermier, E. Giacobino, P. Desbiolles, and M. Dahan. Bunching and antibunching in the fluorescence of semiconductor nanocrystals. *Optics Letters*, 26(23):1891–1893, 2001.

[78] O. Mićić, H. Cheong, H. Fu, A. Zunger, J. Sprague, A. Mascarenhas, and A. Nozik. Size-dependent spectroscopy of InP quantum dots. *The Journal of Physical Chemistry B*, 101(25):4904–4912, 1997.

[79] O. I. Micic, C. J. Curtis, K. M. Jones, J. R. Sprague, and A. J. Nozik. Synthesis and characterization of InP quantum dots. *The Journal of Physical Chemistry*, 98(19):4966–4969, 1994.

[80] O. I. Mićić, J. Sprague, Z. Lu, and A. J. Nozik. Highly efficient band-edge emission from InP quantum dots. *Applied Physics Letters*, 68(22):3150–3152, 1996.

[81] A. Mohan, M. Felici, P. Gallo, B. Dwir, A. Rudra, J. Faist, and E. Kapon. Polarization-entangled photons produced with high-symmetry site-controlled quantum dots. *Nature Photonics*, 4(5):302, 2010.

[82] I. Moreels, G. Raino, R. Gomes, Z. Hens, T. Stoferle, and R. F. Mahrt. Band-edge exciton fine structure of small, nearly spherical colloidal CdSe/ZnS quantum dots. *ACS nano*, 5(10):8033–8039, 2011.

[83] M. Müller, S. Bounouar, K. D. Jöns, M. Glässl, and P. Michler. On-demand generation of indistinguishable polarization-entangled photon pairs. *Nature Photonics*, 8(3):224, 2014.

[84] C. B. Murray, D. J. Norris, and M. G. Bawendi. Synthesis and characterization of nearly monodisperse CdE (E= sulfur, selenium, tellurium) semiconductor nanocrystallites. *Journal of the American Chemical Society*, 115(19):8706–8715, 1993.

[85] J. W. Nicklas and J. W. Wilkins. Accurate electronic properties for (Hg, Cd)Te systems using hybrid density functional theory. *Physical Review B*, 84(12):121308, 2011.

[86] M. Nirmal, D. J. Norris, M. Kuno, M. G. Bawendi, A. L. Efros, and M. Rosen. Observation of the" dark exciton" in CdSe quantum dots. *Physical Review Letters*, 75(20):3728, 1995.

[87] D. J. Norris, A. L. Efros, M. Rosen, and M. G. Bawendi. Size dependence of exciton fine structure in CdSe quantum dots. *Physical Review B*, 53(24):16347, 1996.

[88] N. Orlowski, J. Augustin, Z. Gołacki, C. Janowitz, and R. Manzke. Direct evidence for the inverted band structure of HgTe. *Physical Review B*, 61(8):R5058, 2000.

[89] W. J. Parak, T. Pellegrino, and C. Plank. Labelling of cells with quantum dots. *Nanotechnology*, 16(2):R9, 2005.

[90] D. R. Penn. Wave-number-dependent dielectric function of semiconductors. *Physical Review*, 128(5):2093, 1962.

[91] M. Penna, A. Marnetto, F. Bertazzi, E. Bellotti, and M. Goano. Empirical pseudopotential and full-brillouin-zone k· p electronic structure of CdTe, HgTe, and Hg1-xCdxTe. *Journal of electronic materials*, 38(8):1717–1725, 2009.

[92] J. P. Perdew and Y. Wang. Accurate and simple analytic representation of the electron-gas correlation energy. *Physical Review B*, 45(23):13244, 1992.

[93] J. P. Perdew and A. Zunger. Self-consistent equations including exchange and correlation effects phys. *Rev. B*, 23:5048–79, 1981.

[94] J. C. Phillips. Energy-band interpolation scheme based on a pseudopotential. *Physical Review*, 112(3):685, 1958.

[95] R. Resta. Thomas-fermi dielectric screening in semiconductors. *Phys. Rev. B*, 16:2717–2722, Sep 1977.

[96] V. Rinnerbauer, K. Hingerl, M. Kovalenko, and W. Heiss. Effect of quantum confinement on higher transitions in HgTe nanocrystals. *Applied physics letters*, 89(19):193114, 2006.

[97] G. Schlegel, J. Bohnenberger, I. Potapova, and A. Mews. Fluorescence decay time of single semiconductor nanocrystals. *Physical Review Letters*, 88(13):137401, 2002.

[98] P. C. Sercel and A. L. Efros. Band-Edge Exciton in CdSe and Other II–VI and III–V Compound Semiconductor Nanocrystals âĹŠRevisited. *Nano Letters*, 18(7):4061–4068, 07 2018.

[99] G. Shen, M. Chen, and P. Guyot-Sionnest. Synthesis of nonaggregating HgTe colloidal quantum dots and the emergence of air-stable n-doping. *The journal of physical chemistry letters*, 8(10):2224–2228, 2017.

[100] W.-S. Song, H.-S. Lee, J. C. Lee, D. S. Jang, Y. Choi, M. Choi, and H. Yang. Amine-derived synthetic approach to color-tunable InP/ZnS quantum dots with high fluorescent qualities. *Journal of nanoparticle research*, 15(6):1750, 2013.

[101] S. Steiger, M. Povolotskyi, H.-H. Park, T. Kubis, and G. Klimeck. NEMO5: A Parallel Multiscale Nanoelectronics Modeling Tool. *IEEE Transactions on Nanotechnology*, 10(6):1464–1474, Oct. 2011.

[102] Q. Sun, Y. A. Wang, L. S. Li, D. Wang, T. Zhu, J. Xu, C. Yang, and Y. Li. Bright, multicoloured light-emitting diodes based on quantum dots. *Nature photonics*, 1(12):717, 2007.

[103] A. Szabo and N. S. Ostlund. *Modern quantum chemistry: introduction to advanced electronic structure theory.* Courier Corporation, 2012.

[104] X. Tang, M. M. Ackerman, G. Shen, and P. Guyot-Sionnest. Towards infrared electronic eyes: flexible colloidal quantum dot photovoltaic detectors enhanced by resonant cavity. *Small*, 15(12):1804920, 2019.

[105] M. D. Tessier, D. Dupont, K. De Nolf, J. De Roo, and Z. Hens. Economic and size-tunable synthesis of InP/ZnE (e= s, se) colloidal quantum dots. *Chemistry of Materials*, 27(13):4893–4898, 2015.

[106] L. H. Thomas. The calculation of atomic fields. In *Mathematical Proceedings of the Cambridge Philosophical Society*, volume 23, pages 542–548. Cambridge University Press, 1927.

[107] N. Troullier and J. L. Martins. Efficient pseudopotentials for plane-wave calculations. *Physical review B*, 43(3):1993, 1991.

[108] A. Van Driel, G. Allan, C. Delerue, P. Lodahl, W. L. Vos, and D. Vanmaekelbergh. Frequency-dependent spontaneous emission rate from CdSe and cdte nanocrystals: Influence of dark states. *Physical Review Letters*, 95(23):236804, 2005.

[109] D. Vanderbilt. Soft self-consistent pseudopotentials in a generalized eigenvalue formalism. *Physical review B*, 41(11):7892, 1990.

[110] L.-W. Wang and A. Zunger. Local-density-derived semiempirical pseudopotentials. *Physical Review B*, 51(24):17398, 1995.

[111] L.-W. Wang and A. Zunger. High-energy excitonic transitions in CdSe quantum dots. *The Journal of Physical Chemistry B*, 102(34):6449–6454, 1998.

[112] U. Woggon, F. Gindele, O. Wind, and C. Klingshirn. Exchange interaction and phonon confinement in CdSe quantum dots. *Physical Review B*, 54(3):1506, 1996.

[113] P. Y. Yu and M. Cardona. *Fundamentals of semiconductors: physics and materials properties.* Springer, 4th edition, 2010.

[114] J. Zhang, Y. Tang, K. Lee, and M. Ouyang. Tailoring light–matter–spin interactions in colloidal hetero-nanostructures. *Nature*, 466(7302):91, 2010.

[115] Q. Zhao, P. A. Graf, W. B. Jones, A. Franceschetti, J. Li, L.-W. Wang, and K. Kim. Shape dependence of band-edge exciton fine structure in CdSe nanocrystals. *Nano letters*, 7(11):3274–3280, 2007.

[116] F. Zirkelbach, P.-Y. Prodhomme, P. Han, R. Cherian, and G. Bester. Large-scale atomic effective pseudopotential program including an efficient spin-orbit coupling treatment in real space. *Physical Review B*, 91(7):075119, 2015.

[117] A. Zunger. Electronic-structure theory of semiconductor quantum dots. *Mrs Bulletin*, 23(2):35–42, 1998.

Acknowledgements

First and foremost, I am heartily thankful to my supervisor, Prof. Dr Gabriel Bester, for giving me the opportunity to work in his group and to do research on a very interesting topic. He organizes the group meeting every week to discuss questions and problems arising from our research. I also want to thank him for being an amiable professor and always encourage me in my work.

I would like to thank my co-supervisor, Prof. Dr. Alf Mews, for encouraging and helpful advice.

I would like to thank all members of my group for many interesting discussions, as well as life enjoying during my PhD time. Especially, thanks to Anastasia Karpulevich, who always supports and gives me appropriate advice for any problem I have. Thanks to Jens and Walter for correcting the abstract of my thesis. Thanks to Marie for helping me with all administrative formalities form my first day in Germany.

I would like to thank all of my Vietnamese friends in Hamburg for being such a great company.

Finally, I am deeply thankful to my family for always standing by me wherever they are.

Declaration

I hereby confirm that I have taken the oath of the present dissertation and that I have not used anything besides the specified materials. The submitted written version corresponds to that on the electronic storage medium. I assure that this dissertation was not submitted in an earlier doctoral procedure.

Eidesstattliche Verischerung

Hiermit versichere ich an Eides statt, die vorliegende Dissertation selbst verfasst und keine anderen als die angegebenen Hilfsmittel benutzt zu haben. Die eingereichte schriftliche Fassung entspricht der auf dem elektronischen Speichermedium. Ich versichere, dass diese Dissertation nicht in einem früheren Promotionsverfahren eingereicht wurde.

Thi Hanh Bui	Date